國立臺灣大學電機資訊學院生醫電子與資訊學研究所

博士論文

Graduate Institute of Biomedical Electronics and Bioinformatics

College of Electrical Engineering and Computer Science

National Taiwan University

Doctoral Dissertation

靜息態功能性磁振造影之轉譯技術開發：

從影像品質檢驗到術前大腦功能定位

Translating Resting-state fMRI to Clinical Application: from Imaging Quality Assurance to Presurgical Brain Mapping

許艾伶

Ai-Ling Hsu

指導教授：陳志宏 博士、劉鶴齡 博士

Advisor: Jyh-Horng Chen, Ph.D., Ho-Ling Liu, Ph.D.

中華民國 107 年 8 月

August 2018

誌謝

"六年光陰似是轉眼逝，眼前艱辛苦樂唯自知，方憶師長昔叮囑，此番前去登高孤獨路。千里馬之美國行，離鄉背景獨一人，家親眷屬兩地遙，所遇所見難言盡，幸得親屬昌衛共支持、同儕鼓勵齊並進，方有今日之所成。前行之路遠又遙，欲謝之人數不盡，惟祈大家皆順遂、共享幸福與安康。"

這些日子以來，十分感謝台大電機系的陳志宏教授。在他富含創意的教導下，讓我從原本的小心翼翼轉化為大膽前行的個性。若無陳老師的信任與賞識，我很難有機會實地經歷教學、服務與研究的同時並進。在技術與思維訓練上，感激 MD Anderson Cancer Center 的劉鶴齡老師，從生理至技術專業知識、從口條練習到文章寫作，皆耐心引導我學習所需具備之細心求證精神。除了學術指導外，也在兩位指導老師身上學到了遇境的調伏能力與積極的處事態度，讓我有能力面對未來的挑戰。在此，學生對兩位指導老師至上最深的感恩與敬意。再來感謝伴我與助我成長的昌衛，是你在無數個分不清白天黑夜的日子中，共享我的苦與樂、幫我排憂解難、支持我前行。在美國一年的千里馬學習所遇之人事物，皆對我在獨立生活與研究上有相當顯著的影響力，感激 Dr. Hou 給我諸多的實務建議、Dr. Prabhu 讓我進入手術室的見習機會以及 Peter 幫助我釐清程式撰寫上的盲點。另外，還需要感謝曾在台大陳老師與陽明林慶波老師實驗室裡中，幾位在研究或生活上照料我的學長們：目前任職於台大電機所的謝昭賢博士、臺北市立萬芳醫院李家瑋博士、陽明大學腦科學研究中心周坤賢助理研究員、復旦大學腦類腦智能研究院羅畯義青年研究員、美商奇異公司林建源博士、謝孟錡博士、吳億澤博士。你們認真負責的研究精神與不屈不饒的做事態度，都是讓我積極向上動力。在此亦要感謝在服務學習與數個計畫截止日前一齊奮鬥的助理夥伴們，艾晶、郁文、婉婷、雅芝，正因為有與你們日以繼夜的共同努力，方能在最後一秒奮力一搏。在研究方法學的抽絲剝繭歷程中，謝謝台大與陽明實驗室同儕們，包含筠安、佩霖、偉倫醫師、柏暐、逸航、虹誼、柏翊、至新，沒有與你們的相互切磋與腦力激盪，我演述的能力亦無法精進。一個歷程的結束也是另一段生活的緣起，致謝的最後要留給最親愛的家人，謝謝你們的支持與鼓勵，即使我的成長如鴨子划水般緩慢前行，你們都不曾放棄我，帶著你們的祝福，我有信心繼續邁向人生下一個階段。

i

中文摘要

自 1995 年首度發現大腦網路的自發性同步現象以來，靜息態功能性磁振造影（Resting-state fMRI, rs-fMRI）技術日益受到神經科學以及臨床神經醫學研究的重視。因其非侵入性且無需外在刺激的實驗設計與簡單指令，該技術已被廣泛運用於兒童發育、老化歷程、神經退化以及精神疾病等群組研究。然而 rs-fMRI 技術並不僅侷限於群組研究，隨著轉譯醫學與個人化醫療技術的快速進展，rs-fMRI 亦逐步受到關注，現正興起一波以 fMRI 進行精準術前大腦功能定位之浪潮。然而，在真正實現以 rs-fMRI 進行個人化評估之前，仍需面對下列三項困境：（一）評估指標：該技術迄今尚未發展出有效的檢驗指標，難以評估其資料品質；（二）種子點選擇：就分析方法而言，經常使用的種子點相關性分析（seed-based correlation analysis）需要主觀設定一種子點，以分析大腦在休息狀態下的網路連結，並定位個人化之功能網路。 隨探究的大腦網路愈趨向高階特化功能（如語言網路），受試者間的功能網路位置變異就越大，造成種子點選定的困難性；（三）分析平台：儘管 rs-fMRI 技術已蔚為潮流，目前仍欠缺以臨床應用導向設計的分析平台。

本論文的主旨在針對 rs-fMRI 資料、種子分析技術做進一步的品質檢驗指標設計與方法改良，並建構以臨床醫事人員為導向之 fMRI 技術分析平台，期望提供簡易操作的使用者介面與可靠的技術以進行臨床相關研究與應用。本論文共具三項主要目標，分列如下：

(一) 本論文**第一目標**為發展一 rs-fMRI 影像品質指標(PICSO)，估測 rs-fMRI 資料中蘊含的神經生理訊息承載量。結果顯示功能性連結的強弱與 PICSO 指標呈現正相關，反之常用快篩型指標一時序信雜比(tSNR)一和大腦功能性連結之間並無明顯關聯。

(二) 準確設定種子點為定位高階功能網路之首要目標，然而實作上存在諸多困難。本論文將以語言功能為例，提出一新式自動化選擇法一結合靜息態區域同質性（regional homogeneity, RH）與統合分析技術（Meta-analysis, MA）一利用 RH+MA 方法導航種子點的設定，增進術前語言功能定位之精準度。

(三) 倘若病灶已影響腦血管的健康狀態，則直接影響以健康血管為前提假設的 fMRI 訊號。為評估腦血管對 fMRI 的影響程度，近期研究建議在以 fMRI 進行大腦功能區域定位時，同時比對反應腦血管健康狀態的順應力圖譜（CVR mapping），避免誤判大腦重要功能區的範圍。故本論文的**第三目標**為發展一平台，整併與模組化任務型 fMRI（task-fMRI）、rs-fMRI 與 CVR mapping，並將結果轉換至與臨床閱片系統與手術導航系統相容之 DICOM 格式，便於醫師進行完整的術前評估與術中導航之用。

本論文的研究目標為轉譯功能性磁振造影分析技術於臨床應用。於技術上，設計實用型的影像品質檢驗指標、發展設定種子點之導航方法；於臨床上，整合多項技術於單一平台，得同時提供影像分析介面、視覺化呈現與直接整併至手術導航系統。在未來發展中，本論文將引入深度學習演算法，自動化解構靜息態功能性網路。這些初步成果顯示功能性造影技術在臨床應用上具有高度潛力。總結而言，本論文在神經科學領域提供了功能性磁振造影的技術改進與整合，預期將能貢獻於國內的醫學工程產業、個人化醫療以及提昇臨床診斷之精確度。
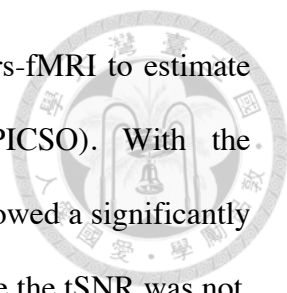
關鍵字：功能性磁振造影、靜息態功能性磁振造影、影像品質指標、術前大腦功能定位、大腦血管順應力圖譜、互動式分析平台、視覺化呈現

Abstract

Since its debut in 1995, the resting-state functional magnetic resonance imaging (rs-fMRI) has received sustained attention from fundamental and clinical neuroscience. Because of its non-invasive mapping of brain network integrity and high clinical feasibility without task engagements, this technique has proliferated amongst the fundamental investigations of development, geriatrics, and psychiatric and neurological disorders. Regarding its clinical practice in personalized medicine, presurgical functional mapping is of increasing importance in clinical management to aid the surgical planning to patients with neurosurgical intervention. Targeting on presurgical mapping, rs-fMRI is occasionally used in clinical practices. The rationale is that this technique still faces several methodological challenges: (1) a practical measure of rs-fMRI data quality to obtain reliable functional networks that has yet to be determined; (2) the inter-subject variability in functional localization and lesion-related functional reorganization makes the seed selection difficult for mapping functional networks on the basis of anatomical landmark alone, and thus affect its clinical use; (3) Despite its importance and usefulness, a specialized clinical software that integrates complementary fMRI techniques for presurgical fMRI workflow is still lacking.

Inherited from the rs-fMRI technique, this dissertation targets at three specific aims: (1) quality assurance from physiological contributions, (2) seed guidance for presurgical language mapping with seed-based rs-fMRI, and (3) technique integration in the specialized software for clinical practices. The ultimate goal of this PhD dissertation is to translate and integrate state-of-the-art fMRI techniques for presurgical mapping and clinical studies.

In specific aim 1, we proposed a quality-assurance index for rs-fMRI to estimate the physiological contributions in spontaneous oscillations (PICSO). With the calibration through the phantom data, we verified that the PICSO showed a significantly positive correlation with the strength of functional connectivity while the tSNR was not, providing a practical quality-assurance indicator for all existing rs-fMRI data sets.

In specific aim 2, we proposed a novel method to guide the seed selection for mapping the rs-fMRI language network by incorporating data-driven regional homogeneity and meta-analysis. The results demonstrated that localization performance on language network was significantly improved comparing to the seed selection based on MNI coordinate and was equivalent to the seed localization guided by task-fMRI activation. These results suggest that the proposed method may be an effective and beneficial approach for rs-fMRI mapping in the clinical practice, especially when patients have difficulties in compliances of task engagements.

In specific aim 3, we developed the Integrated fMRI for Clinical Research (IClinfMRI) software package to incorporate advanced fMRI methods of task-fMRI, rs-fMRI, and cerebrovascular reactivity (CVR) mapping. Incorporating CVR technique is to indicate the potential false-negative areas in fMRI results, and to implement data conversion modules for facilitating clinical fMRI researches with the applicability to pre-surgical planning in the treatment of intracranial lesions.

In summary, the dissertation was designed for translating fMRI techniques into clinical practice, initiating from the quality examination, seed guidance of rs-fMRI mapping, to platform development. Verifying the positive relation of the PICSO index with the strength of functional connectivity, proposing an effective approach for quality assurance of rs-fMRI mapping, and developing the IClinfMRI software in the clinical workflow. In the future direction, we will develop a purely data-driven approach

independent of the needs that enable the identification of functional network through the deep learning algorithm.
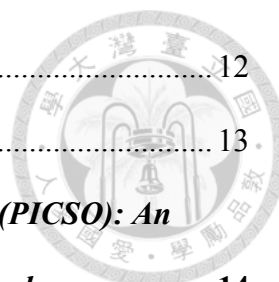
In conclusion, the proposed techniques and software in this thesis not only facilitate the application of fMRI techniques on daily clinical practices, but also improve the brain-mapping precision in personalized medicine.

Key words: Functional magnetic resonance imaging (fMRI), Resting-state fMRI, PICSO, Pre-surgical mapping, Preoperative mapping, Cerebrovascular reactivity, Interactive software, Visualization

Contents

List of Figures

List of Tables

Chapter 1

Introduction

1.1 Task-based functional Magnetic Resonance Imaging (fMRI) and its Role in Clinical Practices

1.1.1 Non-invasive Brain Mapping using Task-based fMRI

Human beings are able to sense the world through the intermittent neuronal firings in our central nervous system. Since renaissance, physician and philosophers have put great endeavor to unveil the mystery of our brain based on experiment-free speculations. The early evidence-based studies of understanding the brain function in cognitive processes measured the behavior changes from the brain-damage cases or population from invasive brain stimulations. Due to invasive nature of these measurements, scientists was inaccessible to investigate the function of human brain systematically. In early 1990's, the non-invasive imaging technique—functional magnetic resonance imaging (fMRI)—was firstly introduced (Kwong et al., 1992; Ogawa et al., 1990). Utilizing the blood oxygenation level dependent (BOLD) mechanism as a surrogate of neuronal activity, fMRI has become the dominate technique in the field of cognitive neuroscience (Bandettini, 2007) and clinical practice (Matthews et al., 2006) for its capability of whole brain functional mapping and accessibility of many medical centers.

1

Conventional task-evoked fMRI (task-fMRI) detects the BOLD signal changes in intermittent periods of a particular task from the baseline (resting) condition. Specifically, when a population of neurons is evoked by a task and has synchronized firing, the local cerebral blood circulation slowly supplies a huge amount of oxygenated hemoglobin from capillary vasodilation. Relying on the tight coupling of neuronal activity to regional increases in cerebral blood flow, this hemodynamic response is regarded as inevitable consequences of synaptic activity (Logothetis et al., 2001), resulting in an increased ratio of oxyhemoglobin to deoxyhemoglobin and an enhancement of a detectable magnetic homogeneity around the brain regions with neural activities. As a result, the local neural activity leads to a regional raise of the MRI signal intensity.

1.1.2 Advantages of Task-based fMRI Technique
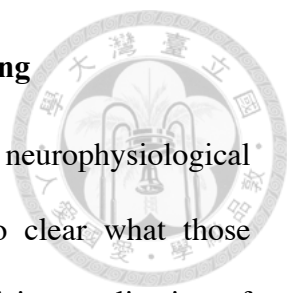
Given the neurophysiological foundation based on BOLD theorem, the task-fMRI technique has multiple advantages for scientific researches and clinical applications (Huettel et al., 2009): (1) fMRI is performed on the standard MRI scanners, radiation-free, and no needs for injecting exogenous contrast agents; instead, it measures the endogenous contrast agent—the BOLD signal—in the brain; (2) since the BOLD contrast is the hemodynamic consequence of neural activity, it provides high flexibility and repeatability to experiment design in term of task paradigm and longitudinal follow-up studies; (3) the feasibility of task-fMRI with a spatial resolution ranging from 2 to 4 millimeter can be overlaid on a brain anatomical image with resolution of 1 millimeter. To date, fMRI is the methodology providing the highest spatial resolution with whole brain coverage to disclose the hidden neural correlates of cognitive behaviors.

1.1.3 Task-based fMRI Applicability in Clinical Research

Although fMRI has not completely become a routine clinical tool, it has already impacted on clinical imaging research for the management of neurological diseases (Matthews and Hampshire, 2016; Matthews et al., 2006). Based on the BOLD mechanisms, fMRI provides a means to detect brain functional deficits with clinical relevance when performing task engagements. Thus, it has been used to explore functional characterization of neurological/psychiatric diseases for assessing neural correlates of clinical syndromes and predicting the long-term prognosis after treatments. For example, studies of prevalent psychiatric conditions—schizophrenia—illustrate the use of fMRI on developing imaging markers for classifying the type of psychiatric disorders (Barch et al., 2003; Macdonald et al., 2005).
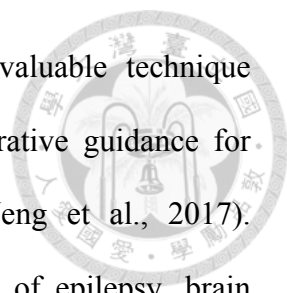
Schizophrenia involves a range of clinical features, such as the delusions, hallucinations, and disorganized thinking. Its functional deficit has been consistently found in different cognitive tasks and the most of these tasks, including executive functions, attention, and memory, involves in the fronto-temporal pathway (Barch et al., 2003; Becker et al., 2008; Minzenberg et al., 2009; Mwansisya et al., 2017). By identifying the specific imaging marker of functional abnormality in schizophrenia, fMRI response in prefrontal cortex has been demonstrated to differentiate the untreated patients with schizophrenia from other patients with non-schizophrenia psychosis (Macdonald et al., 2005) and depression (Barch et al., 2003). In addition to its potential for clinical managements, fMRI may have a broader range of applications in clinical neuroscience research to elucidate the neural mechanisms of functional recovery in psychiatric disorders (Rasetti et al., 2010; Scoriels et al., 2013) and stroke (Dong et al., 2007; Jaillard et al., 2005).

1.1.4 Clinical Practice of Task-based fMRI in Presurgical Mapping

At the current moment, it is clear that fMRI could demonstrate neurophysiological differences in case–control comparisons, but it is not always so clear what those differences add values to personalized medicine. One of the promising application of clinical fMRI is to aid neurosurgical planning in order to maximize the lesion resection while reducing the risk of postsurgical functional deficits. The benefits of a large resection must be weighed against the cost of resultant neurological deficits incurred in areas of eloquent cortex, particularly in motor/language areas. Despite the strong similarities among individual brains that enable group studies to be conducted, the specificity of individual subject for presurgical planning is neglected in group averages analysis. Compared to healthy normal, due to the grossly altered anatomy and brain plasticity, the degree of inter-subject variability is typically higher in patients, particularly in the higher-order cortical areas, such as language areas. Additionally, as each patient's brain anatomy is unique, and the substantial individual variability of language localization has been reported by stimulation mapping in a large cohort of 117 patients (Ojemann et al., 1989). Therefore, the presurgical functional localization is not generalizable, not reliably detected based on anatomic landmark alone, and must be evaluated individually (Bates et al., 2003; Silva et al., 2018).

To the high demands of individualized functional localization, the task-fMRI with high spatial resolutions has been served for clinical purpose on determining the dominant hemisphere, localizing brain functions, and predicting postsurgical outcomes (Benjamin et al., 2017) and have been shown to correlate with the clinical gold-standard of Wada testing (Janecek et al., 2013), intra-operative direct cortical stimulation (DCS) (Bizzi et al., 2008; Weng et al., 2017), and prediction of postsurgical outcomes
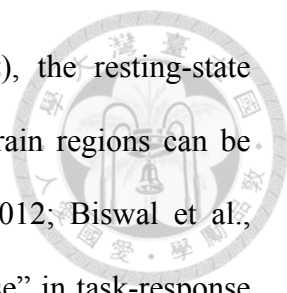
(Sabsevitz et al., 2003). These validations make task-fMRI a valuable technique applicable for preoperative counseling and planning and intraoperative guidance for lesion resection in the eloquent cortex (Bizzi et al., 2008; Weng et al., 2017). Additionally, it has been proven effective in guiding the surgery of epilepsy, brain tumor, and arteriovenous malformations (Bookheimer, 2007; Genetti et al., 2013; Pillai, 2010), and continues to dominate clinical practice (Matthews et al., 2006).

However, the challenge of applying task-fMRI to presurgical mapping is the patient compliance. The effectiveness of task-fMRI is highly dependent on patient performances in terms of effective participation, adequate cooperation, and task completion due to neurological deficits or altered behavior capabilities (Bookheimer, 2007; Pujol et al., 1998), which is often compromised at baseline prior to surgery and limits the interpretability of maps derived solely from these paradigms (Bookheimer, 2007). Furthermore, in some cases that patients might not be feasible to stay awake during the imaging procedure, often limiting the use of task-fMRI in population for whom conscious sedation is frequently necessary, such as pediatric or aged populations. Despite its utility, these challenges would restrict the task-fMRI on clinical applications to only a small percentage of total fMRI variance.

1.2 Resting-state fMRI and its Role in Clinical Practices

1.2.1 Spontaneous Synchronizations

As an adjunct to task-fMRI, Bharat Biswal and his colleagues found that human brain shows temporal synchronizations of spontaneous activities between regions while participants are at rest (not performing any task) over the duration of the scanning session (Biswal et al., 1995). By measuring the temporal synchronization of these

spontaneous low-frequency BOLD signal oscillations (< 0.1 Hz), the resting-state functional connectivity (rsFC) networks across spatially distinct brain regions can be extracted from resting-state fMRI (rs-fMRI) signal (Bandettini, 2012; Biswal et al., 1995). These rs-fMRI signals were viewed as the background "noise" in task-response studies due to its non-stimulus locked feature in an experimental paradigm. Even though scientists have yet fully understood its neurophysiological basis of rsFC, a growing body of neuroimaging evidence from rodents, monkeys to humans has informed the interpretation of resting-state fMRI (rs-fMRI) (Chen et al., 2017; Pan et al., 2011; Wilson et al., 2016; Wu et al., 2017). Rather than rsFC *per se*, cumulative studies indicate that global fluctuation of spontaneous BOLD oscillations is linked to broadband EEG activity (Wong et al., 2013), correlates with global fluctuation of cerebral blood flow (Zhao et al., 2017) and regional glucose metabolism (Tomasi et al., 2013). These all suggest that the spontaneous activity play a functional role for large-scale communication and synchronization in the brain.
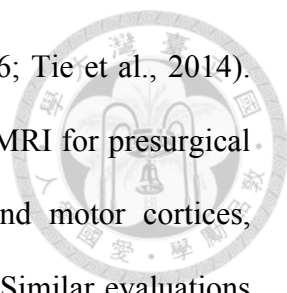
The rs-fMRI networks are often detected with use of seed-based correlation analysis (SCA) (Biswal et al., 1995; Shimony et al., 2009) or data-driven approaches such as independent component analysis (ICA) (Smith et al., 2009; Zhang et al., 2009). The SCA approach is straightforward to correlate the extracted reference time courses against every voxel in the brain, but it imposes prior knowledge to select the reference time courses by averaging over a seed. For extracting rsFC network, data-driven method is more popular to be adopted because it is free from *a priori* bias in seed selection. Although the ICA approach does not have the issues associated with seed placement, determining the proper number of components and selecting components of interest in this approach remain challenging (Branco et al., 2016).

1.2.2 Resting-state Functional Connectivity (rsFC) in Clinical Research

Rs-fMRI has rapidly growing applications in clinical fMRI research for both theoretical and practical reasons. Theoretically, the brain is organized and composed of functional networks, in which spatially distinct brain regions concomitantly share information with each other. A large body of literature indicates that brain organization derived from rsFC networks are altered in patients with psychiatric and neurological disorders (Lee et al., 2013; Matthews and Hampshire, 2016), showing an alternative connectivity perspective in understanding the relevance of brain disorder to large-scale network properties. Practically, by asking patients to lie quietly in the scanner for about 6 minutes, rs-fMRI paradigm does not require patients to perform cognitive tasks, making it with high feasibility in clinical routine. This circumvents the problem of interpreting activation differences that is regrading to task performance differences. Additionally, it can be performed when patients are during early sleep stages (Fukunaga et al., 2006; Heine et al., 2012) and light sedation (Greicius et al., 2008; Heine et al., 2012; Liang et al., 2015), expanding its applicability to patient populations for who are difficult to comply with the task paradigm. Another advantage of rs-fMRI is its ability to identify many functional networks in single acquisition, thus saving scan time if multiple networks are to be assessed.

1.2.3 Benefits of rsFC in Presurgical Mapping

Regarding its clinical practice in personalized medicine, presurgical functional mapping is of increasing importance in clinical management to aid the surgical planning to patients with neurosurgical intervention. Using either with seed-based (Zhang et al., 2009) or data driven analysis (Mitchell et al., 2013), rs-fMRI have shown its feasibility of identifying motor and language networks in patients with brain tumors (Branco et al.,

7
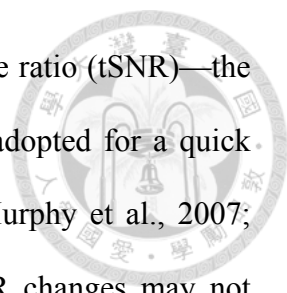
2016; Cochereau et al., 2016; Mitchell et al., 2013; Sair et al., 2016; Tie et al., 2014). Zhang and colleagues described the initial experiences in using rs-fMRI for presurgical planning in four patients with tumors infiltrating the sensory and motor cortices, comparing rs-fMRI with task-fMRI and DCS (Zhang et al., 2009). Similar evaluations were then conducted on 6 and 8 patients with lesions close to the motor cortex (Kokkonen et al., 2009; Liu et al., 2009). Mitchell et al., showed an average 80% sensitivity for sensorimotor identification, but moderated consistency (only less than 65%) for linguistic mapping as compared to DCS with a limit number of epileptic and tumor patients (Mitchell et al., 2013), resulted from high intra-subject variability. More recently, an encouraging study with a larger number of tumor and epilepsy patients showed moderate consistency of language network identification between task-fMRI and rs-fMRI (Branco et al., 2016). With the same approach, Sair et al. demonstrated that the reasons limiting their concordance were mainly high intra-subject variability. Together, evidence from these studies suggests the potential usefulness of rs-fMRI in presurgical planning.

1.3 Current Challenges of Clinical Practices using rs-fMRI Techniques

1.3.1 Quality Control of rs-fMRI

The task-fMRI techniques are to assess the signal increments over the baseline intensities, so the variations in the temporal dynamics are used as the quality assessments for task-fMRI (Krüger et al., 2001). However, the RS-fMRI is the baseline signal itself, which means that the quality assessment approach in task-fMRI no longer stands valid in rs-fMRI. However, with popularity of rs-fMRI in cognitive and clinical research and its potential for surgical planning, the necessity of rs-fMRI quality

assurance is increasing. Conventionally, the temporal signal-to-noise ratio (tSNR)—the ratio of the mean signal over its temporal standard deviation—is adopted for a quick quality examination (Bodurka et al., 2007; Krüger et al., 2001; Murphy et al., 2007; Triantafyllou et al., 2005). Yet previous study revealed that tSNR changes may not truthfully reflect connectivity alterations (Molloy et al., 2014). By definition, the tSNR emphasizes the baseline average of rs-fMRI time courses, whereas this baseline information does not contribute to rsFC. Instead, intrinsic rsFC is supposed to reflect the spontaneous synchronization of neuronal basis, thus the temporal fluctuations take the major contribution to rsFC outcomes. Despite importance of rs-fMRI in clinical applications, a practical measure to access data quality for existing rs-fMRI data sets is still warranted.

1.3.2 From Group Results towards Individualized Mapping

By using SCA approach, the inter-subject variability in functional localization and lesion-related functional reorganization makes the seed selection difficult for mapping functional networks on the basis of anatomical landmark alone, and thus affect its clinical use (Mueller et al., 2013; Rosazza et al., 2014; Sohn et al., 2015). The inter-subject variability has been further demonstrated to be heterogeneous distributed across brain networks in not only health subjects (Mueller et al., 2013) but also in patients (Mitchell et al., 2013). Furthermore, Sohn et al. showed that the standardized seeds across healthy subjects lead to inaccurate calculations of rsFC, and and Yan et al. demonstrated diverse rsFC results when placing distinct seed locations (Sohn et al., 2015; Yan et al., 2013). These studies commonly addressed the impact of seed selection on rsFC. In addition, Cochereau et al. recently indicated that the use of seed-based analysis achieved 80% accuracy in detecting individual language network (Cochereau et

9

al., 2016) when selecting seeds from intraoperatively stimulated positive sites. Even though their approach is not applicable for presurgical mapping, it demonstrated that seeding precisely would greatly improve the detection accuracy for individualized mapping of language network from rs-fMRI.
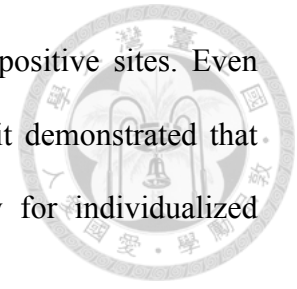
1.3.3 Presumption of fMRI Techniques: Neurovascular Coupling

Based on the BOLD principle, the fMRI's capability to reflect regional neural activity mainly relies on the intact coupling of cerebrovascular response following neural firings (Harrison et al., 2002; Roy and Sherrington, 1890). This presumption, termed as neurovascular coupling, refers to the complex neurophysiological mechanism that links transient neural activities to the local functional hyperemia subsequent to cognitive events, which is the key principle of *in vivo* neuroimaging techniques through BOLD hemodynamics (Devonshire et al., 2012; Harris et al., 2011; Huber et al., 2014; Mukamel et al., 2005).

However, in clinical cases, the abnormal cerebral vasculature or regional hemodynamic disruption caused by intracranial pathology can impair the cerebrovascular reactivity (CVR) and violate the presumption of neurovascular coupling. The altered neurovascular coupling had been observed on abnormal physiological states such as cerebrovascular diseases, brain tumors and neurodegenerative diseases (Iadecola, 2004; Mikulis, 2013; Ulmer et al., 2003), thereby contributing to false negative findings in fMRI (lack of BOLD signal despite neural activity). For the use of fMRI mapping as tool of surgical planning, these false negatives in fMRI mapping may potentially lead to an undesirable resection of eloquent cortex (Pak et al., 2017; Pillai and Mikulis, 2015; Ulmer et al., 2003). Without further confirmation by intraoperative direct cortical

10

stimulation, the fMRI false negatives could result in permanent postoperative neurological deficits.

To evaluate the risk of lesion-induced neurovascular uncoupling (NVU), mapping CVR by dynamic BOLD imaging during a vasodilatation challenge would be a useful technique for assisting the interpretation of clinical fMRI (Pak et al., 2017; Pillai and Mikulis, 2015). CVR mapping has been used to identify the impaired neurovascular coupling in brain-tumor patients with task-fMRI (Hou et al., 2006; Zacà et al., 2014), and, most recently, in those with rs-fMRI (on motor network rsFC) (Agarwal et al., 2016). Practically, CVR experiments can be conducted using ordinary fMRI acquisition methods during a breath-holding (BH) task (Kastrup et al., 2001; Liu et al., 2002). Despite its importance in clinical applications, CVR mapping has yet reached the status of an established clinical diagnostic procedure because data analysis for CVR mapping requires modifications to the existing fMRI software, which is a time-consuming and arduous procedure without expert's assistance.

1.4 Specific Aims

This dissertation raises three specific aims targeting at the above-mentioned fMRI challenges in clinical research correspondingly: (1) addressing a new quality assurance method for rs-fMRI (Hsu et al., 2016), (2) launching a semi-auto seed guidance approach for individualized mapping of language network by rs-fMRI (Hsu et al., 2018), and (3) integrating multiple fMRI techniques in one specialized software for clinical practices ().

Because three projects were included in this dissertation, I divided it into background knowledge in chapter 1, elaborated three project-oriented sections from

11

chapter 2 to chapter 4, and discussed further considerations of addressed approaches in chapter 5.

1.4.1 Quality Assurance for rs-fMRI

Recently, data quality in rs-fMRI has received substantial attention because multiple MRI centers often adopt diverse ways of rs-fMRI protocols. In principle, tSNR could be used as a quick measure of rs-fMRI data quality, but it does not guarantee reliable rsFC outcomes. Therefore, we proposed a quality-assurance index for rs-fMRI to estimate the physiological contributions in spontaneous oscillations (PICSO). With the calibration through the phantom data, we verified that the PICSO showed a significantly positive correlation with FC while the tSNR was not, providing a practical quality-assurance indicator for all existing rs-fMRI data sets.

1.4.2 Individualized Functional Mapping

Targeting on presurgical mapping, rs-fMRI has shown its potential to localize intrinsic functional networks for the patients who cannot comply with task demands. One of the common approaches of network detection is the seed-correlation analysis that imposes the prior knowledge of seed selection. However, high inter-subject variability in language localization and lesion-related functional reorganization make the seed selection difficult for mapping brain networks on the basis of anatomical landmark alone, and thus limit its clinical use. Here we proposed a novel method to guide the seed selection for mapping the language network by incorporating data-driven regional homogeneity and meta-analysis in rs-fMRI. The results demonstrated that localization performance on language network was significantly improved comparing to the seed selection based on MNI coordinate and was equivalent to the seed localization guided by task-fMRI activation. These results suggest that the proposed method may be

12

an effective and beneficial approach for rs-fMRI mapping in the clinical practice, especially when patients have difficulties in compliances of task engagements.
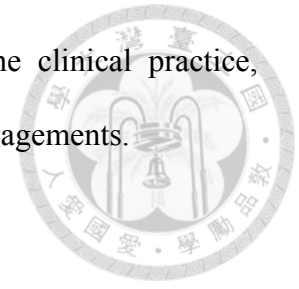
1.4.3 Toolbox Development for Clinical Routine

Task-fMRI, rs-fMRI and CVR mapping have been applied to clinical management of neurological diseases, exemplified by pre-surgical functional mapping. Although the analyses for different fMRI modalities are theoretically feasible with existing research software, a specialized clinical software that can integrate the three complementary fMRI techniques and export the mapping results in DICOM format for PACS and surgical navigation system remains unavailable for clinical practices. Thus, we developed the Integrated fMRI for Clinical Research (IClinfMRI) software package by incorporating advanced fMRI methods with streamlined processing and shortened the processing time to facilitate clinical fMRI researches with the applicability to pre-surgical planning in the treatment of intracranial lesions. With results illustrated in two clinical patients, we verified that IClinfMRI was validated against a well-established software package—AFNI.

Chapter 2

Physiological Contribution in Spontaneous Oscillations (PICSO): An Approximate Quality-Assurance Index for Resting-State fMRI Signals

2.1 Introduction

The brain at rest is composed of multiple functional networks that have been extensively explored using connectivity approaches. Resting-state functional connectivity (rsFC) measures the synchronization of low-frequency blood-oxygen-level dependent (BOLD) oscillations (Biswal et al., 1995), which are presumed to be the surrogate of spontaneous neuronal cross-talks (Leopold et al., 2003; Logothetis, 2007; Logothetis et al., 2001). Although scientists do not fully understand the intrinsic essence of resting-state fMRI (rs-fMRI) signals, numerous studies have demonstrated that rsFC can be altered by several neurological, psychiatric, and neurodegenerative diseases (e.g., Alzheimer's disease, Parkinson's disease, depression, dementia, and schizophrenia) and can be dynamic among physiological conditions (e.g., anesthesia or sleep) (Boveroux et al., 2010; Horovitz et al., 2009; Zhang and Raichle, 2010). A current trend in the proliferation of rs-fMRI investigations is to perform data mining from multi-center data

14
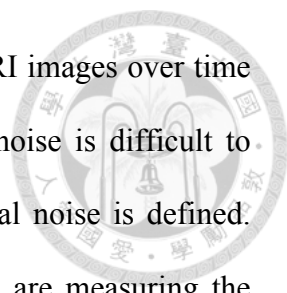
sets for large samples (e.g., The Alzheimer's Disease Neuroimaging Initiative, 1000 Functional Connectomes Project, and Human Connectome Project) (Smith et al., 2013). However, because of the various types of data acquisition and experimental conditions, a promising quality-evaluation strategy is warranted for producing reliable rsFC outcomes.

Currently, a common measure of rs-fMRI data quality is the temporal signal-to-noise ratio (tSNR), which is the ratio of the mean signal over its temporal standard deviation (SD) (Bodurka et al., 2007; Krüger et al., 2001; Murphy et al., 2007; Triantafyllou et al., 2005). Triantafyllou et al. tested the dependence of the tSNR on scanning parameters, such as magnetic field strength, flip angle (FA), image resolution, and echo time (TE) (Triantafyllou et al., 2005), and suggested the optimal conditions for enhancing the tSNR (Triantafyllou et al., 2006). Although the tSNR provides an initial indication of rs-fMRI data quality, tSNR changes are not directly reflected in rsFC alterations (Molloy et al., 2014; Triantafyllou et al., 2005; 2006). In other words, a high tSNR does not guarantee reliable connectivity strength (CS). An extreme example of this is that the fMRI data from the phantom possess a high tSNR, but these data do not result in long-distance connectivity. This is because, by definition, the tSNR emphasizes the baseline average of rs-fMRI time courses. However, this baseline information does not contribute to rsFC; instead, the temporal fluctuations take the major contribution to rsFC outcomes. More specifically, the temporal fluctuations in rs-fMRI signals can be regarded as a combination of spontaneous neural activities, non-neuronal fluctuations (i.e., respiration and cardiac pulsation), and thermal noise from scanner electronics. Conceptually, rsFC results from the synchronization of spontaneous neural activities, whereas non-neuronal fluctuations and thermal noise are irrelevant to neuronal synchronization but are inevitably involved in rs-fMRI signals. Therefore, the

15

physiological contributions in spontaneous oscillations, once quantified, should be a meaningful candidate for measuring the sensitivity of functional connectivity.
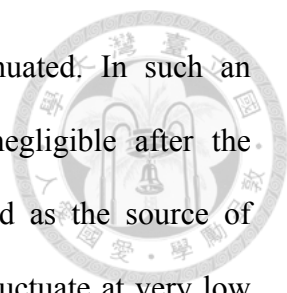
However, quantifying the physiological contributions in spontaneous activities is not a trivial task. Apart from hardware imperfections (Weisskoff, 1996), the physiological contributions in rs-fMRI signals were first addressed by the Krüger physiological noise model (Krüger et al., 2001; Triantafyllou et al., 2005). This model assumes that the noise variance in the imaging voxels is composed of thermal noise, non-neuronal fluctuations, and spontaneous fluctuations of a potentially neuronal origin. Therefore, if the thermal noise could be estimated according to rs-fMRI signals, then the physiological contributions over thermal noise could be defined as a quality measure for rs-fMRI. This concept has previously been addressed, demonstrating the dependence of physiological contributions on the acquisition parameters. Triantafyllou et al. investigated the improvement of physiological contributions at a high field strength, large FA, and low spatial resolution (Triantafyllou et al., 2005). Bodurka et al. suggested the optimal fMRI voxel size when the thermal noise matches the physiological fluctuations (Bodurka et al., 2007). Additionally, Gonzalez-Castillo presented that the physiological contributions were more sensitive to the FA than the tSNR was (Gonzalez-Castillo et al., 2011). Although these studies have emphasized the importance of physiological contributions for fMRI signals, their quantification strategies are time-consuming and unrealistic for application to existing rs-fMRI data sets and clinical routines.

Conceptually, a practical measure for quantifying physiological contributions should be voxel-wise, free from region of interest (ROI) selection, and without changing parameters in imaging acquisition. In Krüger's model, the total fluctuation

16

level is directly measured according to the SD of reconstructed fMRI images over time (Krüger et al., 2001); however, consensus on estimating thermal noise is difficult to achieve because this metric depends on how and where the thermal noise is defined. Two methods that are generally used for estimating thermal noise are measuring the spatial noise from a noise-only region or measuring the temporal noise without radio-frequency (RF) excitation. The first approach is more widely used than the second, but its applicability to rs-fMRI data is limited for three reasons: (a) manual selection of the noise region outside of the image object is required for calculating the background noise level; (b) regardless of imaging artifacts, hundreds of pixels are required in order to obtain a reasonable estimate of background noise because the precision of the noise estimation is proportional to the square root of the number of pixels in the ROI; (c) the suitability of manual ROI selection is questionable in parallel imaging because each channel contributes differently across the entire field of view. Compared with the first approach, the second approach without RF excitation is a more straightforward estimation method for assessing pure thermal noise over time. However, it requires hardware, pulse sequence editing, longer acquisition time, and a special reconstruction algorithm (Kellman and McVeigh, 2005; Triantafyllou et al., 2011). Although the second approach is robust and precise, it is still generally unfeasible as a practical estimation surrogate for existing rs-fMRI data sets.

To address these concerns, we propose a new voxel-wise method for estimating the PhysIological Contributions in Spontaneous Oscillations (PICSO) of the acquired rs-fMRI data sets. With this method, the thermal noise over time of the rs-fMRI signals is estimated in approximation by subtracting the imaging signals between each pair of adjacent time points; this is an extended version of the difference method (Kellman and McVeigh, 2005; Reeder et al., 2005). This subtractive strategy enables high-frequency

signals to be emphasized and low-frequency signals to be attenuated. In such an estimation, the physiological contributions are assumed to be negligible after the voxel-wise subtraction, and the resultant residues can be regarded as the source of thermal noise because the spontaneous rs-fMRI signals generally fluctuate at very low frequencies (<0.1 Hz), close to a time-invariant characteristic for every pair of adjacent time points. To validate the applicability of the proposed method in thermal noise estimation, we first verified that fMRI signals acquired from the phantom possessed a zero PICSO value after we performed the calibration procedure. Subsequently, we observed a positive relationship between the CS and PICSO at various image resolutions because the image resolution has been reported as the major factor affecting the CS (Molloy et al., 2014; Triantafyllou et al., 2005; 2006). Moreover, we conducted various degrees of spatial smoothing on the rs-fMRI data to confirm that the alteration in the CS can be directly reflected by the PICSO. This new approach produces several advantages for quantifying the physiological contributions in fMRI signals such as the applicability to parallel MRI (Reeder et al., 2005) and to all rs-fMRI data sets for quality assurance.

2.2 Material and Method

2.2.1 Theory

All rs-fMRI signals can be regarded as a superposition of the intrinsic baseline signal and signal fluctuations. The quality of rs-fMRI data is typically measured using the tSNR, which is defined as the ratio of the baseline average $(\bar{s})$ to its SD over time (σ):

$$tSNR = \frac{\bar{s}}{\sigma} \tag{1}$$
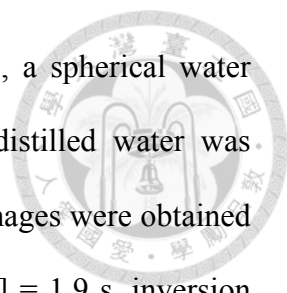
Assuming that the rs-fMRI signals are free from non-neuronal fluctuations (i.e., respiration and cardiac pulsation), the signal variance can be separated into thermal noise and the desired physiological fluctuations of neural origin (Bianciardi et al., 2009; Birn et al., 2008; Chang et al., 2009a; Glover et al., 2000). According to Krüger's model, the total signal fluctuations in the fMRI signal (σ) are the square-law sum of the Gaussian thermal noise (σ_0) and physiological fluctuations (σ_p), expressed in equation form as $\sigma = \sqrt{\sigma_0^2 + \sigma_p^2}$ (Krüger et al., 2001), where σ_0 is independent of the fMRI signal intensity and σ_p is scaled relative to the image intensity. Estimating the variance of both total fluctuation level and thermal noise facilitates calculating the ratio of physiological fluctuations to thermal noise, which is determined using Eq. (2):

$$\frac{\sigma_p}{\sigma_0} = \sqrt{\left(\frac{\sigma}{\sigma_0}\right)^2 - 1} \tag{2}$$

where the $\frac{\sigma_p}{\sigma_0}$ ratio represents the fMRI PICSO and can be regarded as the sensitivity surrogate in the rs-fMRI signals. Additionally, for any non-ideal circumstance that causes the ratio of total fluctuation level over thermal noise to be less than unity, the PICSO value would be set to zero.

2.2.2 Image Acquisition

A total of 12 right-handed healthy volunteers (age: 26.4 ± 2.1 y, females/males: 6/6) were enrolled in this study. All participants declared that they fully understood the experimental procedure and provided written informed consent. The entire procedure was approved by the Institutional Review Board of National Yang-Ming University. Data were acquired using a Siemens 3T Trio system with a 12-channel head coil. To

19

verify the accuracy of the thermal noise estimation in the PICSO, a spherical water phantom consisting of 1.25 g of $NiSO_4 \cdot 6H_2O$ per 1000 g of distilled water was scanned using identical imaging protocols. T_1-weighted structural images were obtained using the MP-RAGE sequence (TE = 2.27 ms, repetition time [TR] = 1.9 s, inversion time [TI] = 900 ms, FA = 9°, 176 slices with $1 \times 1 \times 1$ mm^3 voxels without an interslice gap). Given the fact that the weightings of thermal noise deviate with voxel sizes (Molloy et al., 2014), we acquired the rs-fMRI signals at various image resolutions as the dominant factor to manipulate the PICSO values for each single subject. Thereafter, the single-shot gradient-echo echo planar imaging (GE-EPI) sequence was adopted to acquire rs-fMRI data at four voxel sizes ($1.3 \times 1.3 \times 2$, $2 \times 2 \times 2$, $3 \times 3 \times 3$, and $5 \times 5 \times 5$ mm^3) by using the parameters shown in **Table 2-1**. Each session contained 150 time points and three dummy scans with a total acquisition time of 7 min 38 s. The scanning order of the four EPI sessions was counterbalanced in a Latin-square manner to reduce the systematic bias resulting from the scanning order of the EPI sessions. Because of the limited brain coverage for sessions at the highest spatial resolution ($1.3 \times 1.3 \times 2$ and $2 \times 2 \times 2$ mm^3), we assigned a slice orientation along the anterior and posterior commissure lines with the midline of the slab reaching the bottom edge of the corpus callosum to cover the thalamus (THAL) and posterior cingulate cortex (PCC). For the other sessions, we maintained the same slice orientation and ensured the coverage of the entire brain. The participants' heads were immobilized using cushions to minimize motion during image acquisition. During the rs-fMRI sessions, the participants were instructed to open their eyes, relax, and not think of anything specific. To minimize the contributions of non-neuronal sources embedded in the rs-fMRI signals, simultaneous cardiac and respiratory recordings were acquired using a built-in pulse oximeter and pneumatic belt, respectively (sampling rate = 50 Hz). A B_0 field map was acquired

using a dual-echo gradient echo sequence (TE_1 = 10 ms, TE_2 = 12.46 ms, TR = 600 ms, FA = 70°, 33 slices with $1.5 \times 1.5 \times 4$ mm^3 voxels) to correct image distortions caused by the inhomogeneity of B_0. The total acquisition time was 38 min 38 s.
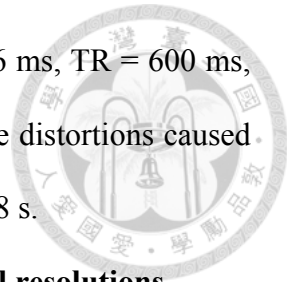
Table 2-1 Acquisition parameters for the EPI with four spatial resolutions

Acquired Voxel Size (mm^3)	FOV (mm)	Matrix Size
$1.3 \times 1.3 \times 2.0$	162×162	$128 \times 128 \times 27$
$2.0 \times 2.0 \times 2.0$	256×256	$128 \times 128 \times 27$
$3.0 \times 3.0 \times 3.0$	192×192	$64 \times 64 \times 35$
$5.0 \times 5.0 \times 5.0$	320×320	$64 \times 64 \times 24$

TR = 3000 ms, TE = 35 ms, flip angle = 87°,

Partial Fourier = 6/8, bandwidth = 1260 Hz/px, Echo spacing = 0.86 ms.

2.2.3 fMRI Processing

All scanning images were preprocessed using AFNI (Cox, 1996) and FSL (Jenkinson et al., 2012). During preprocessing, spatial smoothing is a crucial factor that affects the tSNR (Triantafyllou et al., 2006) and CS (Wu et al., 2011); thus, to prevent the additional smoothing induced by spatial normalization, all functional images were analyzed in the native space, including both preprocessing and the seed-correlation analysis, and finally transformed into the MNI space for group analysis. ***Figure 2-1*** demonstrates the workflow of phantom–human preprocessing. The phantom data set first underwent standard preprocessing (***Figure 2-1***) including motion correction, field map correction, and despiking. Subsequently, different detrending orders were performed to verify the signal drift induced by system instability.

21
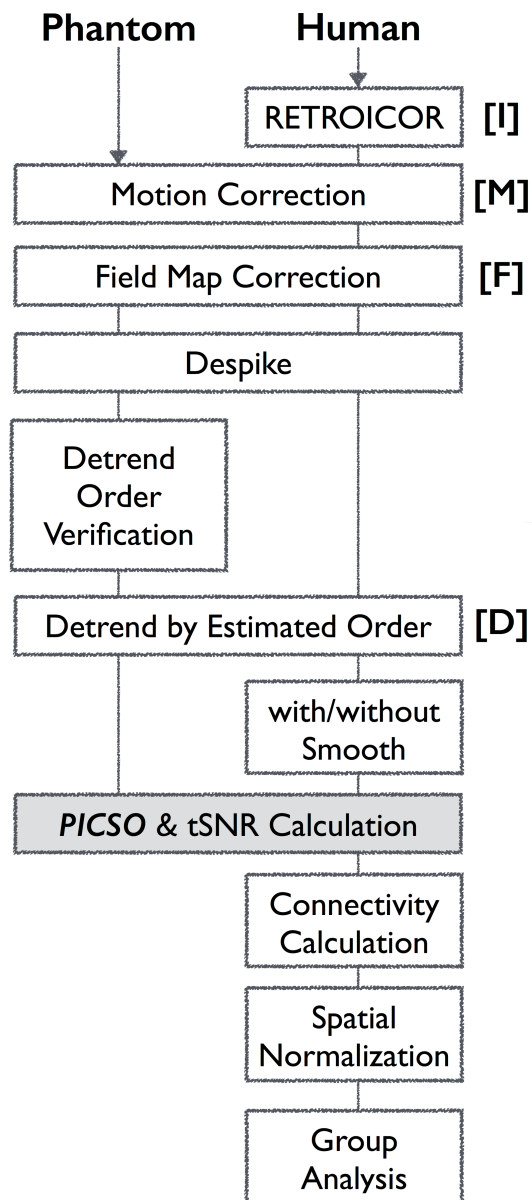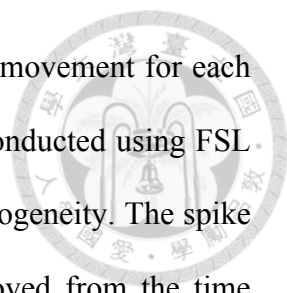
Figure 2-1 Flowchart of the rs-fMRI preprocessing procedure and PICSO estimation approach

The detrending order was then determined when the thermal noise was equal to the total fluctuation level because the phantom possessed the stationary baseline signal and lacked physiological fluctuations. For the human data, the effects of cyclic cardiac pulsation and respiration were first removed using RETROICOR with second-order Fourier series expansion (3dretroicor in AFNI) (Glover et al., 2000). Motion correction

was then performed using FSL (mcflirt) to minimize possible head movement for each rs-fMRI time series. Retrospective field-map correction was then conducted using FSL (fugue) to eliminate the image distortions caused by the field inhomogeneity. The spike (3dDespike in AFNI) and estimated polynomial trends were removed from the time series. Moreover, because head motion at both the individual and group levels can contribute to spurious correlations (Power et al., 2012; 2015), we examined the motion by using mean framewise displacement (FD) for the entire rs-fMRI data set. All rs-fMRI data fulfilled the motion criteria (i.e., mean FD < 0.3 mm). To further examine the effects of head motion on the PICSO, we performed a correlation analysis between the PICSO and mean FD for comparison.

2.2.4 Estimating the Thermal Noise and PICSO

After the preprocessing, for a given voxel, the tSNR was determined using Eq. (1) according to the ratio of the mean signal intensity $\bar{s}$ to the SD σ of a series of 150 functional images. Because the rs-fMRI signals were modeled as the sum of true BOLD intensity and the superimposed temporal noise, which following a Gaussian distribution (Wink and Roerdink, 2006), the slow fluctuations in rs-fMRI in adjacent acquisitions were assumed to be canceled out by subtraction, resulting in Gaussian-noise residue. Therefore, the voxel-wise thermal noise σ_0 was determined by calculating the SD of a series of subtractive images between adjacent scans and divided by $\sqrt{2}$ because the SD of the subtracted Gaussian noise is theoretically increased by $\sqrt{2}$ (Reeder et al., 2005). After the maps of thermal noise σ_0 and total noise σ were calculated, the PICSO map was determined as the ratio of the variance of the total fluctuation level to the thermal noise, as shown in Eq. (2). Subsequently, the tSNR and PICSO values were averaged within the predefined ROIs for a given data set at various spatial resolutions. For the

23
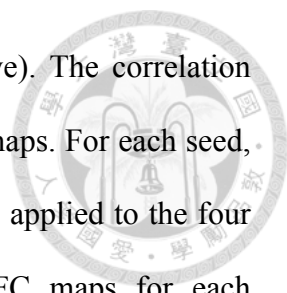
phantom results, we expected the thermal noise to be identical to the total fluctuation level, and the PICSO index to be zero.
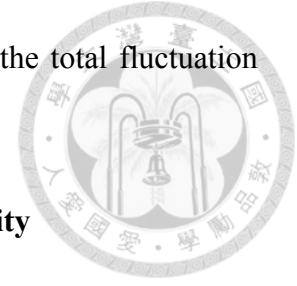
2.2.5 Seed-Based Correlation Analysis for Functional Connectivity

We conducted a seed-based correlation analysis by using the THAL to represent the subcortical structures and the PCC to signify the cortex representative. According to the data sets of four resolutions, the seed regions were identified in the native space through the following three steps: (1) The seed points of the left THAL and PCC were first defined using the MNI coordinates (-7, -16, 6) and (2, -51, 27), respectively (Greicius et al., 2003; Guldenmund et al., 2013). (2) These seed points were inversely transformed from the MNI space back to the reference data set ($3 \times 3 \times 3$ mm^3) in the native space, and the native seed regions were then prescribed a sphere with a 5-mm radius on the reference data set. (3) The native seed regions of the other resolutions (i.e., $1.3 \times 1.3 \times 2$, $2 \times 2 \times 2$, and $5 \times 5 \times 5$ mm^3) were transformed from the native seed region on the reference data set to match the image resolutions by using FSL (flirt). Following these steps ensured that the native seed regions were identical among the various imaging sessions to prevent the bias of seed size and the resulting CS.
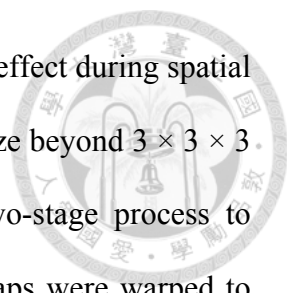
Prior to FC calculation, we conducted nuisance regression by using the following 10 covariables: six affine motion parameters, two temporal variations of the respiration volume and heart rate (Chang et al., 2009a), and the mean time series of white matter (WM) and cerebrospinal fluid (CSF). The WM and CSF masks were generated from the segmented T_1 anatomical image by using FSL fast with a threshold 50% probability, and transformed to match the image resolutions. Subsequently, the FC maps were obtained through a seed-regression analysis in the native space by extracting the average residual time series from the resolution-matched seed regions and using it as the

24

regressor against every voxel in the brain by AFNI (3dDeconvolve). The correlation maps from the regression model were then converted to Fisher's z maps. For each seed, the same procedures for seed prescription and seed correlation were applied to the four image resolutions and four smoothing levels, resulting in 16 FC maps for each participant. Setting the smoothing levels lower than the acquired image resolution did not affect the data sets; therefore, we report only 10 FC maps corresponding to the effective changes in spatial resolution. For the group analysis, the resulting z maps were normalized to the MNI space for a one-sample t test (3dttest++); the significance level was set to FDR-corrected p < 0.01 (3dFDR) with an explicit common mask among the participants. The normalization process is detailed in the following subsection.

2.2.6 Normalization after Functional Connectivity

To avoid imposing extra smoothing effects on PICSO estimations, we only applied spatial normalization for visualizing group-level index maps. The first volume of the functional data sets in the four acquired voxel sizes was used as the reference scan to estimate the transformation matrix. Spatial normalization was applied to transform the FC maps in the native space to the MNI space by using the predefined transformation matrix. The predefined transformation matrix that was used to transform the FC maps from the native space to the MNI space was produced using a two-stage (the reference scan with $3 \times 3 \times 3$ mm^3 spatial resolution) or three-stage process (the scans with other spatial resolutions). For the reference data set with an acquired voxel size of $3 \times 3 \times 3$ mm^3, the reference scan was aligned with the T_1 image (boundary-based registration). This aligned image was then nonlinearly warped to the MNI space by using the warping matrix, which was determined by warping the native T1 image to the MNI T1 image (fnirt). Next, the transformation matrices from the previous two stages were combined

25
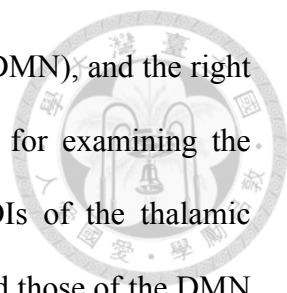
into a two-stage reference scan matrix to minimize the interpolation effect during spatial normalization. The other functional scans with the acquired voxel size beyond $3 \times 3 \times 3$ mm^3 were registered to the reference scan (flirt) prior to the two-stage process to produce a three-stage transformation matrix. Finally, all the FC maps were warped to the MNI space with a spatial resolution of $2 \times 2 \times 2$ mm^3 by using the two- or three-stage transformation matrices.

2.2.7 Resolution and Spatial Smoothing

To investigate whether the CS alterations could be directly reflected by the quality measurements (tSNR and PICSO), we manipulated multiple noise levels by processing the data sets with various degrees of smoothness. The smoothness of each preprocessed fMRI data set was controlled by applying a smoothing kernel until the predefined uniform full-width-at-half-maximum (FWHM) (measured in millimeters) was reached, matching the spatial resolutions of the acquired images (i.e., $2 \times 2 \times 2$, $3 \times 3 \times 3$, and $5 \times 5 \times 5$ mm^3). Notably, the FWHM is the inverse of the shortest distance that discriminates two points, and is determined according to the acquired voxel size and applied smoothing level. We did not apply the conventional smoothing method with a fixed Gaussian kernel because of the uncontrolled FWHMs; instead, we expanded the point spread function to specific levels to compensate for the intrinsic point spread functions of image acquisition, which might have differed among the participants.

2.2.8 ROI Analysis

To investigate whether the effect of the spatial resolution on the CS was consistent with that on both quality measurements (tSNR, and PICSO), Pearson's correlation analysis was conducted among the CS, tSNR, and PICSO in both the cortical and subcortical areas. The left THAL (L THAL) and PCC were chosen for studying the

26
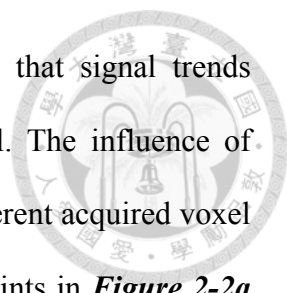
local rsFC within the thalamic network and default mode network (DMN), and the right THAL and medial prefrontal cortex (MPFC) were set as proxies for examining the strength of distant rsFC within these networks. The selected ROIs of the thalamic network were obtained from the MNI template embedded in FSL and those of the DMN were obtained from a previous study (Smith et al., 2009). All ROIs defined in the MNI space were warped to the native space corresponding to each acquired voxel size through inverse spatial normalization. The ROI analysis was performed to quantify the mean PICSO index, tSNR values, and CS in the native space. In addition, at the same FWHM, repeated-measures analysis of variance (ANOVA) was employed to compare the averaged PICSO values among the data sets in various voxel sizes, and Pearson's correlation analysis was used to examine the relationship between the quality measurements (tSNR and PICSO) and CS. Additionally, to further examine whether RETROICOR and imaging resolution affected the noise estimation, the average of both σ_0 and σ within the predefined ROIs was examined using two-way repeated-measures ANOVA (a 2×4 design, Factor 1: with and without applying RETROICOR, Factor 2: the four acquired imaging resolutions).

2.3 Result

2.3.1 PICSO Calibration and Estimation

Phantom data were used in the first step of calibration; ***Figure 2-2a*** depicts the total fluctuation level as a function of thermal noise under different voxel sizes of acquisition ($1.3 \times 1.3 \times 2$, $2 \times 2 \times 2$, $3 \times 3 \times 3$, and $5 \times 5 \times 5$ mm^3) and various detrending orders in preprocessing. The total fluctuation level decreased as the detrending order was set from linear, quadratic to cubic polynomial, whereas the

27

thermal noise was free from the effect of detrending, indicating that signal trends contributed dominantly to the estimation of total fluctuation level. The influence of detrending on the fMRI time series is shown in **Figure 2-2b** for different acquired voxel sizes. With the detrending order as cubic polynomial, the scatter points in **Figure 2-2a** are located on the identity line (PICSO = 0) among different acquired resolutions, verifying the reliability of thermal noise estimation on the basis of the subtracting procedure (Dietrich et al., 2007; Reeder et al., 2005; Triantafyllou et al., 2011).

Using the human data set as the second step of calibration, we attempted to validate that σ is sensitive to physiological noise, but σ_0 is not. We conducted a repeated-measure two-way ANOVA to test the RETROICOR effect on both thermal noise and total fluctuation level within the predefined seed-side ROI. For the L THAL, the σ estimation of data processed with RETROICOR differed significantly from that processed without RETROICOR ($F(1, 10) = 30.12$, $p < 0.05$), whereas the RETROICOR process did not significantly affect the estimation of σ_0 ($F(1, 10) = 0.87$, $p = 0.37$). In the PCC, the σ estimation of data processed with RETROICOR differed significantly from that processed without RETROICOR ($F(1, 10) = 32.34$, $p < 0.05$), whereas the data processed with RETROICOR did not significantly affect the estimation of σ_0 ($F(1, 10) = 0.02$, $p = 0.88$). For testing this concept throughout the brain, we adopted the same test for multiple ROIs in the MNI template embedded in FSL (Harvard–Oxford Subcortical Structural Atlas). Because of the limited spatial coverage of the acquired images, the ROIs could be used for testing only the bilateral cerebral cortex, THAL, caudate, putamen, and pallidum. The results are included in this manuscript as supplementary information (**Table 2-2**). The observations indicated that the σ_0 estimation is appropriate for estimating the noise, which is irrelevant to

physiology. Considering the influence of head motion on the PICSO estimation, we performed a correlation analysis to test the association between the PICSO values in the predefined ROIs and mean FD. No significant correlations were detected between the mean FD and PICSO for any ROIs, including the bilateral THAL, PCC, and MPFC ($p > 0.35$).
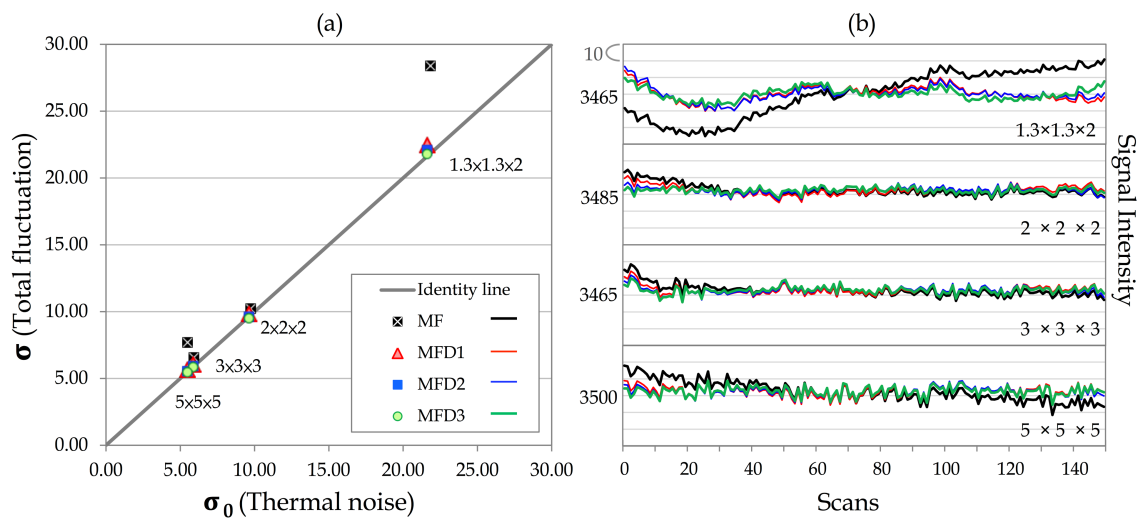
Figure 2-2 PICSO calibration using phantom data

(a) Total fluctuation level and the estimated thermal noise depend on the acquired spatial resolution and the preprocessing steps. The solid line represents the identity line (i.e., PICSO = 0). The solid black rectangle represents the results processed by motion correction (M) and field-map correction (F). Results with different levels of detrending (D) orders are denoted as D1, D2, and D3. The thermal noise and total fluctuation level showed identical changes when the detrending order was set as a cubic polynomial. (b) Corresponding time series without detrending and with different detrending orders among the four acquired voxel sizes. Time series processed without detrending and processed with the first, second, and third detrending orders are represented by the black, red, blue, and green lines, respectively. The numbers that appear on the left side of the time series represent the average signal intensity. Each line space indicates an intensity increment of 10.

Figure 2-3 shows the PICSO map from a single subject as a function of the acquired voxel sizes ($1.3 \times 1.3 \times 2$, $2 \times 2 \times 2$, $3 \times 3 \times 3$, and $5 \times 5 \times 5$ mm^3, without smoothing). The PICSO value increased with the acquired voxel size and presented the spatial specificity. The PICSO value in the neocortex was higher than that in the subcortical region. For all cortical regions, the PICSO value in the posterior brain was higher than that in the anterior brain, suggesting relatively high physiological contributions in the posterior brain.

Table 2-2 The RETROICOR effect on both σ_0 and σ within ten ROIs

	σ_0		σ			σ_0		σ	
ROI	F	p	F	p	ROI	F	p	F	p
L Cerebral Cortex	0.15	0.71	15.72	0.00*	R Cerebral Cortex	0.01	0.94	10.34	0.01*
L Thalamus	0.85	0.38	30.26	0.00*	R Thalamus	0.19	0.67	20.51	0.00*
L Caudate	1.21	0.30	9.38	0.01*	R Caudate	1.68	0.22	17.01	0.00*
L Putamen	0.21	0.65	14.36	0.00*	R Putamen	0.00	0.99	11.59	0.01*
L Pallidum	1.63	0.23	20.33	0.00*	R Pallidum	1.51	0.25	21.43	0.00*

A p-value of less than 0.05 was considered statistically significant and was designated with one (*) asterisk.

Grey color indicates no significant noise differences in repeated-measure two-way ANOVA tests.

2.3.2 PICSO Modulated by the Acquired Voxel Size

The diagonal pictures of the upper panels in *Figure 2-4* and *Figure 2-5* depict the FC as a function of the acquired voxel sizes in the thalamic network and DMN, respectively. In both networks, the mean CS increased monotonically with the voxel size ($p < 0.05$). As the voxel size increased, the mean CS ($\pm$SD) in the L THAL increased from 0.06 ($\pm$0.03) to 0.16 ($\pm$0.09), 0.28($\pm$0.10), and 0.40 ($\pm$0.09), and the corresponding PICSO increased from 0.00 ($\pm$0.00) to 0.21 ($\pm$0.14), 0.41 ($\pm$0.21), and

0.79 (±0.24). In the PCC, as the voxel size increased, the mean CS increased from 0.09 (±0.01) to 0.19 (±0.01), 0.27 (±0.02), and 0.32 (±0.03), and the corresponding PICSO increased from 0.22 (±011) to 0.49 (±0.15), 0.70 (±0.20), and 0.95 (±0.22).
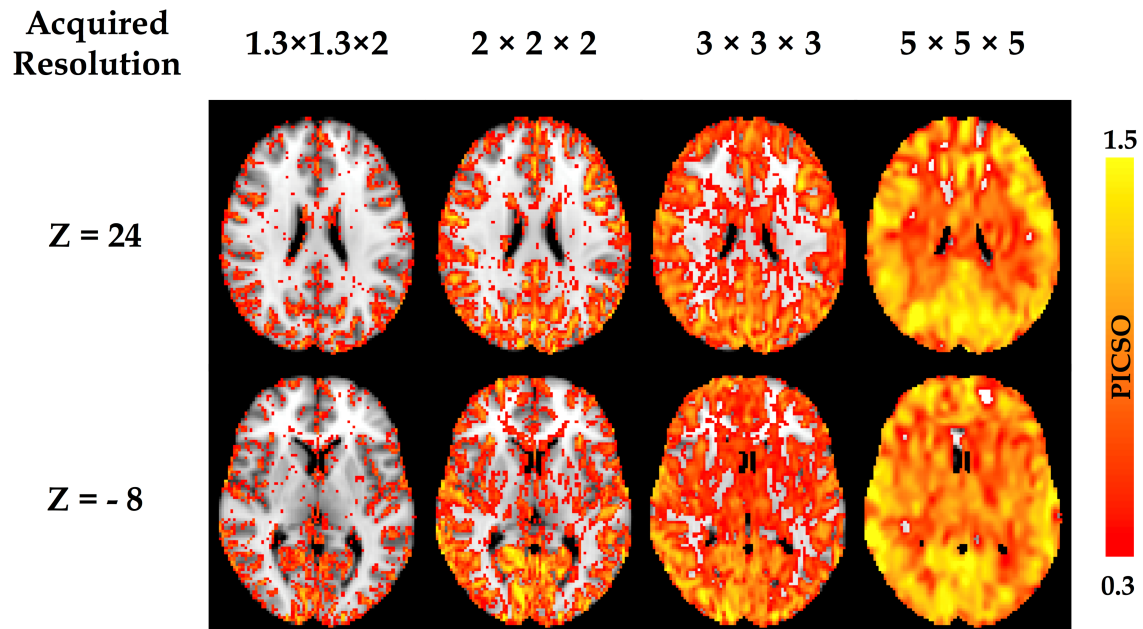
Figure 2-3 Voxel-wise PICSO map from a single subject

The PICSO value increases as a function of the acquired voxel sizes ($1.3 \times 1.3 \times 2$, $2 \times 2 \times 2$, $3 \times 3 \times 3$, and $5 \times 5 \times 5$ mm^3, without smoothing). Additionally, the PICSO value also possesses spatial specificity; the PICSO value of the posterior brain is generally larger than that of the anterior brain.

2.3.3 PICSO Modulated by the Smoothness

The off-diagonal pictures in the upper panels of *Figure 2-4* and *Figure 2-5* show the smoothing effects of the FC maps on the acquired voxel sizes in the thalamic network and DMN, respectively. For any fixed voxel size in acquisition, spatial smoothing substantially enhanced the CS and spatial extent within the network. However, when the FWHM was controlled after smoothing, the impact of the acquired voxel size on the CS was more substantial than the impact of smoothing. For example,

the CS of the data acquired at $2 \times 2 \times 2$ mm3 was significantly stronger than that of the data acquired at $1.3 \times 1.3 \times 2$ mm3 and smoothed to the uniform FWHM of $2 \times 2 \times 2$ mm3 (FDR-corrected $p < 0.01$). The lower panels of **Figure 2-4** and **Figure 2-5** show the relationships between the PICSO values and the fixed FWHMs after smoothing; the bars represent the multiple voxel sizes in acquisition.
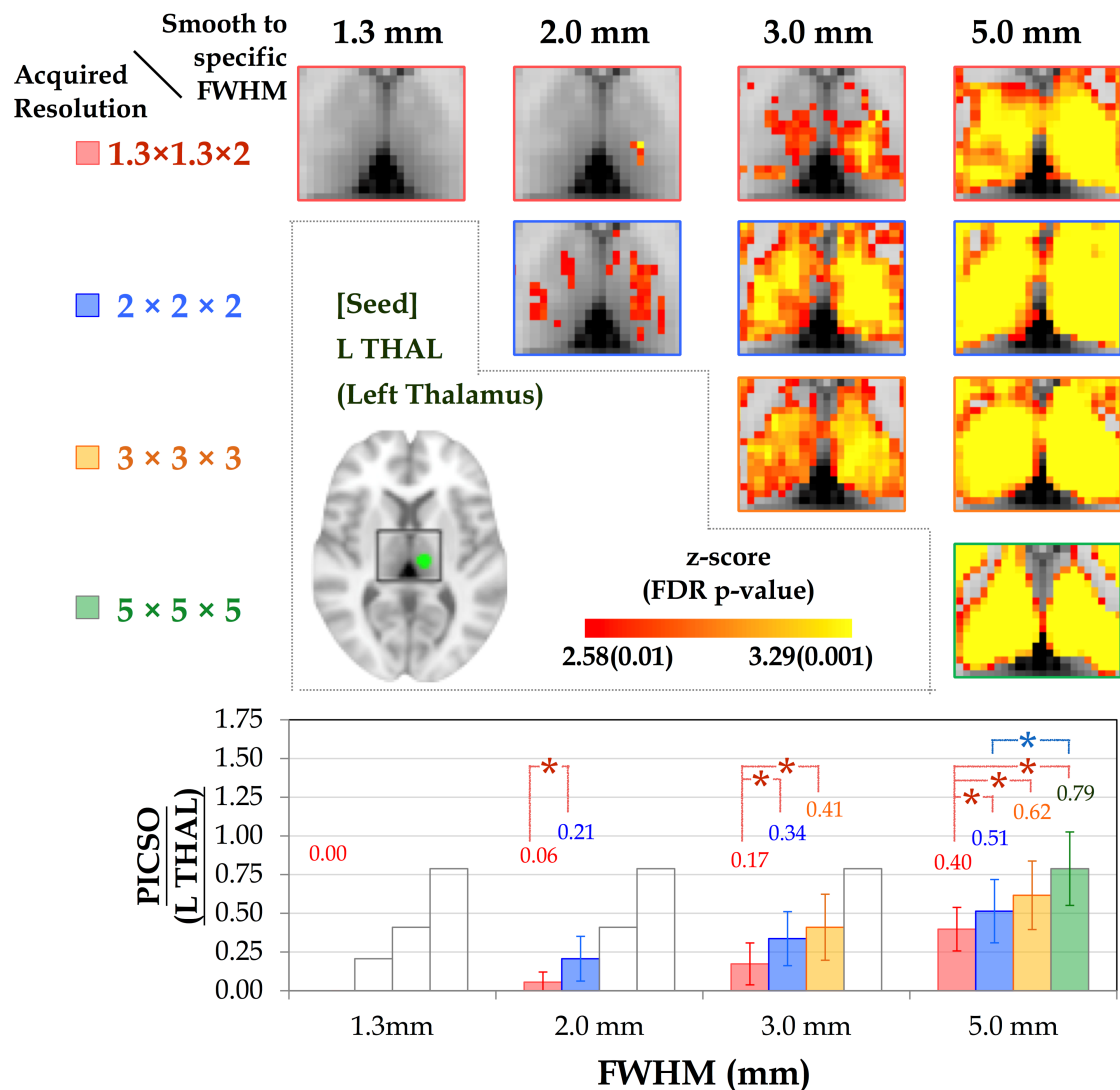
Figure 2-4 Group-level thalamic connectivity as a function of spatial resolution
(Upper) The thalamic connectivity varies with smoothness (FWHMs = 1.3, 2, 3, and 5 mm) under the four acquired voxel sizes. Although the spatial extent of FC is preserved among the various voxel sizes, the CS increases with the smoothness. (Lower) Bar chart illustrating the corresponding PICSO value for each smoothness level of the acquired

voxel sizes. Both the red and blue lines indicate significant differences in the paired comparisons (LSD-corrected p < 0.01).
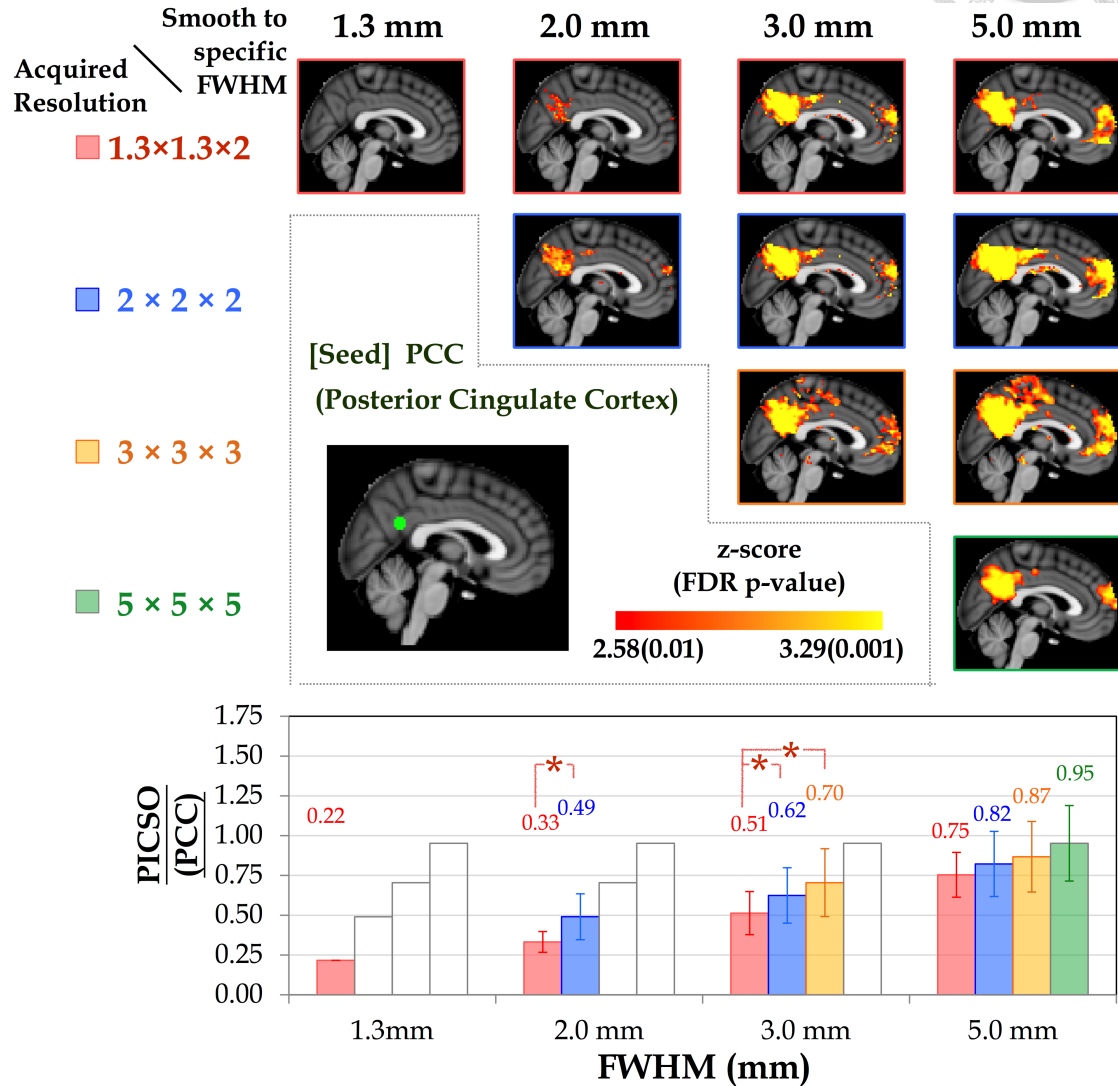
Figure 2-5 Group-level DMN connectivity as a function of spatial resolution
(Upper) DMN connectivity varies with smoothness (FWHMs = 1.3, 2, 3, and 5 mm) under the four acquired voxel sizes. (Lower) Bar chart illustrating the corresponding PICSO values for each smoothness level of the acquired voxel sizes. Both the red and blue lines indicate significant differences in the paired comparisons (LSD-corrected p < 0.01).

33

For example, for the final FWHM of 3 mm in the lower panel of *Figure 2-4*, the data with acquired voxel sizes of $2 \times 2 \times 2$ and $3 \times 3 \times 3$ mm3 had higher PICSO values than those with an acquired voxel size of $1.3 \times 1.3 \times 2$ mm did, and no significant difference in the PICSO values was observed between the data with acquired voxel sizes of $2 \times 2 \times 2$ and $3 \times 3 \times 3$ mm.

2.3.4 Relationship between the PICSO and CS

To verify the efficacy of using the PICSO or tSNR as quality measures for rs-fMRI, we conducted a correlation analysis to quantify the association between the CS and the two quality measurements after we controlled the smoothness. According to the data of three voxel sizes ($1.3 \times 1.3 \times 2$, $2 \times 2 \times 2$, and $3 \times 3 \times 3$ mm^3, which are conventionally adopted in human studies, all of which were smoothed to a fixed FWHM of 3 mm), *Figure 2-6* shows the relationship between the CS and both quality measurements (PICSO and tSNR) within the predefined seed ROIs. Each point in *Figure 2-6* indicates an individual subject, and the trend lines denote the coupling between the quality measurements and the CS among the three data sets. The PICSO and CS demonstrated a large significantly positive correlation within the L THAL ($r = 0.82$, $p < 0.05$) and a medium significantly positive correlation with the PCC ($r = 0.33$, $p < 0.05$). However, the tSNR, which is commonly adopted to test fMRI quality, showed a nonsignificant correlation with the CS. These phenomena indicated the high sensitivity of the PICSO index to the FC in the rs-fMRI signals.
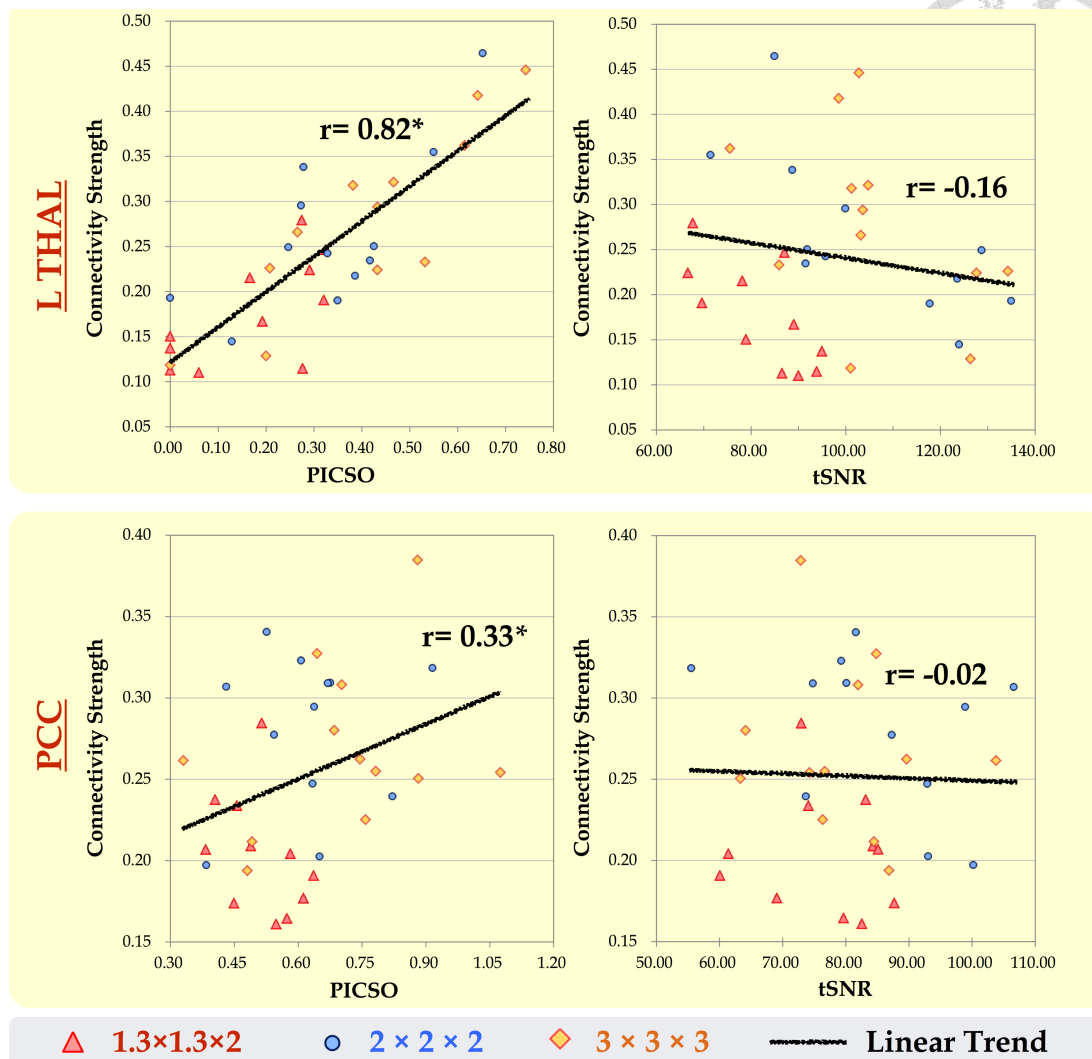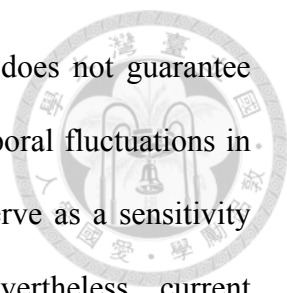
Figure 2-6 Relationship between both quality measurements (PICSO and tSNR) and the CS in the rs-fMRI data sets within the L THAL and PCC
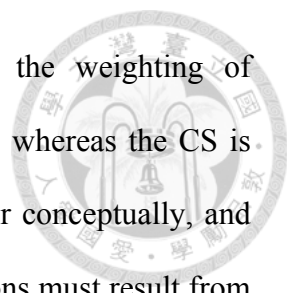
At a fixed FWHM of 3 mm, each point in the scatter plot indicates an individual subject, and the linear trend line denotes the coupling among the three data sets of the acquired voxel sizes of $1.3 \times 1.3 \times 2$, $2 \times 2 \times 2$, and $3 \times 3 \times 3$ mm^3. Only the trend lines between the PICSO and CS correlate significantly within the L THAL (r = 0.82) and PCC (r = 0.33).

2.4 Discussion

Recently, data quality in rs-fMRI has received substantial attention because different imaging centers often adopt different rs-fMRI protocols. In principle, tSNR
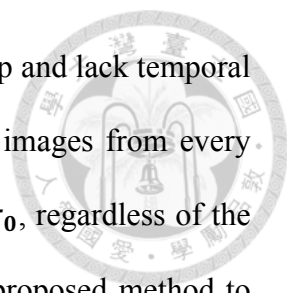
could be used as a quick measure of rs-fMRI data quality, but it does not guarantee reliable rsFC outcomes. Previous studies have emphasized the temporal fluctuations in fMRI signals and the potential of physiological contributions to serve as a sensitivity indicator of rs-fMRI quality (Triantafyllou et al., 2005). Nevertheless, current quality-evaluation strategies that involve manual ROI selection for determining physiological contributions are time-consuming and unrealistic when processing rs-fMRI data sets derived from a large sample (Molloy et al., 2014; Triantafyllou et al., 2005; 2006). Because of practical concerns, we first proposed a novel approach for estimating the physiological contributions in rs-fMRI signals under the assumption that the ultra-slow trends and low-frequency neuronal fluctuations can be minimized using temporal subtraction. We titled this estimation index as the PICSO for rs-fMRI, similar to the notion of the contrast-to-noise ratio in the stimuli-evoked fMRI signals. Crucially, the reliability of the proposed approach was verified through the phantom data with four frequently adopted voxel sizes (*Figure 2-2*), and the PICSO index was shown to be more sensitive to the resulting rsFC than the tSNR was. Second, our analysis of the various spatial resolution revealed that reducing the acquired image resolution or adopting a large smooth kernel increased the rsFC and physiological contributions, which is consistent with previous reports (Molloy et al., 2014; Triantafyllou et al., 2005; 2006). In brief, we achieved the following three aims of this study: (1) calibrating the PICSO estimation procedures by using a phantom, (2) verifying the high sensitivity of PICSO for detecting the CS (*Figure 2-6*), and (3) determining that the acquired voxel size had a larger effect on the PICSO than the smoothness did (lower panels in *Figure 2-4* and *Figure 2-5*). Moreover, the PICSO index has the advantages of avoiding additional acquisition, facilitating a practical quality evaluation for existing fMRI databases derived from a large sample, and enhancing the rs-fMRI reliability of future

36
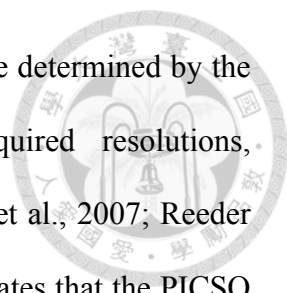
clinical investigations. Notably, however, the PICSO represent the weighting of physiological fluctuations over the thermal noise of a single voxel, whereas the CS is the temporal correlation between two voxels or regions. They differ conceptually, and their relationship is described as follows. High CS outcomes in regions must result from the sufficient PICSO (high physiological contribution) values in these regions; however, regions with high PICSO values do not directly indicate their FC. Accordingly, the linear correlation between the CS and PICSO (*Figure 2-6*) was medium to large when different noise levels were modulated (by imaging resolution or spatial smoothing), but in actuality (with a fixed noise level), the PICSO can only be regarded as the prior reliability measure for the rsFC.

According to the physiological noise model in BOLD-fMRI (Krüger et al., 2001; Triantafyllou et al., 2005), the PICSO index was proposed to approximately estimate the contribution of intrinsic spontaneous activities by estimating the ratio of σ_p over σ_0 in a voxel-wise manner without additional sequence editing. Between these two parameters, estimating σ_0 is more uncertain and difficult due to the existence of multiple approaches for doing so. The approach of estimating σ_0 without RF excitation has recently been well adopted because it is a straightforward concept, but its requirements of extra sequence editing and image reconstruction greatly lengthen the time required for experiments and analysis, rendering it almost impossible to apply to existing RS-fMRI data sets (Kellman and McVeigh, 2005; Triantafyllou et al., 2011). For image processing, a general method for estimating σ_0 is to calculate the spatial variance within a selected ROI outside of the brain region, and a subtractive imaging method was employed to subtract images from the selected two adjacent images and estimate the thermal noise in an ROI manner (Reeder et al., 2005). However, these
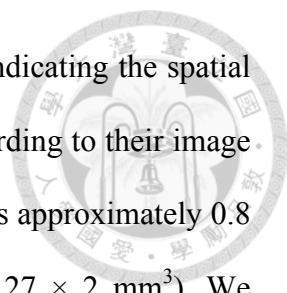
ROI-based methods are not designed for generating a voxel-wise map and lack temporal information for rsFC. By contrast, we used a series of subtractive images from every two adjacent time points to enable accurate measurement of local σ_0, regardless of the image spatial noise, and to enable the practical application of the proposed method to existing rs-fMRI data sets. This subtractive strategy was based on two assumptions: (1) the temporal thermal noise follows a Gaussian distribution (Wink and Roerdink, 2006), and (2) the resting-state spontaneous activity does not change quickly for each pair of adjacent time point. If either assumption is violated by the rapid signal changes because of a subject's head motion, then the robustness and accuracy of the PICSO estimation might decrease. Thus, for preprocessing, the rs-fMRI data were processed using motion correction and despiking to minimize the motion impact prior to the PICSO calculation. Although no existing motion correction methods could guarantee that the data were completely free from motion, the residual motion effect in our approach would be considered as the thermal noise because of the high-frequency enhancement by the subtractive strategy, thus reducing the PICSO value. Under the general inclusion criteria with the mean FD of less than 0.3 in our data set, the PICSO value showed no correlation with the mean FD, suggesting that head motion does not affect the PICSO.

Moreover, any slight signal drift during image acquisition also affects the PICSO estimation; hence, this drift should be corrected using the detrending procedure, the order of which might differ among scanners. In our preprocessing, the detrending order was set to the third order on the basis of the phantom verification because, in the phantom data, when the total fluctuation level is equal to the thermal noise; this indicates no physiological fluctuation contributions. Our phantom results (*Figure 2-2a*, with various acquired voxel sizes) verified the assumptions in the plot of σ versus σ_0

38

that followed the identity line after detrending, and the thermal noise determined by the proposed approach showed high stability under various acquired resolutions, demonstrating the reliability of the subtractive procedure (Dietrich et al., 2007; Reeder et al., 2005; Triantafyllou et al., 2011). Moreover, *Figure 2-6* illustrates that the PICSO and CS were positively correlated, but the tSNR and CS did not show a significant correlation. Therefore, according to the two assumptions, PICSO estimation can be a convenient quality-assurance measure in the preprocessing procedure for rs-fMRI data sets. Notably, a higher PICSO value was displayed in the visual cortex compared with that in the THAL (*Figure 2-3*), which is consistent with the findings of Bianciardi et al. (2009). They also reported that the visual cortex showed higher sensitivity to the spontaneous activity than the entire gray matter did (Bianciardi et al., 2009). Because the rs-fMRI signals are based on the BOLD mechanism, the PICSO inhomogeneity among the brain regions implied a regional disparity in the cerebrovascular structure.
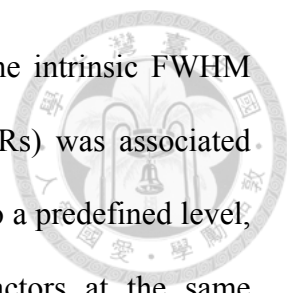
The off-diagonal upper panels in *Figure 2-4* and *Figure 2-5* reveal the substantial influence of the spatial resolution on the rsFC, showing that the PICSO (lower panels in *Figure 2-4* and *Figure 2-5*) is an effective index for reflecting the FC changes. The results indicate that the brain areas with low PICSO values were confounded by thermal noise, causing a low CS and reducing the spatial extent. This may explain why studies have seldom reported high-resolution rsFC results without spatial smoothing. Although the relationship between the PICSO and CS was explicit, the PICSO values were lower than anticipated (approximately 0.00–0.95). To ascertain the confidence level, as a reference in the PICSO estimation, we examined the data sets of Bianciardi, who estimated the contributions of various noise sources in rs-fMRI data by using regression approaches (Bianciardi et al., 2009). After the signal drift and nonneuronal fluctuations were removed, the fMRI variance of Bianciardi's 7T data sets resulted in a PICSO value

39

of 0.6 in the whole brain gray matter and 1.7 in the visual cortex, indicating the spatial specificity of the PICSO value among brain regions. Similarly, according to their image resolution ($1.25 \times 1.25 \times 2$ mm^3), the PICSO in the visual cortex was approximately 0.8 in the visual cortex of our high-resolution 3T data set ($1.27 \times 1.27 \times 2$ mm^3). We concluded that this PICSO value was reasonable because the PICSO index is linearly proportional to the field strength, which is consistent with Huettle's statement that "while thermal noise increases linearly with increasing field strength, physiological noise increases quadratically with the field strength" (Chu et al., 2012). In current hardware settings, although the PICSO value in subcortical regions is low compared with the thermal noise level, this difficulty can be alleviated through spatial smoothing (*Figure 2-4*) or elevating the field strength.
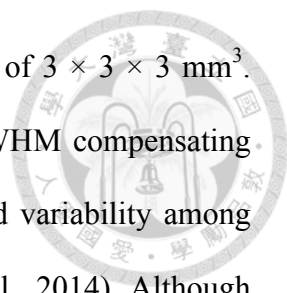
Traditional spatial smoothing in fMRI preprocessing involves applying a smooth kernel with a fixed kernel size rather than smoothing until a uniform point-spread-function is reached, a procedure that was performed in this study. However, uniform smoothing was necessary in the current study to control the effective spatial resolution (i.e., the FWHM level) and to compare the PICSO and CS with the same criteria. Moreover, the artificial connectivity induced by head motion has attracted global attention in the rs-fMRI field (Power et al., 2014); applying uniform smoothness facilitates minimizing the motion-induced variability among participants (Scheinost et al., 2014). The intrinsic blurring factors related to motion were minimized because the uniform smoothing performed using 3dBlurToFWHM entailed employing an iterative estimation scheme until an approximation of the desired smoothness was reached.

The PICSO value was inversely related to the effective spatial resolution and was affected by the acquired voxel size and the applied spatial smoothing. We defined the

40

spatial resolution of the acquired voxel size (SRv) according to the intrinsic FWHM before smoothing, whereas the spatial resolution of smoothing (SRs) was associated with the final elevated FWHM (after the smoothing was executed) to a predefined level, regardless of high-resolution acquisition. Comparing the two factors at the same effective spatial resolution revealed that the SRv reduced σ_0 substantially more than the SRs did. In addition, increasing the voxel size increased the σ/σ_0 ratio, thus enhancing the PICSO value. At the same FWHM, spatial smoothing did not enhance the PICSO as significantly as the voxel size effect did. These results accord with those of a previous study, in which the significance of the acquired spatial resolution to the σ/σ_0 ratio exceeded that of the smoothing (Triantafyllou et al., 2006).

Consistent with a previous study (Triantafyllou et al., 2006), spatial smoothing greatly enhanced the tSNR, particularly for the data acquired at a high spatial resolution. For example, before spatial smoothing, the average tSNR (±SD) in the PCC increased from 32.8 (±1.9) to 60.5 (±7.4) and to 79.9(±11.2) as the voxel size was increased from $1.3 \times 1.3 \times 2$ to $2 \times 2 \times 2$ mm and to $3 \times 3 \times 3$ mm^3, respectively. After data sets were spatially smoothed to a fixed FWHM of 5 mm, the average tSNR was 110.3 (±17.0), 115.4 (±22.6), and 105.0 (±19.3) under the aforementioned three acquired voxel sizes, respectively. However, after the data sets were smoothed to a fixed FWHM of 3 mm (*Figure 2-4* and *Figure 2-5*), the group-level rsFC with an acquired resolution of $2 \times 2 \times 2$ mm^3 was significantly higher than that with an acquired resolution of $1.3 \times 1.3 \times 2$ mm^3 in the voxel-wise paired *t* test (uncorrected p < 0.01), suggesting that the rsFC was more enhanced by increasing the acquired voxel size than by increasing the smoothness. Visual inspection revealed that, when the effective spatial resolution was set at $3 \times 3 \times 3$ mm^3, as shown in *Figure 2-4*, the group-level rsFC with an acquired voxel size of 2×2

$\times$ 2 mm^3 was slightly higher than that with an acquired voxel size of 3 $\times$ 3 $\times$ 3 mm^3. This could be due to the strategy of smoothing to a predefined FWHM compensating for the confounding factors caused by head motion, which reduced variability among participants and thus enhanced the statistical results (Scheinost et al., 2014). Although the group-level connectivity maps from both acquired voxel sizes appeared to differ, no significant difference was observed in the voxel-wise paired t test (uncorrected p < 0.01). Overall, we suggest acquiring data at the desired resolution, rather than smoothing the high-resolution fMRI data to produce reliable rsFC.

We present the PICSO index as an approximate index for estimating the contributions of physiological fluctuations in spontaneous rs-fMRI oscillations without requiring additional sequence editing or time-consuming ROI selection. In this study, we carefully calibrated the PICSO index by using the phantom data sets at the first step. Second, the resulting PICSO and CS exhibited a high correlation in the thalamic network and DMN. Finally, at a fixed effective spatial resolution, the PICSO values were more enhanced by increasing the acquired voxel size than by increasing the smoothness. These results suggest that, for producing robust rs-fMRI outcomes, directly acquiring functional data at a low spatial resolution is more effective than performing smoothing after acquiring high-resolution data sets. Caution should be exercised when conducting high-resolution acquisition of rs-fMRI signals. In summary, we propose that the PICSO index is an effective sensitivity indicator for rs-fMRI signals, which can be integrated with existing preprocessing procedures to enable quality assurance for future rs-fMRI studies.
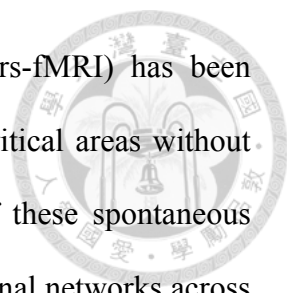
Chapter 3

Combining Regional Homogeneity and Meta-Analysis to Improve Preoperative Language Mapping with Resting-state fMRI

3.1 Introduction

The most common application of current clinical fMRI is for localization of eloquent cortex in the brain to support neurosurgical intervention to reduce the risk of postsurgical functional deficits (Matthews et al., 2006). With the use of intermittent periods of task and baseline, fMRI has been widely used as pre-operative mapping approach to non-invasively localize functional anatomy to be avoided during surgery (Dimou et al., 2013; Giussani et al., 2010), such as the task of silent word generation to localize frontal gyrus for expressive language activation (Black et al., 2017). Despite its clinical utility, the effectiveness of presurgical task-fMRI mapping is frequently compromised by patient's inadequate compliance due to neurological deficits or altered behavior capabilities (Bookheimer, 2007; Pujol et al., 1998). Sedation cannot be used because the patient must stay awake to perform tasks during the imaging procedure. Thus, these challenges often limit the application of task-fMRI for preoperative functional localization.

As an adjunct to task-fMRI, resting-state functional MRI (rs-fMRI) has been considered as a means of presurgical mapping tool to localizing critical areas without task engagements. By measuring the temporal synchronization of these spontaneous low-frequency fMRI oscillations (< 0.1 Hz), the resting-state functional networks across spatially distinct brain regions can be identified from rs-fMRI signal (Bandettini, 2012; Biswal et al., 1995). Additionally, it can be performed when patients are during early sleep stages (Fukunaga et al., 2006) and light sedation (Greicius et al., 2008), expanding its applicability to patient populations incapable to comply with the task paradigm. Recent studies have shown its feasibility of localizing motor and language networks in patients with brain tumors (Branco et al., 2016; Cochereau et al., 2016; Mitchell et al., 2013; Sair et al., 2016; Tie et al., 2014).

One common approach for detecting rs-fMRI networks is the seed-correlation analysis, which is straightforward to correlate the extracted reference time courses against every voxel in the brain, but it imposes prior knowledge to select the reference time courses by averaging over a seed (Biswal et al., 1995; Shimony et al., 2009). As each patient's functional anatomy is unique, language-network localization has been reported to possess the substantial individual variability by stimulation mapping in a large cohort of 117 patients (Ojemann et al., 1989), and to be heterogeneous distributed across brain networks in patients with epilepsy and brain tumor (Mitchell et al., 2013). With regard to the impact of seed selection on rsFC, Sohn et al. showed that the standardized seeds across healthy subjects lead to inaccurate rsFC calculations, and Yan et al. demonstrated diverse rsFC results when placing distinct seed locations (Sohn et al., 2015; Yan et al., 2013). Therefore, the seed determination of presurgical rs-fMRI

mapping is not generalizable, not reliably detected based on anatomic landmark alone, and must be evaluated individually.

By definition, the rs-FC networks are obtained from the temporal correlation of every voxel in the brain against the average reference time courses over the specified seed region. This averaging within seed region is based on the assumption that the time curves in those neighboring voxels are well synchronized, resembling the presumption of regional homogeneity (RH). RH measures the local connectivity among neighboring voxels of rs-fMRI data, sensitive to the neurophysiological metabolism and neurological diseases (Jiang and Zuo, 2016). Leveraging from RH, previous study on healthy subjects demonstrated that the uncertainty of seed selection was reduced and the sensitivity of rs-FC detection was improved (Yan et al., 2013). In this study, we propose a novel method that further confines the data-driven RH map within the functional anatomy based on meta-analysis (MA) to guide the seed selection for seed-based rs-fMRI language mapping in patients with brain tumors. The effectiveness of the proposed approach was verified by comparing three methods in mapping the individual language network: RH+MA (new method), MNI-based seeding approach (general method for normal population) and the task-fMRI activation (taken as gold standard for individualized mapping). Therefore, two hypotheses were made: (1) the performance of mapping language network guided by RH+MA approach is improved compared to that guided by the general seeding approach using MNI coordinate, and (2) the mapping results by the new approach is equivalent to the seed localization guided by task-fMRI activation.

3.2 Material and Method

3.2.1 Participants

Patients undergoing surgical resection of brain lesion participated in this study, approved by the Institutional Review Board at MD Anderson Cancer Center. Before inclusion, written informed consent was obtained from each patient in accordance with the guidelines. Twenty-five patients with lesion close to language areas, out of the seventy-five patient pool, were included in the following analysis.

3.2.2 Data Acquisition

Presurgical mapping of the language network for each patient was requested by the neurosurgeon because the tumor located near the cortical and subcortical language areas. The imaging datasets inclusive of language task-fMRI, rs-fMRI, and 3D T_1-weighted (T_1w) imaging were acquired on a 3T clinical scanner (GE Healthcare, Milwaukee, WI, USA). For fMRI acquisition, a T_2^*-weighted gradient-echo EPI (GE-EPI) sequence was used with the following parameters: repetition time (TR)/echo time (TE) = 2000/25 ms, flip angle = 90°, 32 slices with 4-mm thickness and no gap, in-plane resolution = 3.75 mm × 3.75 mm, parallel imaging with acceleration factor of 2. The 3D T_1w image was acquired using a gradient-echo sequence (TR/TE/inversion time = 7.4/2.1/400 ms; flip angle = 20°; 124 slices with .94 × .94 × 1.2 mm³ voxels). Language task-fMRI included a letter fluency (LETT), a category fluency (CAT), and a sentence completion (SENT) paradigm. A total of 130 image volumes were obtained from each of the first two paradigms, which started with a 20-s rest period, followed by six cycles of 20-s task block and 20-s rest interval. For the sentence completion paradigm, a total of 120 image volumes were obtained without the last 20-s rest interval. For rs-fMRI, patients were asked to keep their eyes closed, not move their head, not fall asleep, and not think of anything in particular. The acquisition period was 6 min (a total of 180 volumes).
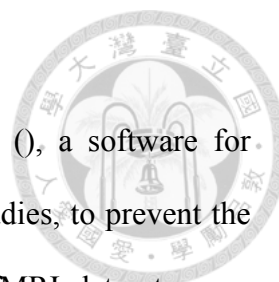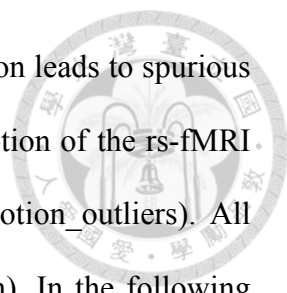
3.2.3 Task-fMRI Analysis

All analyses were analyzed in the native space using IClinfMRI (), a software for integrating fMRI techniques in presurgical mapping and clinical studies, to prevent the additional spatial smoothing induced by normalization. The task-fMRI datasets were processed using the *Task fMRI* module with the default procedures, including motion correction, aligning to a T_1w image with a 2-mm isotropic grid based on coordinate-based registration, de-spiking, spatial smoothing with a 4-mm FWHM 3D Gaussian kernel, and GLM analysis. Task-fMRI activation map was determined by setting a *t* threshold and a cluster-size threshold, corresponding to AlphaSim corrected *p* < 0.05. For measuring the spatial concordance across three task-fMRI results at individual level, the corrected activation maps were transformed as binary masks, and the binary masks of three task-fMRI were summed and then divided by three to form an individual concordance map (Fig.3-6). The individual concordance map was used to generate the task-guided seed for rs-FC analysis on each individual. Furthermore, to verify the spatial consistency of functional localization across three seeding approaches, a union mask (the united regions of three task-fMRI masks) was prescribed for two purposes: (a) using the union mask as the gold-standard of language-mapping for each patient (native space), and (b) normalizing the union mask to the MNI space (standard space) to generate one normalized probabilistic map of language network from task-fMRI across patients.

3.2.4 Rs-fMRI Analysis by Incorporating Data-driven Regional Homogeneity

The rs-fMRI data were preprocessed in the *Resting-state fMRI* module with the default procedures: slice timing, motion correction, realignment, de-spiking, detrending, regressing out covariates (included six motion parameters and fluctuations averaged over two masks of white matter and cerebrospinal fluid), band-pass filtering of 0.01–

0.08 Hz, and a 4-mm FWHM spatial smoothing. Because head motion leads to spurious correlations in rsFC (Power et al., 2012), we examined the head motion of the rs-fMRI data set using mean framewise displacement (FD) by FSL (fsl_motion_outliers). All rs-fMRI data fulfilled the motion criteria (i.e., mean FD < 0.3 mm). In the following RH+MA method, we applied the meta-analysis (MA) to constraining the seed candidates within language network and refined the seed-selection process by regional homogeneity (RH). The MA map was downloaded from Neurosynth using the term "language", resulting in 885 studies, (Yarkoni et al., 2011) and constrained the results within the language regions-of-interest (ROI). This ROI encompasses bilateral middle frontal gyrus, bilateral inferior frontal gyrus, bilateral angular gyrus, bilateral supramarginal gyrus, and bilateral superior temporal gyrus, implemented by using the LONI Probabilistic Brain Atlas (Shattuck et al., 2008). The RH map was calculated before spatial smoothing and confined within a mask obtained from inversely normalized MA map from MNI space to the native space using SPM12, as demonstated in **Figure 3-*1***. Next, seed placements of the rs-fMRI data were positioned at local maxima of the RH map in the meta-analysis mask of the anterior/posterior portion of the language network (traditional Broca's/Wernicke's area). Local maxima of RH+MA map were conducted in a voxel-wise manner using AFNI (3dExtrema with the option of "-volume", "-interior", "-strict", and "-data_thr"), where a local maximum was determined if the value of given voxel is higher than its 26 neighbors. To reduce the number of seed candidates within RH+MA map, a threshold was defined by 70 percentage of a maximum (**Figure 3-*2***), which is inspired by an automatic threshold determination method (Voyvodic, 2006).
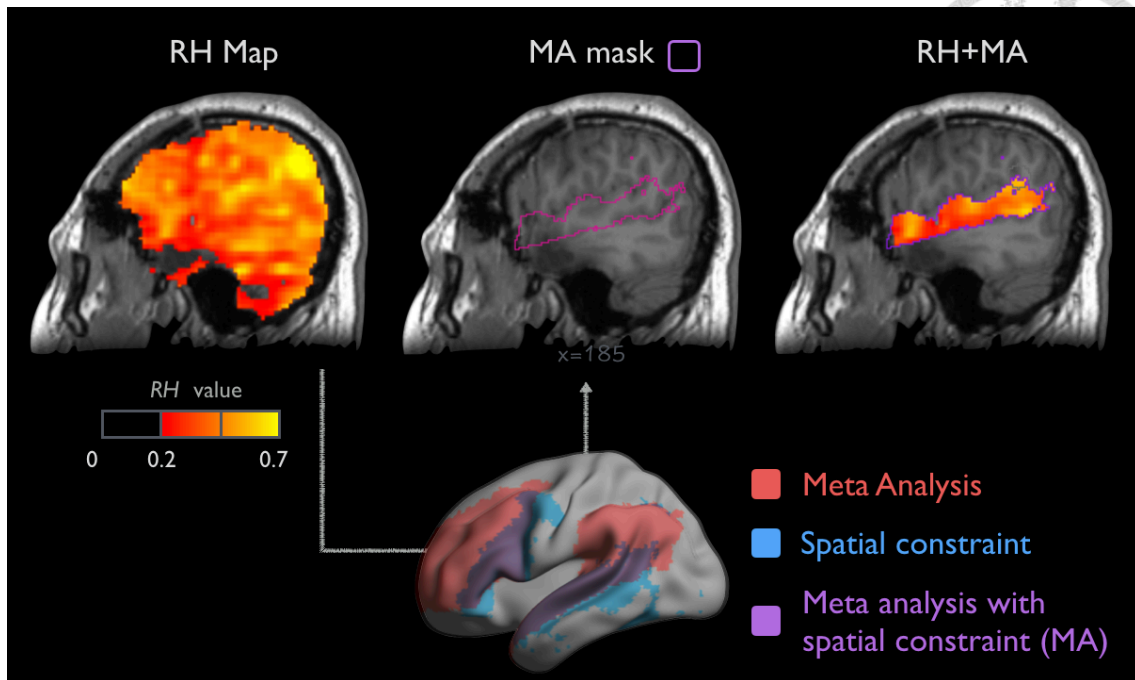
Figure 3-1 The demonstration of RH+MA approach on a representative case

The rsFC maps were calculated with a 6-mm spherical seed centering on local maxima of RH+MA map. Generally, for those cases with lesion sites in left temporal-occipital/temporal-parietal lobe, the seeds were placed on anterior part of the language network. In contrast, for those cases with lesion sites in left frontal lobe, the seeds were placed posterior part of the language network.
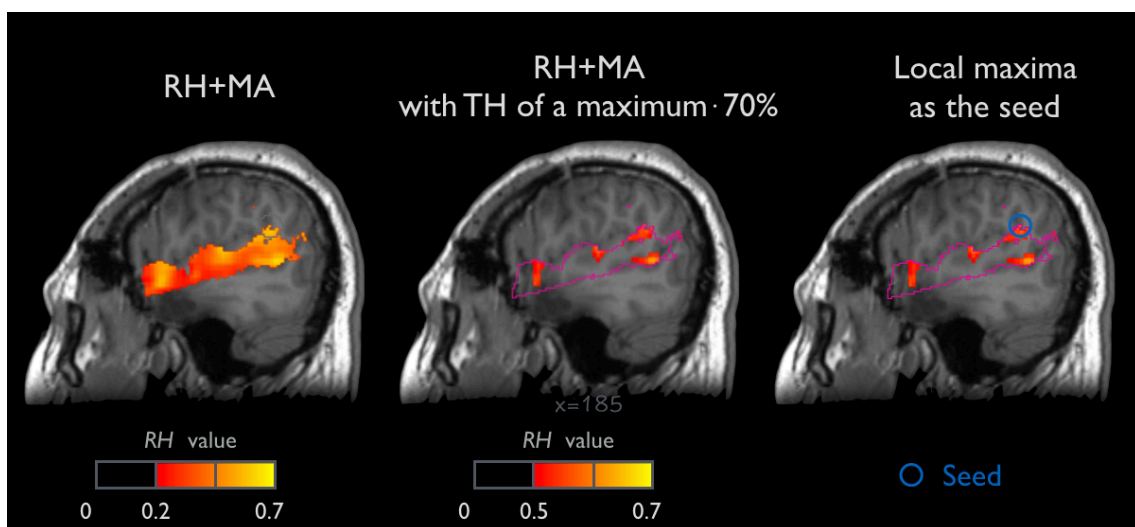
Figure 3-2 Illustration of searching seed candidates and identifying one of local maxima on a representative case

49

3.2.5 Rs-fMRI Analysis by Alternative Approaches

For comparing RH+MA approach against alternative seed-selection approaches, we conducted a seed-based correlation analysis guided by task activation (the personalized perspective) and that guided by MNI coordinate (the research perspective). In rsFC guided by task-fMRI, the areas of the maximum value within an individual concordance map were overlapped to each of the task activation maps, forming seeds for following rsFC analysis. **Figure 3-*3*** shows that the seed was positioned at a local maximum of single task activation maps within language ROI distant from the lesion. In rsFC guided by MNI coordinates, the 6-mm spherical seeds (Rosazza et al., 2014; Yan et al., 2013; Zhang et al., 2009) of traditional Broca's area and Wernicke's area were centering on (−51, 27, 18) and (−51, −51, 30), respectively. The adopted coordinates were in line with previous studies (Tomasi and Volkow, 2012; Zhu et al., 2014) and their spatial location in both render and planar view were shown in **Figure 3-*4***.
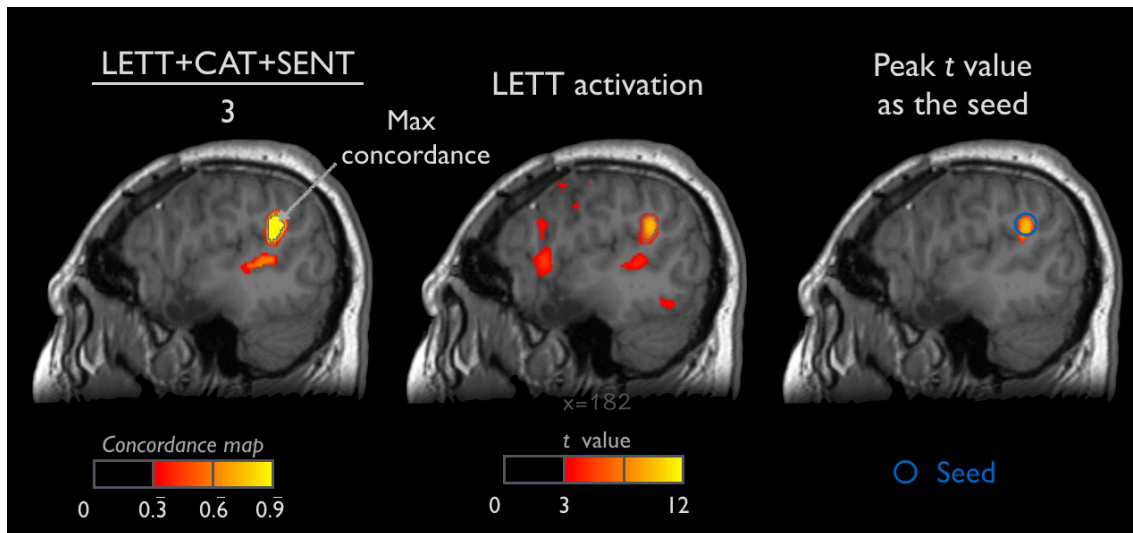
Figure 3-3 Illustration of seeding on a peak value of a task t-statistic map for a representative case
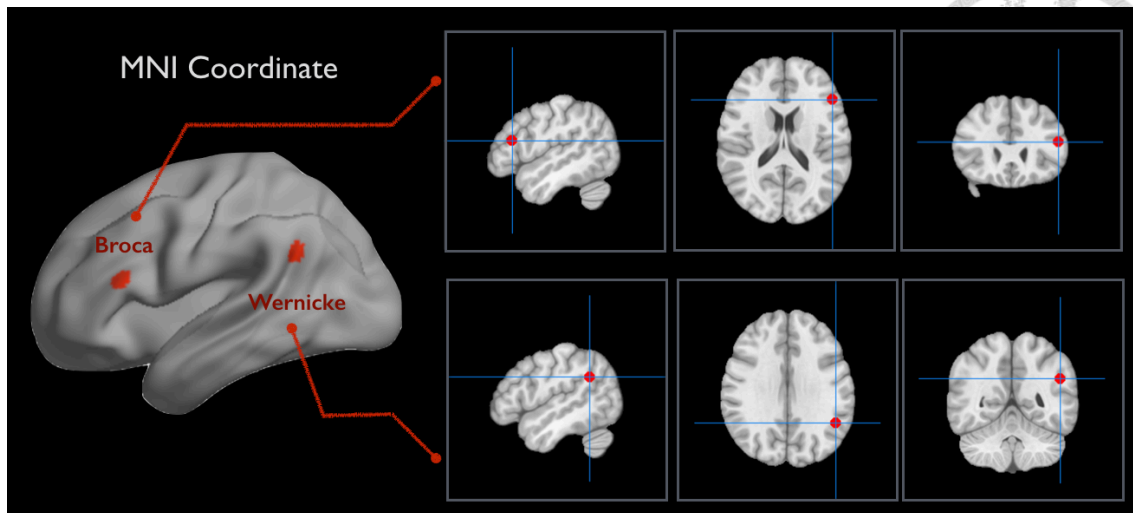
Figure 3-4 Location of seed ROIs adopted in the present study

3.2.6 Identification of Language Network form Rs-fMRI Maps

To identify language network but exclude default mode network from each patient's rs-fMRI maps, we performed a semi-automated template-matching procedure. First, we calculated the overlay of each rs-fMRI map against the predefined templates of default mode network and predefined language ROIs (Fedorenko et al., 2010; Mahowald and Fedorenko, 2016; Yarkoni et al., 2011). These language ROIs were derived from single-subject analysis and validated to represent functional characteristic of language regions in a large group of 220 healthy subjects (Fedorenko et al., 2010; Mahowald and Fedorenko, 2016) and then combined into a single binary mask as a language network template (LNT), including the left medial frontal gyrus (MFG), the left inferior frontal gyrus (IFG), the left inferior frontal gyrus pars orbitalis (IFGorb), the left angular gyrus (AngG), the left posterior temporal (PostTemp), as well as the left anterior temporal (AntTemp) regions (**Figure 3-5**). The default mode network template (DMT) was downloaded from Neurosynth with the option of reverse inference using the term "default mode" derived from 516 studies (Yarkoni et al., 2011).

51
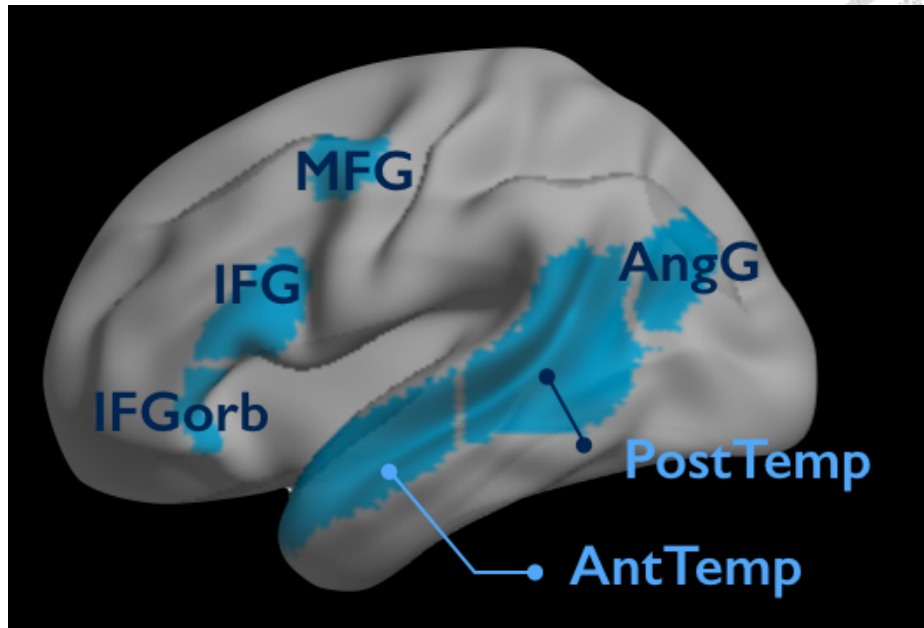
Figure 3-5 Location of Language ROIs provided by Fedorenko et al.

In template-matching procedure, the Dice coefficient between a template (DMT/LNT) and rsFC map was calculated to quantify the spatial similarity between two binary masks (Rombouts et al., 1997; Tie et al., 2014). The Dice coefficient, between 0 and 1, provides an objective measure of overlap between the voxel numbers within the two masks (template and rsFC map in this study). Higher Dice coefficient represents higher similarity between masks, as noted by the following equation.

$$Dice\ coefficient = \frac{2 \cdot Voxel\#_{Template \cap rsFC}}{Voxel\#_{Template} + Voxel\#_{rsFC}}$$

Since the Dice coefficient quantifies the proportion of supra-threshold voxels between measurements, it varies according to the threshold used. For this reason, we calculated Dice coefficients between a template and a rsFC map at a fixed z threshold of 0.5. Because of multiple resulting rsFC maps, the rsFC map with a higher Dice coefficient in LNT than that in DMT was selected for the language-network mapping.

52
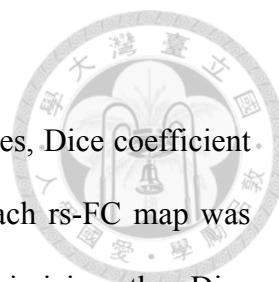
3.2.7 Comparison among Seed-correlation Rs-fMRI approaches

For quantitative comparison among three rs-fMRI seeding approaches, Dice coefficient between the union mask (of three binary task-fMRI masks) and each rs-FC map was calculated. Thresholds of rsFC maps were optimized by maximizing the Dice coefficient, starting at a z value of 0.5 with a 0.05 increment. The Dice coefficients across rs-fMRI seed-guiding approaches were compared by using a one-sided Wilcoxon signed-rank test due to non-normally distributed nature of the Dice coefficient.

3.3 Result

Among the 25 patients, 15 had lesions near Wernicke's area and 10 near Broca's area. **Figure 3-*6a*** demonstrates that significant activations ($p < 0.05$, corrected) were detected in left middle frontal areas for three task paradigms, left inferior frontal areas and left inferior parietal for task paradigms of LETT and SENT.
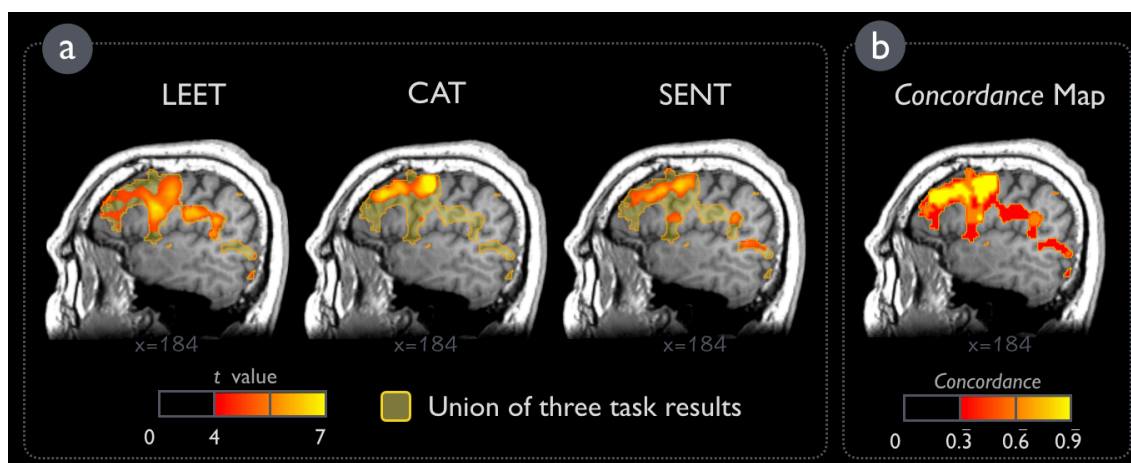
Figure 3-6 The significant activations of letter fluency (LETT), category fluency (CAT), and sentence completion (SENT), and the concordance map of three tasks

Figure 3-*7* illustrates the language rs-FC mappings at a fixed threshold guided via the three methods: MNI coordinate, task activation, and RH+MA approaches for a representative patient. The rsFC maps guided by both task activation and RH+MA

53

approaches showed scattered hot spots in left inferior frontal/parietal regions, supramarginal gyrus, and superior temporal gyrus (*Figure 3-7 b-c*), whereas that guided by MNI coordinate showed no connectivity results in left frontal regions (*Figure 3-7a*).
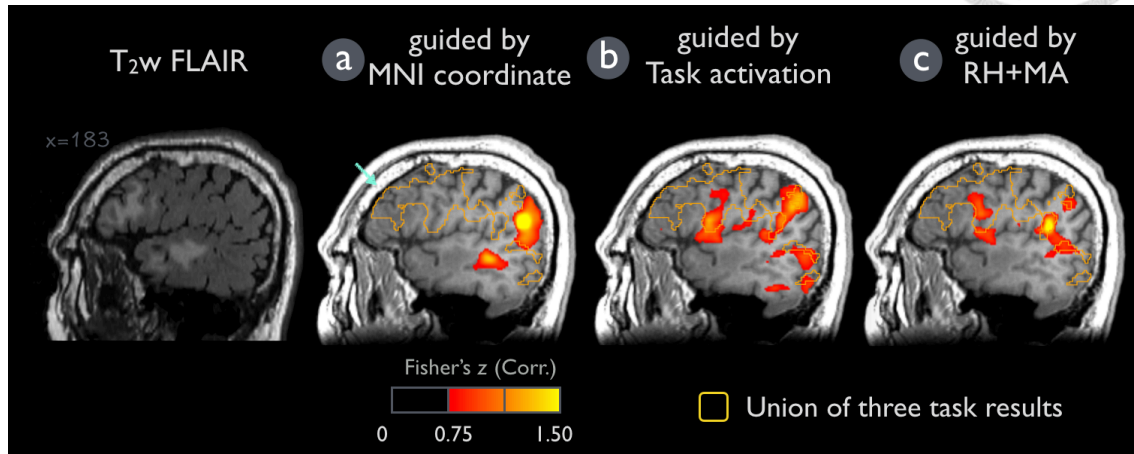
Figure 3-7 The seed-based rs-fMRI mapping guided by MNI coordinate, task activation, and RH+MA approaches. Language maps from a representative subject

Table 3-1 presents the mean FD (motion parameter) and Dice coefficient for each patient determined from the whole brain and the language ROI. In the whole brain, Dice coefficient was on average 0.171 ± 0.109, 0.220 ± 0.086, and 0.216 ± 0.103 for rs-fMRI guided by MNI coordinate, by task-fMRI, and that by RH+MA map, respectively. In the language ROI, the Dice coefficient was 0.357 ± 0.176 with rs-fMRI guided by MNI coordinate, 0.441 ± 0.155 with rs-fMRI guided by task activation map, and 0.438 ± 0.159 with rs-fMRI guided by RH+MA map. As presented in **Figure 3-8**, in both whole brain and language ROI, the performances of mapping language network guided by RH+MA approach were significantly improved compared to that guided by the general seeding approach using MNI coordinate [$Z = 2.05$, $p < 0.05$ for whole brain, $Z = 2.36$, $p < 0.05$ for language ROI]. Moreover, the rs-fMRI mapping results by the RH+MA approach showed no significant differences to the seed localization guided by task-fMRI

54

activation coordinate [$Z = -0.23$, $p = 0.59$ for whole brain, $Z = -0.46$, $p = 0.68$ for language ROI].
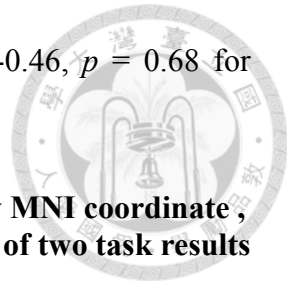
Table 3-1 Dice coefficients between resting-state maps (guided by MNI coordinate , guided by task activation and guided by RH+MA) and the union of two task results for the whole brain and within language ROI

Patient	Lesion close to	mean FD of rs-fMRI data	Dice for Whole Brain			Dice for Language ROI		
			guided by MNI Seed	guided by task	guided by RH+MA	guided by MNI Seed	guided by task	guided by RH+MA
P1	Wernicke	0.210	0.268	0.215	0.255	0.585	0.541	0.535
P2	Wernicke	0.080	0.231	0.233	0.229	0.544	0.481	0.496
P3	Wernicke	0.184	0.166	0.235	0.103	0.193	0.270	0.215
P4	Broca	0.163	0.064	0.377	0.289	0.202	0.518	0.497
P5	Broca	0.107	0.158	0.194	0.202	0.336	0.526	0.517
P6	Wernicke	0.116	0.152	0.143	0.112	0.347	0.438	0.445
P7	Wernicke	0.281	0.135	0.140	0.119	0.385	0.359	0.413
P8	Broca	0.035	0.344	0.249	0.189	0.331	0.475	0.362
P9	Broca	0.055	0.094	0.110	0.105	0.529	0.629	0.459
P10	Wernicke	0.201	0.242	0.220	0.230	0.482	0.429	0.469
P11	Broca	0.141	0.052	0.124	0.147	0.187	0.373	0.371
P12	Broca	0.067	0.111	0.254	0.173	0.261	0.287	0.296
P13	Wernicke	0.086	0.192	0.187	0.258	0.354	0.534	0.331
P14	Wernicke	0.266	0.401	0.373	0.420	0.609	0.704	0.668
P15	Wernicke	0.180	0.033	0.135	0.215	0.085	0.079	0.634
P16	Wernicke	0.052	0.170	0.243	0.234	0.454	0.578	0.552
P17	Wernicke	0.094	0.414	0.262	0.453	0.690	0.242	0.711
P18	Broca	0.134	0.051	0.227	0.243	0.207	0.513	0.527
P19	Broca	0.156	0.117	0.188	0.194	0.207	0.190	0.188
P20	Wernicke	0.103	0.070	0.082	0.148	0.284	0.258	0.371
P21	Broca	0.113	0.038	0.120	0.043	0.057	0.429	0.035
P22	Broca	0.054	0.161	0.228	0.141	0.199	0.520	0.276
P23	Wernicke	0.136	0.113	0.429	0.450	0.334	0.606	0.635
P24	Wernicke	0.053	0.307	0.197	0.231	0.654	0.398	0.537
P25	Wernicke	0.130	0.180	0.336	0.223	0.420	0.658	0.405
Mean (SD)		0.128(0.066)	0.171(0.109)	0.220 (0.086)	0.216(0.103)	0.357 (0.176)	0.441 (0.155)	0.438 (0.159)
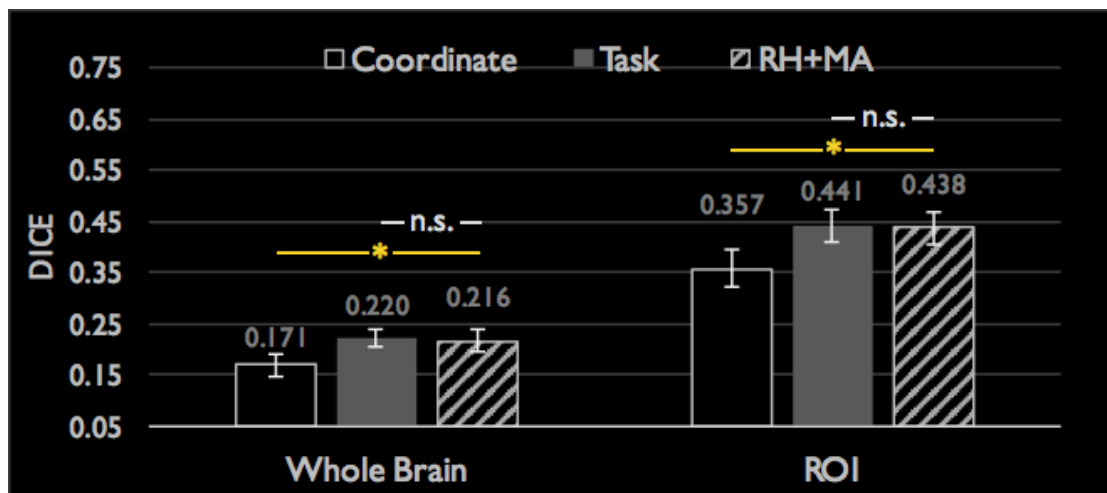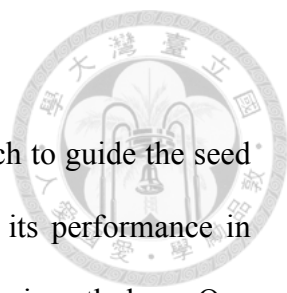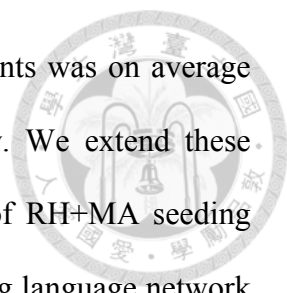
Figure 3-8 Bar plot representation of Dice coefficents in rs-fMRI language mapping guided by three seeding approaches for the whole brain and within language ROI (*$p < 0.05$)

3.4 Discussion

The goal of this study was to propose a novel RH+MA approach to guide the seed selection of mapping the rs-fMRI language network and to verify its performance in detecting language areas as do task-guide approach, in patients with brain pathology. One of the advantages of the proposed seeding approach was that it is data-driven and automatically selects the potential seed candidates by incorporating the measure of local connectivity among neighboring voxels of rs-fMRI data within the target language network. We assessed quantitatively the degree of correspondence among three seed-based rs-fMRI analyses (guided by MNI coordinate, task, and RH+MA approaches) and a union of activation maps obtained by performing three language task-fMRI for pre-surgical planning, with reference to Dice coefficient of rs-fMRI with respect to task-fMRI. Our results demonstrated that performance on localizing language network guided by RH+MA approach was significantly improved comparing to that by the general seeding approach—MNI coordinate. Moreover, we found that rs-fMRI guided by RH+MA approach was as sensitive as that guided by task activation approach, providing advantageous potential in the clinical practice, especially in those patients who have difficulties in task compliances.

Our results showed that rs-fMRI maps guided by either task activation or RH+MA approach had a fair overlap with the maps obtained from traditional task-fMRI using GLM methods. We observed a Dice coefficient of 0.216 for whole-brain analysis when using an optimized threshold for maximizing the Dice coefficient. As the analysis confined in language ROI, the Dice coefficient increased to 0.438 in average. This increases in Dice coefficient suggested that the spatial overlap between task-fMRI and rs-fMRI depended on the adopted ROI in the analysis. These findings were in line with previous results from Branco at al., who reported that overlay between rs-fMRI using

data-driven analysis and task-fMRI using GLM method in 15 patients was on average 0.248 and 0.458 for whole brain and language ROI, respectively. We extend these findings by demonstrating that the seed-based rs-fMRI with use of RH+MA seeding approaches was helpful in optimizing the seed placement in detecting language network in patients with brain lesion.

Independent component analysis (ICA) is an alternative to seed-based analysis of rs-fMRI in presurgical mapping. However, we did not evaluate ICA in the current study for various reasons. While ICA approach provides promises in outlining language networks in both healthy controls (Tie et al., 2014) and patients with brain lesions (Branco et al., 2016; Sair et al., 2016), the choice of proper number of components is much more challenging for determining language networks due to the complex noise level, spatial, and temporal dependence of fMRI data (Li et al., 2007). Overestimated the number of independent components (ICs) results in a decrease in repeated-measure stability, whereas underestimated number of ICs lead to a merge of different brain networks as a single component. Although a previous study showed no significant effect of number of ICs from 20 to 50 on the concordance of rs-fMRI and task-fMRI (Sair et al., 2016), another contradictory observation of the noticeable changes in specificity with a fixed number of ICs lower than 50 has been reported (Branco et al., 2016). Additionally, Hui et al. compared various methods to estimate the optimal number of ICs using information theory criteria and concluded that none of perfect criteria has can be determined for fMRI data (Hui et al., 2011). Alternatively, Cochereau et al. indicated that the use of seed-based analysis achieved 80% accuracy in detecting individual language network (Cochereau et al., 2016) when selecting seeds from intraoperatively stimulated positive sites. Even though their approach is not applicable for presurgical

mapping, it demonstrated that precise seeds determination improved the detecting accuracy for language mapping derived from rs-fMRI, in contrast to ICA approach.

In conclusion, this study proposed one novel RH+MA approach to guide the seed selection in rs-fMRI mapping, which could be assistive to localize brain networks in presurgical mapping. Despite of the moderate overall concordance between task-fMRI and rs-fMRI language networks, this new method showed no significant difference in Dice coefficients comparing to the seed selection based on task-fMRI activations. Our results suggest that the proposed method can be an effective and beneficial approach to supplement the application of fMRI in the clinical practice.
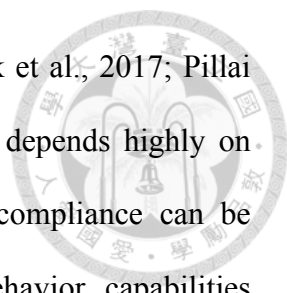
Chapter 4

IClinfMRI Software for Integrating functional MRI Techniques in Presurgical Mapping and Clinical Studies
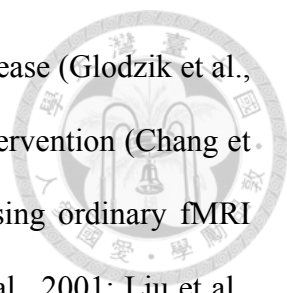
4.1 Introduction

Functional magnetic resonance imaging (fMRI) based on a blood oxygenation level–dependent (BOLD) mechanism has growing significance in clinical imaging studies for the management of neurological diseases (Matthews et al., 2006). One of the promising applications of clinical fMRI is to aid presurgical planning in order to maximize the lesion resection while preventing post-operative functional deficits (Sanai et al., 2008; Vlieger et al., 2004). With use of block-design paradigms, fMRI activations have been shown to correlate well with the clinical gold-standard—intra-operative direct cortical stimulation (DCS)—making it valuable for presurgical planning (Bizzi et al., 2008; Weng et al., 2017). However, functional brain mapping that exploits the task-fMRI technique alone presents two major challenges in patients with intracranial pathology. First, the impaired cerebrovascular reactivity (CVR) can decrease sensitivity and specificity on localizing eloquent regions near or within the lesion (Pillai and Zacà, 2011; 2012; Ulmer et al., 2003; 2004) because BOLD-fMRI relies on intact coupling between neural firing and cerebrovascular response (Harrison et al., 2002; Roy and Sherrington, 1890). Thus, CVR mapping has been recommended as an essential

59
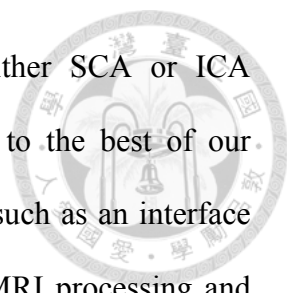
component when the reliability of fMRI mapping is a concern (Pak et al., 2017; Pillai and Mikulis, 2015). Second, since the effectiveness of task-fMRI depends highly on patients' performance and participation, ensuring adequate task compliance can be challenging in patients with neurological deficits or altered behavior capabilities (Bookheimer, 2007; Pujol et al., 1998). As an alternative to task-fMRI, resting-state fMRI (rs-fMRI) has become a promising technique in localizing brain regions in functional networks, regardless of task engagement (Mitchell et al., 2013; Quigley et al., 2001; Zhang et al., 2009). To effectively translate the aforementioned techniques for presurgical planning and fMRI studies in clinical populations, specialized clinical software is required to integrate these complementary techniques and promptly generate useful information in a clinical format before surgery or before a clinical decision is made.

Since the BOLD signal is based on neurovascular coupling, the abnormal cerebral vasculature or regional hemodynamic disruption caused by intracranial pathology can impair the CVR and invalidate the assumption of neurovascular coupling. Such neurovascular uncoupling (NVU) can potentially result in false negative errors in fMRI mapping (lack of BOLD signal despite neural activity) which may potentially contribute to an undesirable resection of eloquent cortex (Pak et al., 2017; Pillai and Mikulis, 2015; Ulmer et al., 2003). Without further confirmation by intraoperative DCS, this fMRI false negative could lead to permanent postoperative neurological deficits. Impaired CVR has been reported in brain tumors (Hsu et al., 2004; Pillai and Zacà, 2012), cerebrovascular diseases (Chang et al., 2013; Mikulis et al., 2005), and neurodegenerative diseases (Iadecola, 2004). In these cases, mapping CVR with MRI during a vasodilatation challenge would be a useful technique to indicate the NVU potential for assisting the interpretation of clinical fMRI activation (Pak et al., 2017;

Pillai and Mikulis, 2015), to detect a vascular risk in Alzheimer's disease (Glodzik et al., 2013), as well as to predict early perfusion change after vascular intervention (Chang et al., 2009b). Practically, CVR experiments can be conducted by using ordinary fMRI acquisition methods during a breath-holding (BH) task (Kastrup et al., 2001; Liu et al., 2002). The post-processing resembles task-fMRI with several modifications such as the selection of impulse response functions (Birn et al., 2008; Jahanian et al., 2016; Pillai and Zacà, 2012) and the consideration of hemodynamic delays (Birn et al., 2008; Jahanian et al., 2016). Therefore, despite its importance in clinical applications, implementation of MRI data analysis for CVR mapping requires modifications to the existing fMRI software and is a time-consuming procedure that can be difficult without the assistance of an expert.

The rs-fMRI is capable of mapping intrinsic functional networks in which the within-network spontaneous BOLD oscillations emerge in synchrony during rest (Biswal et al., 1995). The rs-fMRI has been shown to be of importance in neurosurgical applications (Lang et al., 2014) and in charactering the integrity of the brain network for a wide variety of diseases (Lee et al., 2013; Matthews and Hampshire, 2016). These networks are often detected with use of seed-correlation analysis (SCA) (Biswal et al., 1995; Shimony et al., 2009) or data-driven approaches such as independent component analysis (ICA) (Smith et al., 2009; Zhang et al., 2009). The SCA approach is straightforward and imposes prior knowledge for seed selection; however, spatial distortions and functional reorganization due to brain lesions can make seed selection difficult on the basis of anatomical landmarks alone. In contrast, although the ICA approach does not have the issues associated with seed placement, determining the proper number of components and selecting components of interest in this approach is challenging (Branco et al., 2016). Software toolboxes have been developed for

analyzing rs-fMRI data for presurgical fMRI mapping using either SCA or ICA approaches (Böttger et al., 2011; Huang et al., 2016). However, to the best of our knowledge, no existing software provides integrated visualization, such as an interface that allows the use of task-fMRI results to guide the SCA in rs-fMRI processing and directly generates results that are ready for exporting to a radiology picture archiving and communication system (PACS) and to a neurosurgical navigation system.

Although the aforementioned analyses for various fMRI modalities are feasible with existing research software such as AFNI (Cox, 1996), SPM (Welcome Department of Cognitive Neurology, Institute of Neurology, London, UK), and FSL (Smith et al., 2004) or in-house scripts, a clinical translation of these techniques in a holistic way is needed. In our study, we developed Integrated fMRI for Clinical Research (IClinfMRI) software to facilitate clinical fMRI research with applicability in presurgical fMRI planning. Beyond the independent processing of task-fMRI, rs-fMRI, and CVR mapping, IClinfMRI supports interactive rs-fMRI mapping while visualizing task-fMRI results as a guidance map, provides visualization of sites with potential NVU in fMRI results, and exports overlays of mapping results on structural MR images in presentations that can be readily sent to a clinical PACS as well as to a surgical navigation system.

4.2 Materials and Method

4.2.1 Developing Environment

The IClinfMRI software was developed on the MATLAB 2014a platform (The MathWorks, Inc., Natick, MA, USA). The software was built upon in-house scripts and calls functions in free for noncommercial-use software such as dcm2nii (https://www.nitrc.org/projects/dcm2nii/), AFNI (version 16.2.09) (Cox, 1996), and

SPM12 (v6685) (Welcome Department of Cognitive Neurology, Institute of Neurology, London, UK). The dcm2nii is used to convert images from Digital Imaging and Communications in Medicine (DICOM) to Neuroimaging Informatics Technology Initiative (NIfTI) formats. Functions in both AFNI and SPM12 are adopted for data analysis.

4.2.2 Workflow and Processing Pipeline

The IClinfMRI software has five modules: *DICOM Import*, *Task fMRI*, *Resting-state fMRI*, *CVR mapping*, and *fMRI to PACS*. **Figure 4-1** shows the schematic workflow of IClinfMRI and the functionalities provided in each module. In *DICOM Import*, DICOM images in a file folder are recognized, sorted, and converted to NIfTI files, which facilitates interoperability among research image processing software, and is saved in organized subdirectories that are named according to the series descriptions stored in the DICOM header.
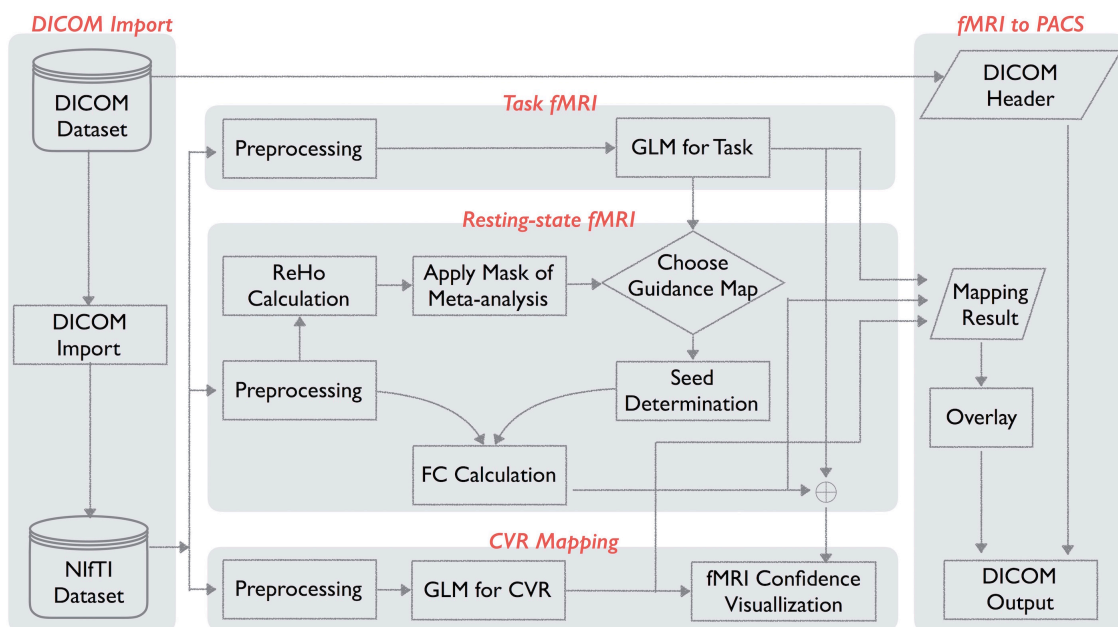
Figure 4-1 Workflow for Integrated fMRI for Clinical Research (IClinfMRI) software

Next, task-fMRI, rs-fMRI, and BH-MRI data are analyzed by modules of *Task fMRI*, *Resting-state fMRI*, and *CVR mapping*, respectively. After the analysis, the mapping results in NIfTI format are properly thresholded and overlaid on clinical structural MR images. The color-coded and gray-scale overlays are exported as a series of DICOM files by using the *fMRI to PACS* module. **Table 4-1** lists the available functions provided in each module. All temporal analyses and image registration call AFNI's functions, and image segmentation and inverse normalization (from template to individual space) call functions from SPM12. Key arguments specified in the functions are described below.

Table 4-1 Summary of IClinfMRI models and functions used to process the fMRI data
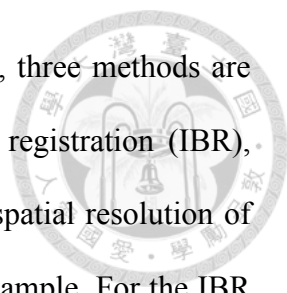
	Function	Module					Software (Function)
		DICOM Import	*Task fMRI*	*Resting-state fMRI*	*CVR Mapping*	*fMRI to PACS*	
Data input	DICOM to NIfTI	✔					dcm2nii
Pre-processing	Slice timing		✔	✔	✔		AFNI (3dTshift)
	Motion correction		✔	✔	✔		AFNI (3dvolreg)
	Aligning EPI to T_1 by coordinate-based registration		✔	✔	✔		AFNI (3dresample)
	Aligning EPI to T_1 by boundary-based registration		✔	✔	✔		AFNI(align_epi _anat.py)
	Aligning EPI to T_1 by intensity-based registration		✔	✔	✔		AFNI (align_epi_anat. py)
	De-spiking & Detrending		✔	✔	✔		AFNI (3dDespike; 3dDetrend)
	Nuisance Regression			✔			AFNI (3dBandpass)
	Segmentation		✔	✔	✔		SPM12 (Segmentation)
	Bandpass filtering			✔			AFNI (3dBandpass)
	Smoothing		✔	✔	✔		AFNI (3dmerge)

Table 4-1 Cont.

Function		DICOM Import	Task fMRI	Resting-state fMRI	CVR Mapping	fMRI to PACS	Software (Function)
				Module			
Detection	HRF-based GLM		✔				AFNI (3dDeconvolve & 3dREMLfit)
	Seed selection on the graph			✔			in-house script
	Seed preview on the graph			✔			in-house script
	Pearson correlation			✔			AFNI (3dfim+)
	Seed-based GLM			✔			AFNI (3dDeconvolve & 3dREMLfit)
	RRF-based GLM with varying latency				✔		AFNI (3dDeconvolve)
	HRF-based GLM with varying latency				✔		AFNI (3dDeconvolve) & SPM12 (HRF)
Display	Adjustable threshold, window, and color map			✔	✔	✔	in-house script
	Fusion of both fMRI and CVR maps on anatomical images				✔		
Data output	NIfTI to DICOM					✔	in-house script

Abbreviations: DICOM, Digital Imaging and Communications in Medicine; *GLM*, general linear model; *NIfTI*, Neuroimaging Informatics Technology Initiative; *CVR*, cerebrovascular reactivity; *HRF*, hemodynamic response function; RRF, respiratory response function

Functional images are motion-corrected to a reference volume with use of rigid-body registration and then resampled to an isotropic grid matching the orientation of a resampled T_1w image, which is resampled to the same isotropic grid in advance. A reference volume is the time point from fMRI data that has the fewest outliers, which are defined as the time point with its value deviant from the trend above a limit and are calculated with use of 3dToutcount. In a typical range of 50-500 time points per session, this deviation limit calculated by the default setting is approximately 5.5×MAD away from the fitted trend, where MAD is median absolute value of time series minus trend.
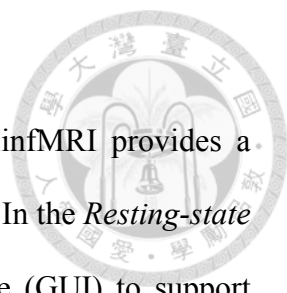
For aligning functional images into a structural T_1w image volume, three methods are incorporated: coordinate-based registration (CBR), intensity-based registration (IBR), and boundary-based registration (BBR). For the CBR method, the spatial resolution of fMRI dataset is resampled to match that of a T_1w image using 3dresample. For the IBR method, the alignment matrix is estimated by a reference volume of the functional data to a T_1w image by using the cost function of normalized mutual information (align_epi_anat.py with the option of "-dset2to1" and "-cost nmi"). For the BBR method, a high-resolution echo-planar imaging (EPI) volume with prominent tissue boundaries of gray matter, white matter (WM), and cerebrospinal fluid (CSF) is required and registered to a T_1w image using the cost function of local Pearson correlation (align_epi_anat.py with the option "-epi2anat") (Saad et al., 2009). In the study that proposed the BBR method (Saad et al., 2009), the spatial resolutions were $3 \times 3 \times 3$ mm^3 and $1 \times 1 \times 1$ mm^3 for echo-planar and T_1w images, respectively, which led to an improved registration as compared to CBR and IBR. When the users prefer BBR but their fMRI datasets are acquired at a lower resolution and the resultant echo-planar images do not have clear tissue boundaries, our software provides the option for them to use an additionally acquired single-volume high-resolution echo-planar image to determine the spatial transformation. The reference volume of the functional image data is then co-registered to the high-resolution EPI image (align_epi_anat.py with the option of "-dset2to1" and "-cost nmi"), and a concatenated transformation matrix is obtained from the two-step process. For the IBR and BBR alignment, their transformation matrix is combined with the one for motion correction; therefore, spatial transformation and image interpolation (using *wsinc5*, 3dAllineate) are performed only once for each original functional image volume. The final voxel size of aligned functional images is 2-mm or 3-mm isotropic, as determined by users.

66
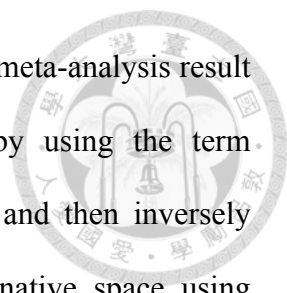
Task-fMRI activation maps are generated with use of the general linear model (GLM) by calculating the fitness of the preprocessed fMRI signal to the expected response that was constructed by convolving a canonical hemodynamic response function (HRF) with the task paradigm. During the fitting procedure, six motion parameters generated in the preprocessing step are set as the nuisance regressors, and the temporal autocorrelation structure in the residual is corrected by using the generalized least squares technique (3dREMLfit) with an autoregressive model of order 1 and moving average model of order 1, i.e. ARMA(1,1).

For rs-fMRI analysis, noise components are modeled by six motion parameters and two averaged signal fluctuations over masks of WM and CSF. These masks are generated by setting a probability threshold of 99.9% on the segments of the three-dimensional (3D) T_1w image. The 3D T_1w image was segmented into GM, WM, and CSF tissue segments using unified segmentation approach (Ashburner and Friston, 2005) in SPM12. On the basis of the probabilistic framework, this tool involved circular procedure of image registration, tissue classification, and bias field correction for optimizing the segmentation. Both masks are eroded by one voxel along each of the three axes (Jo et al., 2010) for preventing the partial volume effect on the masks and then resampled to match the spatial resolution of the aligned rs-fMRI data. It is optional to include a global signal fluctuation as an additional noise component by extracting the averaged signal from a whole brain mask produced by setting a sum of tissue probability maps of gray matter, WM, and CSF with a threshold of 30%. After removing the noise components and performing other preprocessing steps, such as the temporal filtering (**Table 4-*1***), the rs-functional connectivity (FC) map is obtained by correlating the average time series from a seed region against that from every voxel in the brain.

67

4.2.3 Unique Features

Instead of analyzing each fMRI modality independently, IClinfMRI provides a unique workflow to integrate them for clinical research applications. In the *Resting-state fMRI* module, we designed a double-panel graphical user interface (GUI) to support interactive rs-fMRI mapping while visualizing a guidance map of the user's choice for seed placement. The guidance map can be an anatomical image, a functional map processed by IClinfMRI's *Task fMRI* module, or a parametric map resulting from other research software. In this module, the seed is placed by using a simple mouse click on either of the two panels, and the seed-based FC map will be calculated, converted to a Fisher's z map, and then interactively updated on the bottom right panel of the GUI. In addition, visualization of mapping results can be easily manipulated with options that include window, threshold, opacity, and color map. Two approaches are suggested and implemented to obtain a guidance map: (1) processing task-fMRI data by using the *Task fMRI* module, and (2) calculating a regional homogeneity (ReHo) map with the use of 3dReHo (Taylor and Saad, 2013) embedded in the *Resting-state fMRI* module. The ReHo analysis summarizes the local FC by measuring the temporal similarity between a given voxel and its neighborhood with the use of Kendall coefficient of concordance (Zang et al., 2004). The ReHo map has been proposed as the alternative to guide seed selection and improve the sensitivity of rs-FC network detection (Yan et al., 2013). Besides, local activity could also contain useful information in tumor studies (Duan et al., 2016), but we have not yet incorporated this feature in our software. In our *Resting-state fMRI* module, the preprocessed rs-fMRI data before spatial smoothing was fed into the ReHo analysis for obtaining ReHo map (Zuo et al., 2013). In addition to offering the ReHo map alone, we further implemented a novel approach that seeds the connectivity analysis based on the ReHo map confined within a mask obtained from

meta-analysis (RH+MA). For the analysis of language network, the meta-analysis result was downloaded from the Neurosynth (http://neurosynth.org/) by using the term "language" that resulted from 885 studies (Yarkoni et al., 2011) and then inversely normalized the meta-analysis maps from standard space to the native space using SPM12. Since it was corrected for a false discovery rate (FDR) of 0.01, we did not apply an additional threshold but constrained the result within the brain regions covering the putative Broca's and Wernicke's areas. These brain regions included middle frontal gyrus and inferior frontal gyrus for the traditional Broca's area, and comprised angular gyrus, supramarginal gyrus, and superior temporal gyrus for the traditional Wernicke's area, implemented by using the LONI Probabilistic Brain Atlas (Shattuck et al., 2008). The final mask was then dilated for 4-mm to consider the altered functional anatomy in patients.

In the *CVR mapping* module, two types of impulse response functions are implemented, the canonical HRF (Birn et al., 2008; Jahanian et al., 2016) and the respiratory response function (RRF) (Birn et al., 2008; Pillai and Zacà, 2012), to generate the CVR map by using the GLM with an adjustable series of multiple time delays. In the voxel-wise optimization, the GLM analysis is repeated for each time delay, and the maximum t value across multiple GLM results will be selected for each voxel, to account for the varying latency of the CVR responses across the brain (Birn et al., 2008; Jahanian et al., 2016). We provide the visualization for fusions of both fMRI and CVR maps on anatomical images, which integrates the results into a single presentation. This allows the display of areas with potential NVU, that is, potential activated areas with both negative fMRI and CVR, near or within the lesion.

Presenting the mapping result in a clinical format is an essential function in software designed for clinical applications. In IClinfMRI, the *fMRI to PACS* module is

used for exporting the functional mapping result to not only color-coded but also gray-scale overlays as DICOM images that can be fed into the same patient directory in PACS and surgical navigation system, respectively. Multiple anatomical images, e.g., T_1w and FLAIR images, can be selected as underlays, for the same functional overlay to be output in the same series. For color-coded output, three sets of DICOM files are produced, one in each of the three orthogonal planes.

4.2.4 Software Installation and Use
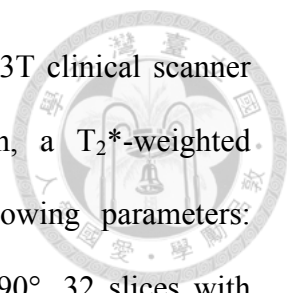
IClinfMRI is available as a zip file upon request, and the user can unzip it to a local directory. Under the MATLAB environment, the user can click "Set Path" and add the directory containing IClinfMRI to the path. IClinfMRI will run by simply typing "IClinfMRI" in Matlab. Note that IClinfMRI calls functions in dcm2nii, AFNI, and SPM12; thus, these software packages need to be installed and their functionalities verified before using IClinfMRI.

4.2.5 Illustrative Cases

Analyses of two patients are presented to illustrate the utility of IClinfMRI. Written informed consent was obtained from each patient in accordance with the guidelines and the study protocol approved by the Institutional Review Board at MD Anderson Cancer Center.

Patient #1

Patient #1 had a left temporal-occipital lesion with imaging characteristics concerning for a glioblastoma (WHO Grade IV). This dataset was used to demonstrate the rs-fMRI analysis workflow with the seed placement guided by task-fMRI results. Presurgical mapping of speech areas was requested by the neurosurgeon since the tumor was located near the cortical and subcortical language areas, in particular, the posterior part of the language network (the traditional Wernicke's area). Language task-fMRI,

rs-fMRI, T$_2$w FLAIR, and 3D T$_1$w imaging were performed on a 3T clinical scanner (GE Healthcare, Milwaukee, WI, USA). For fMRI acquisition, a T$_2$*-weighted gradient-echo EPI (GE-EPI) sequence was used with the following parameters: repetition time (TR)/echo time (TE) = 2000/25 ms, flip angle = 90°, 32 slices with 4-mm thickness and no gap, in-plane resolution = 3.75 mm × 3.75 mm, parallel imaging with acceleration factor of 2. The 3D T$_1$w image was acquired using a gradient-echo sequence (TR/TE/inversion time = 7.4/2.1/400 ms; flip angle = 20°; 124 slices with .94 × .94 × 1.2 mm^3 voxels). Language task-fMRI included a letter fluency paradigm, a category fluency paradigm, and a sentence completion paradigm. A total of 130 image volumes were obtained from each of the first two paradigms, which started with a 20-s rest period, followed by six cycles of 20-s task block and 20-s rest interval. For the sentence completion paradigm, a total of 120 image volumes were obtained without the last 20-s rest interval. For rs-fMRI, patients were asked to keep their eyes closed, not move their head, not fall asleep, and not think of anything in particular. The acquisition period was 6 min, during which a total of 180 volumes were obtained. The task-fMRI data were processed with use of the *Task fMRI* module with the following default procedures: motion correction, aligning to a T$_1$w image with a 2-mm isotropic grid via CBR method, de-spiking, spatial smoothing with a 4-mm FWHM 3D Gaussian kernel, and GLM analysis. The rs-fMRI data were first preprocessed in the *Resting-state fMRI* module with the following default procedures: slice timing, motion correction, aligning to a T$_1$w image with a 2-mm isotropic grid via the CBR method, de-spiking, detrending, nuisance regression (mask of WM and CSF), band-pass filtering (0.01–0.08 Hz), and spatial smoothing with a 4-mm FWHM 3D Gaussian kernel. Next, seed placement of the rs-fMRI data was guided by a task-fMRI map resulting from the *Task fMRI* module. For this patient, in particular, the seed was positioned at a local maximum of the

task-evoked activations near the anterior part of the language network (traditional Broca's area) because the lesion was in left temporal-occipital lobe near the traditional Wernicke's area.

In addition to fMRI, BH-MRI was also performed on the same patient, and the dataset was used to demonstrate the CVR analysis and visualization. For BH-MRI acquisition, a GE-EPI sequence was used with the same setting of fMRI parameters as described above, except that the TR was set to 3000 ms. The BH paradigm was 210 s long and comprised an initial 30-s natural breathing period, followed by three cycles of alternations between 15-s BH and 45-s natural breathing. Respiration monitoring device was used to confirm the subjects' compliance during the BH CVR MRI. The data were preprocessed by using the *CVR Mapping* module with the following setup: motion correction, aligning to a T_1w image with a 2-mm isotropic grid spatial resolution via the CBR method, de-spiking, and spatial smoothing with a 4-mm FWHM 3D Gaussian kernel. The onset time and the task duration recorded during data acquisition were set as the task paradigm. The CVR map with a BH task was generated by using a GLM model with multiple respiratory delays ranging from -10 to 15 s between the task and expected RRF.
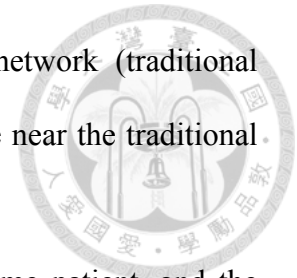
Patient #2

Patient #2 had a left temporal-parietal mass with imaging characteristics consistent with glioblastoma (WHO Grade IV). This dataset was used to demonstrate the rs-fMRI analysis workflow when no task-fMRI results were available. According to neuropsychological assessment, the patient showed significant receptive language deficits and global impairment during testing; thus, he was unable to perform a task-fMRI. Instead, the rs-fMRI acquisition was requested to provide presurgical mapping of the eloquent language areas near the lesion. The image protocol included

T_1w imaging, T_2w FLAIR imaging, and rs-fMRI. The rs-fMRI data processing was similar to that of Patient #1, except for that the seed was guided by the RH+MA map and placed at a local maximum of ReHo in the meta-analysis mask of the anterior portion of the language network.
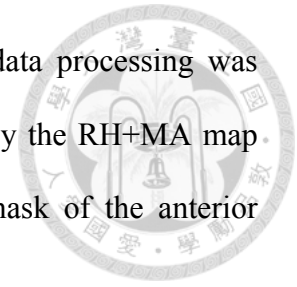
4.2.6 Validation of the rs-fMRI Workflow

To validate our software and workflow for rs-FC mapping, the rs-fMRI data for the two patients were also processed with the procedure adopted in a previous study (Hart et al., 2016) using AFNI software, independent from the IClinfMRI. The independent processing procedure and parameters were identical to ours except for the band-pass filtering (0.01–0.1 Hz), spatial smoothing (6-mm FWHM), and the diameter of the seed (10 mm).

4.3 Results

Typing "IClinfMRI" in the MATLAB command window opens the main GUI window (**Figure 4-2**). Users can click on one of the five modules to start corresponding functions of the program.

4.3.1 DICOM Import

As the first module of IClinfMRI, *DICOM Import* requires users to select a main directory, and all subdirectories containing DICOM files will be automatically recognized using MATLAB function "isdicom" and then renamed according to its embedded DICOM information. Concerning the difference in series naming across the center, three options for subdirectories naming are available in "Folder Rename Option" panel of the GUI, including (1) series description, (2) patient's ID and series description, (3) patient's ID, series description, and series number. Next, the DICOM files in various

directories are converted to NIfTI format. The converted NIfTI files are used for the following four modules.
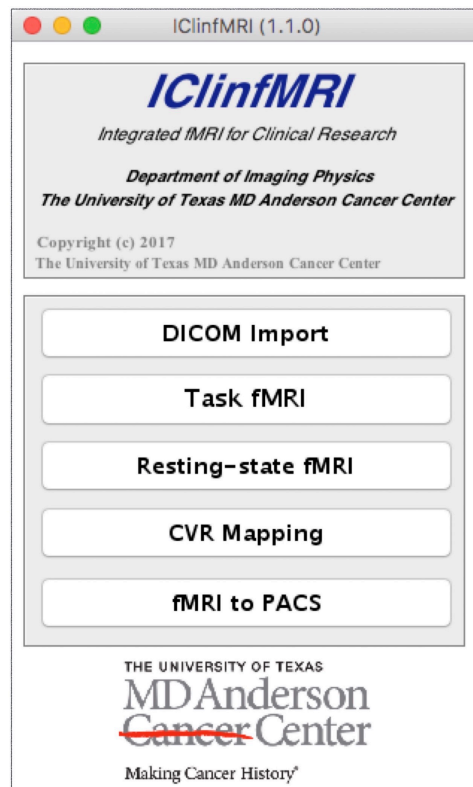
Figure 4-2 The main graphical user interface (GUI) of IClinfMRI
The main window comprises the five modules of the software.

4.3.2 Task fMRI

Since presurgical planning requires task-fMRI activations to be superimposed on an anatomical image, both task-fMRI and high-resolution T_1w images are requested in the *Task fMRI* module, using the "Task-fMRI" and "High-Res T1w" button (**Figure 4-3**). The "High-Res EPI" is optional. It allows users to select a high-quality echo-planar image volume, when available, to which the BBR algorithm can be applied to improve the registration with the T1w image. After users provide the onset timing and duration of a task in the unit of seconds, the timing of the paradigm will be updated, as shown in **Figure 4-3**. Once the required data and task paradigm are both set, the

74

"Processing" button will be enabled, and the "Preprocessing" section can be modified if the checkbox "Default" is unselected.
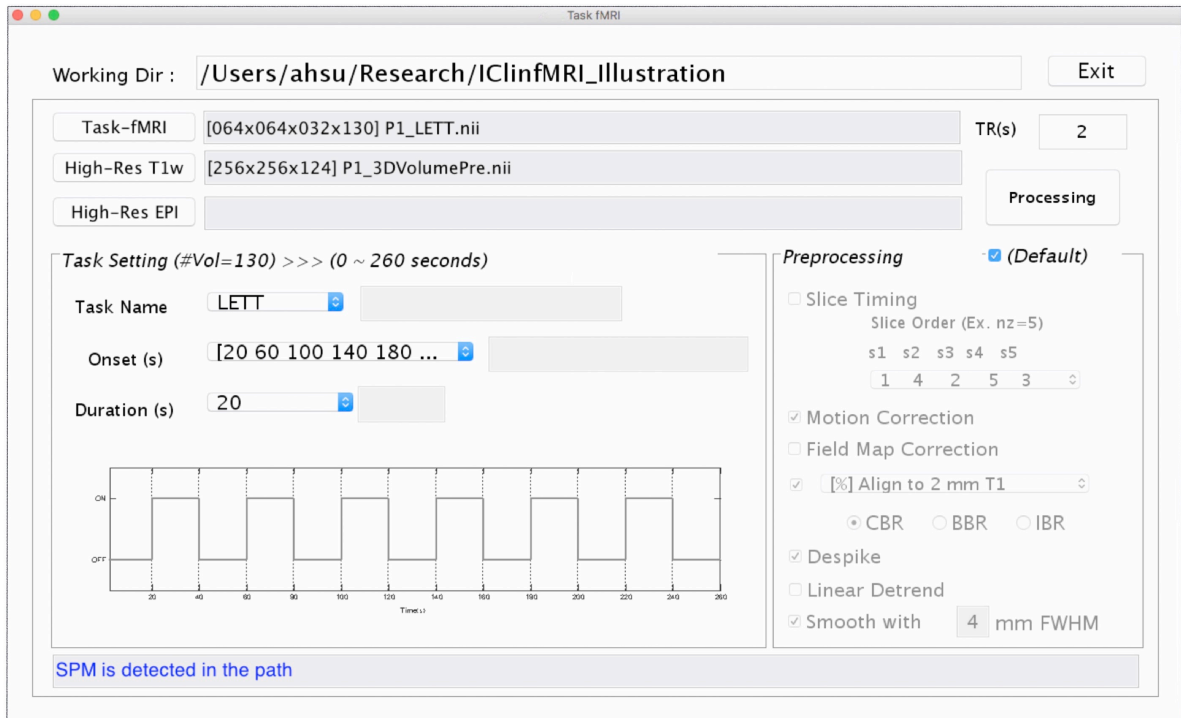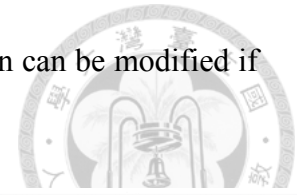
Figure 4-3 The GUI of Task fMRI module
This window consists of the imaging data input (upper), task paradigm setting (bottom left), and preprocessing setting (bottom right) panels.

After the "Processing" button is selected, the task-fMRI data will sequentially undergo the selected preprocessing steps, followed by the GLM-based activation detection. The resulting t statistical map is saved in a folder named by the task-fMRI data, which can be output for presurgical planning with the last module as well as retrieved in the *Resting-state fMRI* and *CVR Mapping* modules when needed.

4.3.3 Resting-State fMRI

Figure 4-4 demonstrates the user interface of the *Resting-state fMRI* module, with the processing for Patient #1. Both rs-fMRI data and high-resolution T_1w image are required, whereas the following three are optional inputs in this module.
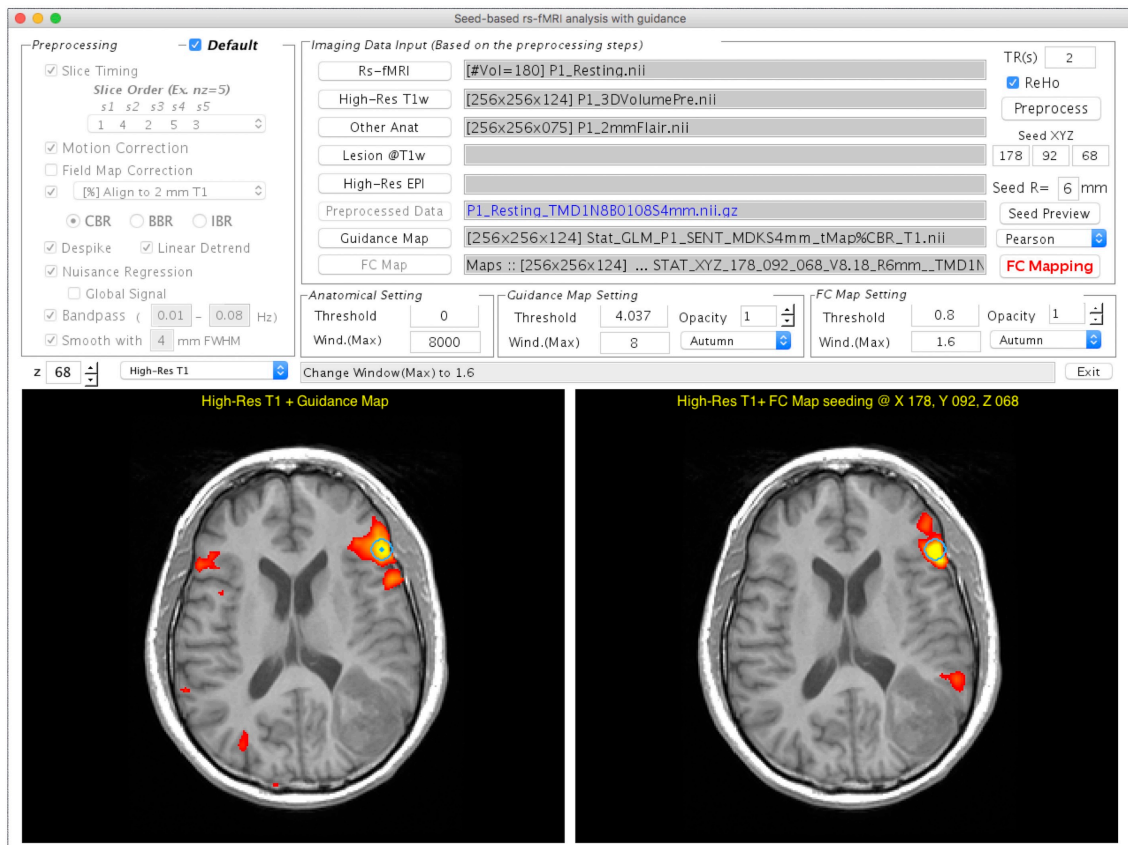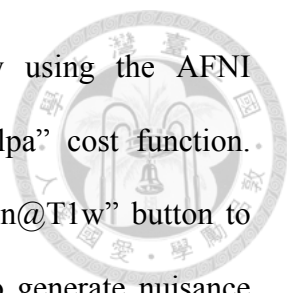
Figure 4-4 GUI of the *Resting-state fMRI* module displayed with processing and visualization for Patient #1

This window consists of the preprocessing selection (upper left), imaging data input panel (upper right), visualization widget (middle right), and two visualization panels (bottom left and right). The bottom left panel shows that the task-fMRI activation overlays ($t > 4.04$, $p < 10^{-4}$, uncorrected) on a high-resolution T_1w image. The bottom right panel shows the FC mapping result obtained with the seed determined based on the task-fMRI (turquoise circle).

First, the "Other Anat" button was designed to visualize the resulting rs-FC map on another structural image such as a T_2w FLAIR image. When an image is selected via

76

this button, the image will be aligned to the T_1w image by using the AFNI "align_epi_anat.py" function with the "-dset2to1" option and "-lpa" cost function. Second, the user can select a binary lesion mask using the "Lesion@T1w" button to exclude the lesion from the WM and CSF masks that are used to generate nuisance regressors in the FC calculation. Third, the utility of the "High-Res EPI" button resembles to *Task fMRI* module. After completing the data selection, one can click "Preprocess" for preprocessing the rs-fMRI data. The ReHo map of the preprocessed rs-fMRI data will be provided if the "ReHo" checkbox is selected. The guidance for seed selection is a unique function that we designed in this module. Users can select the "Guidance Map" button to superimpose the fMRI result, the ReHo results, or the RH+MA results on the displayed structural image for guiding the seed placement. After completing the data preprocessing, users can then define a seed by left-clicking the mouse on the bottom panels of the GUI, adjust the radius of seed sphere by using the edit box following the "R=" description, view the seed on the GUI by using "Seed Preview" button, and calculate the seed-based FC map by using "FC Mapping" button. In the demonstrated case (***Figure 4-4***), a seed (the turquoise dot with circular contour) was positioned on a local maximum (t=8.18, uncorrected $p<5\times10^{-13}$) of the sentence completion task-fMRI activation near the traditional Broca's area. The resulting rs-FC z-map is illustrated in the bottom right panel of the GUI, and the "FC Map Setting" is enabled for adjusting the threshold.

4.3.4 CVR Mapping

Figure 4-5 shows the *CVR Mapping* module, illustrated with the processing for Patient #1. Once the CVR data and T_1w images are selected, adjustments on the following four parameters become available: (1) the onset time of the BH period, (2) the

duration of each breath-hold, (3) multiple time delays applied to the GLM analysis, and
(4) response function used in the GLM analysis. Note that the flexibilities are given in
the onset and duration settings of each BH session, since in practice they usually vary
among patients/studies.
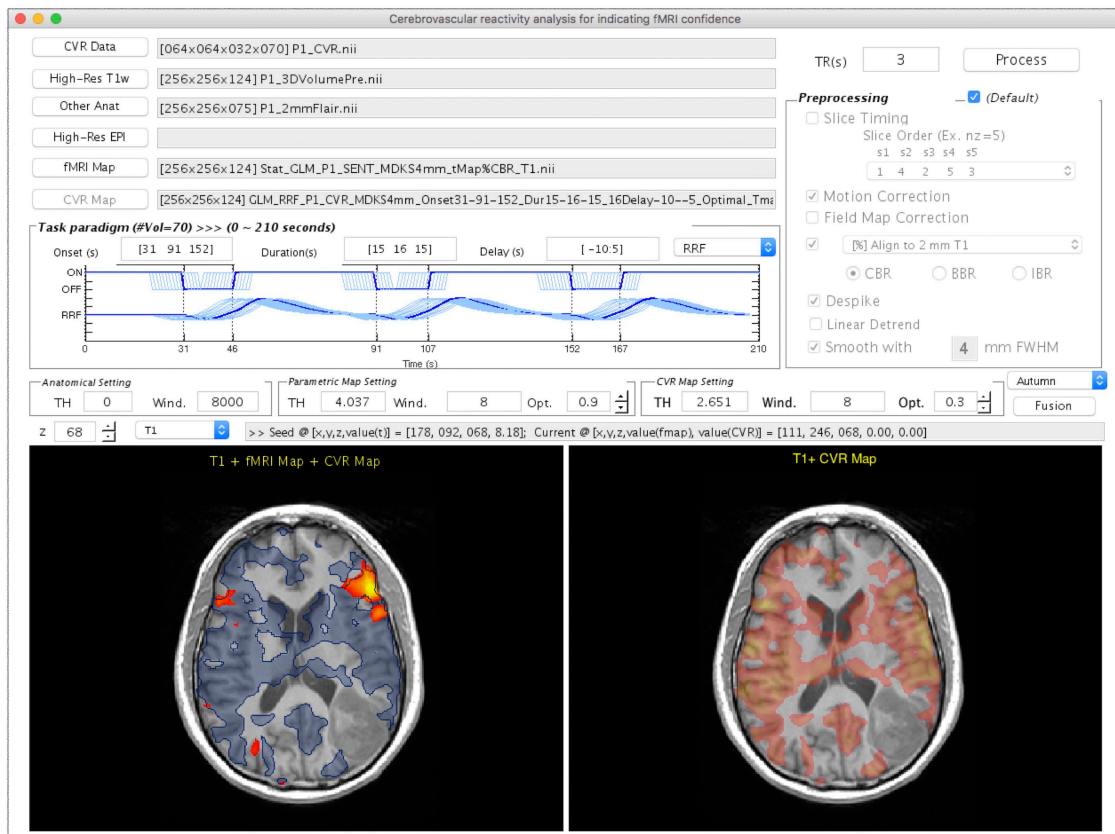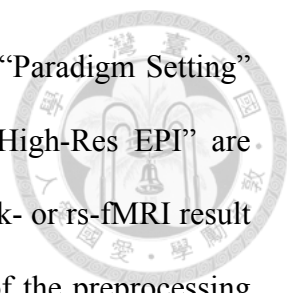
**Figure 4-5 The GUI of the CVR Mapping module displayed with processing and
visualization for Patient #1**

This window consists of the imaging data input panel (upper left), breath-hold paradigm
setting (middle left), preprocessing selection (upper right), visualization widget (middle),
and two visualization panels (bottom left and right). The bottom left panel shows the
task-fMRI activation overlays ($t > 4.04$, $p < 10^{-4}$, uncorrected) on a high-resolution T_1w
image using the warm color map. The result of CVR mapping ($t > 2.65$, $p < 0.01$,
uncorrected) displays as transparent blue with a solid blue contour. The area outside the
CVR map, but inside potential functional anatomy near the lesion, indicates the location
of possible NVU. The bottom right panel shows the CVR map using a warm color map.

As the parameters are adjusted, the diagram will be updated in the "Paradigm Setting" panel. Similar to the previous modules, the "Other Anat" and "High-Res EPI" are optional inputs. The "fMRI Map" button is used for selecting the task- or rs-fMRI result to be displayed in the bottom left panel (**Figure 4-5**). The option of the preprocessing step for CVR mapping is identical to that in the *Task-fMRI* module (**Figure 4-*3***). After the processing, the bottom right panel will automatically display the CVR map overlaying on the structural image (**Figure 4-5**). Finally, the "Fusion" button is enabled to fuse the resulting CVR map to the preselected fMRI results. Specifically, we display the thresholded CVR map as transparent blue with the solid blue line, together with fMRI activations (or networks) on the anatomical image. In this patient, markedly diminished ipsilateral CVR was seen in the areas within/near the tumor, which indicated NVU potentials and risk of false-negative results in fMRI.

4.3.5 fMRI to PACS

To convert an fMRI overlay on anatomical images to DICOM files, an anatomical image and parametric map are both required inputs. An option of saving an fMRI overlay on both T_1w and another anatomical image (e.g., T_2w FLAIR) in the same series was made available. DICOM headers of images in the resulting series adopted partially those in a DICOM image selected by the user, e.g., one of the original T_1w DICOM images. The output of this module included a series of DICOM images of white overlay and three series of color-coded overlays in three orthogonal orientations, respectively.

4.3.6 rs-fMRI Case Results and Validation

In these speech-fMRI results (***Figure 4-6A***), significant activations ($t > 4.04$, $p <$ 10^{-4}, uncorrected) were detected in bilateral frontal areas and right temporal/parietal area, but not in the left temporal/parietal area or in the traditional Wernicke's area.
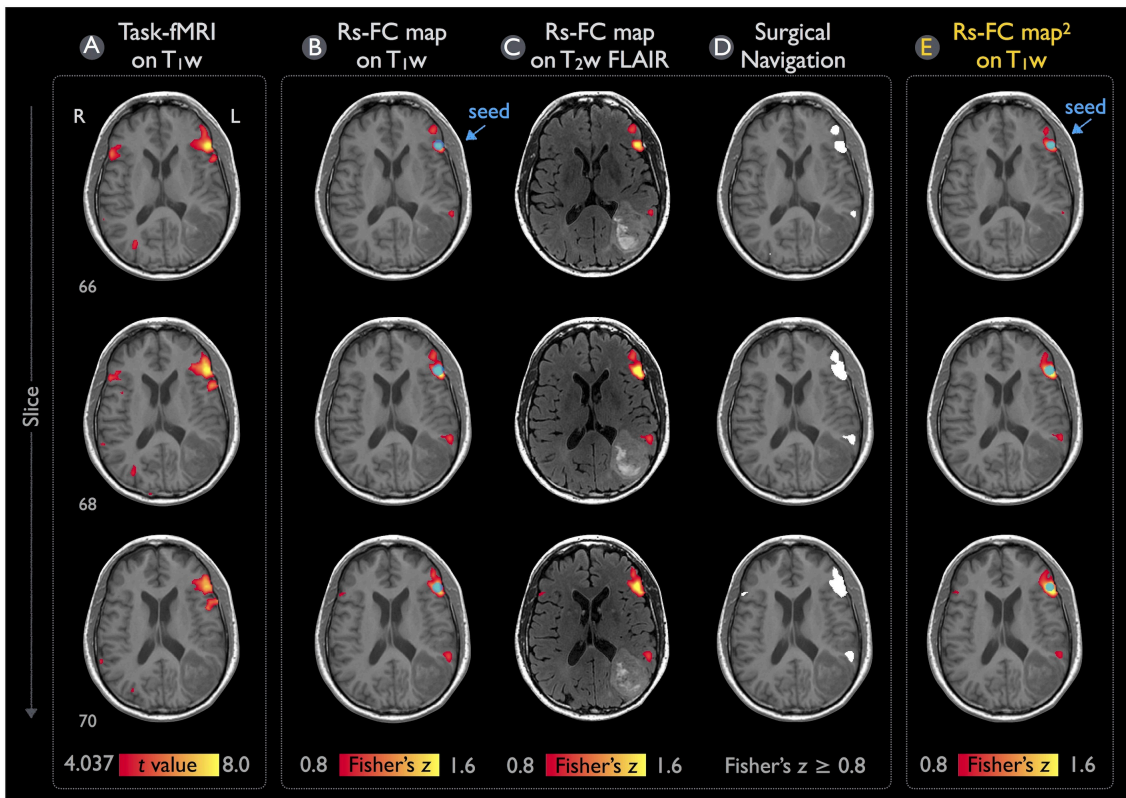
Figure 4-6 Language mapping resulting from task-fMRI and rs-fMRI for Patient #1

(A) The task-fMRI activation above the t statistic threshold of 4.04 ($p < 10^{-4}$, uncorrected) was overlaid on the T_1w image. **(B-C)** Seeding at the peak t value on the task-fMRI activation (blue circle), the rs-FC map above the Fisher's z threshold of 0.8 was overlaid on the T_1w and T_2w FLAIR images. **(D)** The thresholded rs-FC map overlaid on the T_1w image in the gray-scale DICOM format. **(E)** The rs-fMRI result analyzed independently from the IClinfMRI by using the procedure adopted in a previous study (Hart et al., 2016).

The rs-fMRI was helpful in that a clear language network between the left frontal and temporal/parietal areas was detected ($z \geq 0.8$), as demonstrated in ***Figure 4-6B-C*** (the same results but three kinds of overlay/underlay outputs from this module).
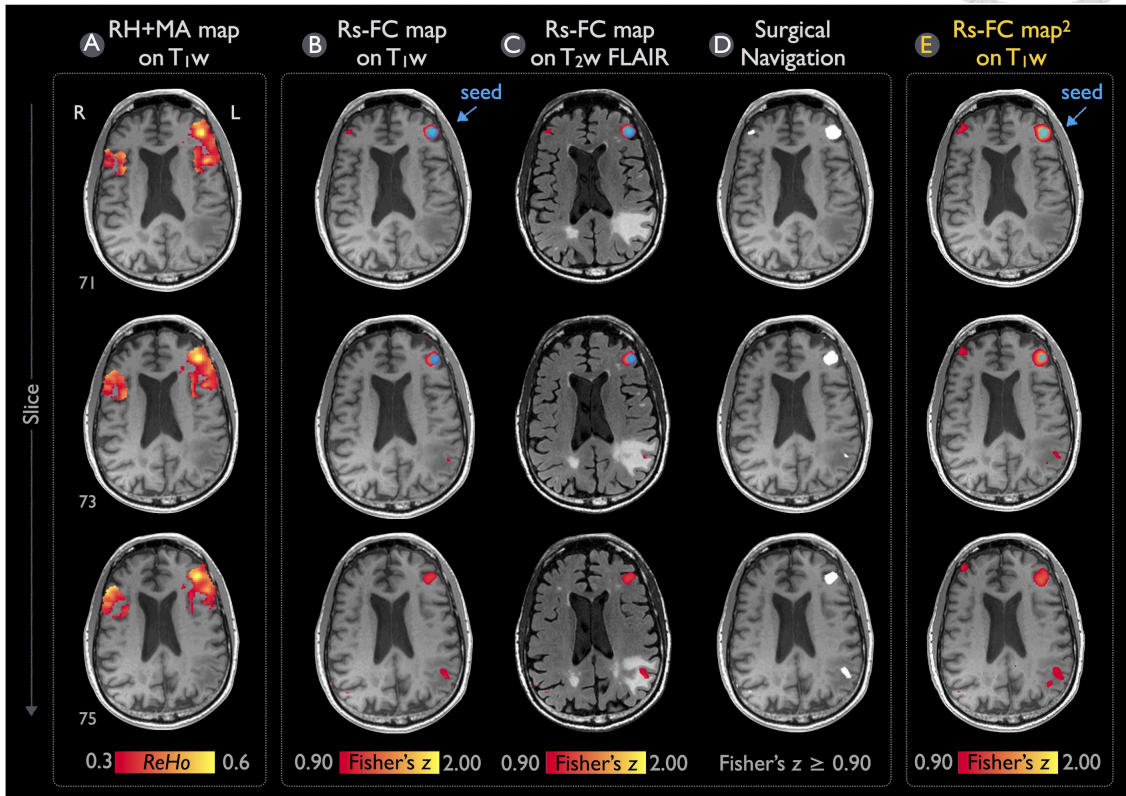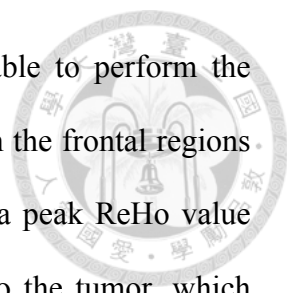
Figure 4-7 **Language mapping of rs-fMRI with seed guided by RH+MA map for Patient #2**

(A) The RH+MA map with a ReHo threshold of 0.3 is overlaid on the T_1w image. **(B-C)** Seeding at a local maximum of ReHo value (blue circle), the rs-FC map above the Fisher's z threshold of 0.9 is overlaid on the T_1w and T_2w FLAIR image. **(D)** The thresholded rs-FC map overlaid on the T_1w image in the gray-scale DICOM format. **(E)** The rs-fMRI result analyzed independently from the IClinfMRI by using the procedure adopted in the previous study (Hart et al., 2016).

Note that the gray-scale fused DICOM format (***Figure 4-6D***) can be directly imported by surgical navigation software. Moreover, the rs-fMRI result (***Figure 4-6B-D***) was consistent with that obtained by using the procedures described in the previous study and software independent from IClinfMRI (***Figure 4-6E***). ***Figure 4-7*** demonstrates the
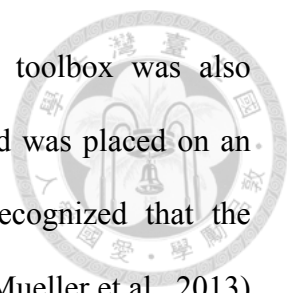
rs-fMRI language mapping results for Patient #2, who was not able to perform the speech fMRI tasks. The RH+MA map showed scattered hot spots in the frontal regions (***Figure 4-7A***). The seed placed in the putative Broca's area with a peak ReHo value was able to detect functional connectivity in brain regions close to the tumor, which were suspected to be in the posterior portion of the language network (***Figure 4-7B-D***). Similar to the results of Patient #1, the rs-fMRI connectivity pattern found by IClinfMRI was similar to that obtained by using previously published procedures (***Figure 4-7E***).
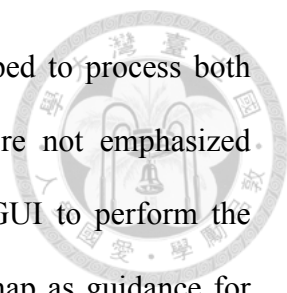
4.4 Discussion

Specialized software, IClinfMRI, was proposed in this study to integrate complementary fMRI techniques in clinical studies with applicability for presurgical planning. Clearly distinguishable from well-established fMRI software package, IClinfMRI was designed with user-friendly modules that can be easily fitted into the clinical workflow. These modules include importing/sorting DICOM images, exporting results that can be recognized by clinical PACS and surgical navigation system, and platforms that can analyze the three major clinical fMRI techniques, namely task-fMRI, rs-fMRI, and CVR mapping, independently yet in an integrated fashion. Unique functionalities of our software include the guidance of seed placement for the interactive rs-fMRI mapping and the visualization of CVR results for indicating potential NVU in fMRI activation maps. The IClinfMRI was specifically designed for translation to clinical fMRI practice with careful validation and is the focus of ongoing research for our team.

For the seed-based FC analysis of rs-fMRI data, previous studies predominantly used anatomical landmarks as guidance in placing a seed (Liu et al., 2009; Shimony et
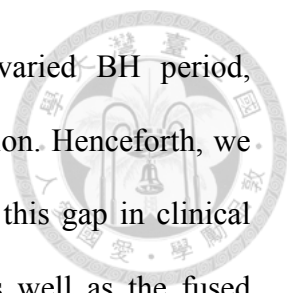
al., 2009; Zhang et al., 2009). The prototype of an interactive toolbox was also developed to calculate and visualize the rs-FC mapping after a seed was placed on an anatomical image (Böttger et al., 2011). However, it is well recognized that the functional localization of brain networks varies in healthy subjects (Mueller et al., 2013), and the variability can be even greater in patients with intracranial pathology (Mitchell et al., 2013). Alternatively, Rosazza et al. placed the seeds on the basis of task-fMRI activation and found that this approach was more sensitive in detecting sensorimotor networks in patients with lesions adjacent to functional areas than were seeds placed on the basis of anatomical landmarks (Rosazza et al., 2014). Cochereau et al. demonstrated 80% accuracy in detecting the rs-language network when seeding at functional sites determined by positive intraoperative DCS results (Cochereau et al., 2016). These studies suggested that determining seeds with guidance from independent functional localizations may improve the results of rs-fMRI analysis. Moreover, Yan et al. proposed a method to use ReHo for assisting seed localization in the rs-fMRI analysis, where the technical logic is described below. When defining a seed with a certain radius (or a volume) for rs-FC analysis, one averages time course across all voxels within this volume to form the reference time curve. Such averaging is based on the assumption that the time curves in those neighboring voxels are well synchronized. However, without examining the resting-state fMRI time curves, one would not know the spatial extent of the well-synchronized regions unless calculating the ReHo index. In other words, the seed selection is still primarily based on anatomical location, like most of the studies using seed-based analysis (Hart et al., 2016; Huang et al., 2016; Rosazza et al., 2014; Zhang et al., 2009), and the ReHo index is only used to refine the group of clusters within/around the assumed anatomical location

Recently, a software toolkit called *PreSurgMapp* was developed to process both task-fMRI and rs-fMRI, but seed guidance and visualization were not emphasized (Huang et al., 2016). In this work, we designed a double-panel GUI to perform the interactive rs-fMRI mapping while presenting another functional map as guidance for seed determination. Users can directly place a seed in either of the two windows, and it will be synchronously presented in the guidance map and rs-FC results for comparison. This interactive mapping facilitates exploration of the rs-functional network and makes it intuitive to users.
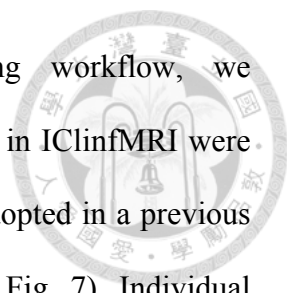
A limitation of our rs-fMRI module is that it supports only seed-based analysis rather than data-driven approaches. Seed-based analysis is more intuitive for users who have clear targets in functional networks that they intent to detect, such as motor and language, which is usually the situation in presurgical mapping. In addition, previous studies indicated the FC maps derived from the seed-based approach have higher consistency with task-fMRI results than do FC maps derived from an independent component analysis (Branco et al., 2016; Cochereau et al., 2016; Quigley et al., 2001; Sair et al., 2016). More recently, methods have been proposed to address the issue of component number optimization for the data-driven analysis (Lu et al., 2017). As the sensitivity and specificity of data-driven approaches improve, we will incorporate these approaches into the IClinfMRI workflow in the future.

A technical challenge of fMRI mapping in patients with neurological diseases is potential false-negative detection due to impaired neurovascular coupling in brain areas adjacent to or within the lesion. This challenge highlights the importance of CVR mapping to indicate brain regions with potential NVU, and subsequently to improve the confidence level of the task-fMRI. However, the existing clinical fMRI software packages, including those designed for presurgical mapping, do not support processing

doi:10.6342/NTU201802205

procedures specific to analysis of CVR mapping, such as a varied BH period, respiratory response function, and multiple delays in GLM calculation. Henceforth, we provided a *CVR Mapping* module with these functionalities to fill this gap in clinical needs. In terms of visualization, the double-panel GUI design, as well as the fused display, allows users to synchronously examine both fMRI and CVR mapping results precisely in their relative spatial positions. Thus the lack of fMRI activation in targeted functional locations but without significant CVR would be a warning of false-negative detection due to the NVU near or within the lesion.

Many research image processing toolboxes and fMRI processing software packages are able to deal with DICOM images. However, exporting the analysis results into clinical PACS and into a surgical navigation system requires not only outputting the results in DICOM format but also writing the DICOM header in a harmonized manner with other images of the same study. For example, original patient and study information should be kept, and a new series number and description should be generated. These aspects are well considered in all software provided by the MRI vendors and in other FDA-cleared software. Although previously developed research toolboxes for presurgical mapping provide the function to analyze fMRI data (Böttger et al., 2011; Huang et al., 2016), the lack of converting data in the DICOM format was the major obstacle for clinical practices. By giving the proper DICOM header, the *fMRI to PACS* module allows users to export a mapping result to the DICOM format by reattaching patients' information. It is important to note that this module can be used to export any images in NIfTI format and is not specifically constrained to the results analyzed by IClinfMRI, which makes it a general tool for wider applications such as quantitative imaging.

Concerning the validity of rs-fMRI functional mapping workflow, we demonstrated that the rs-FC maps processed with the procedure set in IClinfMRI were in accordance with the rs-FC maps processed with the procedure adopted in a previous study (Hart et al., 2016) using AFNI software alone (Fig. 6 and Fig. 7). Individual algorithms adopted in this module were identical to those used in previous validation studies that compared seed-based rs-fMRI with intraoperative mapping (Cochereau et al., 2016; Rosazza et al., 2014; Zhang et al., 2009). Minor differences of these rs-FC maps were expected because their preprocessing procedure and parameters were slightly different (see the *Methods and Implementation* section). For example, a smaller spatial extent in Figure 7B compared with that in Figure 7E was caused by the smaller smooth kernel applied in our procedure because spatial extent has been demonstrated to be directly associated with the spatial smoothing kernel on rs-FC maps (Wu et al., 2011).

Determining the threshold across individual mappings has been no consensus yet in the neuroimaging field because the various tasks result in different statistical sensitivity (Blatow et al., 2011; Nadkarni et al., 2015). Considering the fMRI mapping in clinical practice, the statistical threshold is determined by experienced clinicians who adjust a continuum of the threshold to obtain adequate activation extent without spurious clusters outside the eloquent cortex (Nadkarni et al., 2015; Rosazza et al., 2014). In contrast to such rater-dependent procedure, Lu et al. recently addressed an automatic procedure of threshold determination based on the training results (Lu et al., 2017). Nevertheless, no gold standard is reached for threshold determination at the current stage. Caution should be exercised when interpreting the statistical maps. In IClinfMRI, independent panels of threshold determination for both parametric and CVR maps were built for users to decide an appropriate threshold.

A limitation of IClinfMRI is that it calls functions in other free software including dcm2nii, AFNI, and SPM. Since AFNI is designed to run on Unix or Mac OS, those using a Windows operating system must install a virtual machine to run IClinfMRI.

In conclusion, by integrating fMRI techniques and implementing data conversion modules, our toolbox is a strong research tool that has been designed for translation to clinical practice. Two approaches in producing guidance maps—task-fMRI activation and the RH+MA map—were implemented for seed-based rs-fMRI mapping. By assisting in interpreting the clinical fMRI study, CVR mapping is able to provide visualization for indicating the potential false-negative areas in fMRI results. Any mapping result in the NIfTI format generated by either IClinfMRI or other research software can be exported in a DICOM format that is ready to be incorporated into PACS. IClinfMRI has been developed to incorporate advanced fMRI methods with streamlined processing and has shortened the processing time for presurgical mapping and other clinical applications. The software is freely available and can be requested by contacting the authors of this article.

Chapter 5

Conclusion, Discussion, and Future Works

5.1 Conclusion
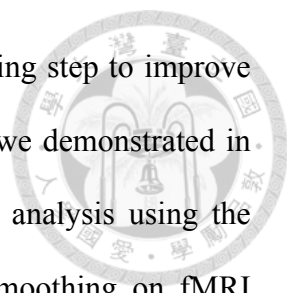
Resting-state fMRI has been continuously growing in the field of neuroimaging and clinical practice for its ability to map brain networks noninvasively with high compliance from subjects. This is especially relevant in clinical settings, especially in presurgical counseling and planning, where a number of patients cannot comply with task demands. However, this rs-fMRI technique still faces several methodological challenges for further clinical application. In this dissertation, we first addressed the lack of measure on rs-fMRI data quality to obtain reliable FC outcomes, and proposed a practical quality-assurance indicator—PICSO—for rs-fMRI data sets. Targeting on presurgical mapping, we introduced a guiding strategy that assisted the clinician in seed selection for the language mapping using rs-fMRI. In aim 3, we developed IClinfMRI software to profit further clinical studies based upon advance fMRI techniques. In brief, we successfully translated fMRI techniques into presurgical mapping on the basis of rs-fMRI technique developments. The presented studies, we believe, not only facilitate the application of fMRI techniques on general clinical practices, but also improve the brain-mapping precision in future personalized medicine.

5.2 Discussion
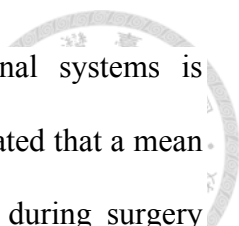
As an improvement of hardware and sequence design, the spatial resolution can be increased without compromising whole brain coverage. However, in fMRI, achievable voxel size is not the main factor to determine the spatial resolution. However, the hardware limitation on voxel size is not the main factor to determine the spatial resolution in fMRI. Following the a weighted average of synchronized neural population within an area of 0.5-3 mm^2 (i.e. local field potential), the fMRI signal driven by blood flow and volume changes (Logothetis et al., 2001). In response to a point-like neuronal activity, the spatial specificity of the point-spread fMRI signal has been reported as 3.5 mm and 2.34 mm of visual cortex for 1.5T and 7T, respectively (Engel, 1997; Shmuel et al., 2007), demonstrating the spatial limitation of fMRI signal on the basis of vasculature. Considering the spatial relationships between neurophysiology and underlying vasculature, the differentiable spatial resolution in fMRI would be constrained around 3 mm at 3T, even if we push the hardware limit of voxel size smaller than $0.5 \times 0.5 \times 0.5 mm^3$.

In chapter 2, we proposed the PICSO index to assess the ratio of physiological fluctuation to thermal noise. Based on the tight coupling between fMRI signal and neural activity, an increase of the neural synchronisation leads to an enhancement of physiological fluctuation, resulting in an increase of PICSO value and local connectivity of the neighboring voxels. Since the PICSO is a local estimate, the remote connectivity measured by the temporal correlation between regions has no directly relationship with PICSO. Caution should be exercised when interpreting the relation between PICSO maps and remote connectivity.

89

In fMRI analysis, spatial smoothing is an important preprocessing step to improve the signal-to-noise ratio (SNR) and PICSO of the fMRI dataset as we demonstrated in Chaper2. In addition, it is a prerequisite for the further statistical analysis using the general linear model (Lindquist, 2008). The degrees of spatial smoothing on fMRI dataset have demonstrated a significant impact on task-fMRI mapping (Lu et al., 2012) and rs-fMRI mapping (Hsu et al., 2016; Wu et al., 2011). While the spatial smoothing improves SNR, it sacrifices the spatial resolution of the functional maps. The reduction in spatial resolution may be an undesirable cost for clinical evaluation, especially for surgical planning. Generally, smoothing kernel size for presurgical fMRI mapping vary between 0–8 mm FWHM (Huang et al., 2016; Kokkonen et al., 2009; Kristo et al., 2014; Liu et al., 2009; Lu et al., 2012). Considering the benefit and cost of spatial smoothing, the smoothness of 4-mm FWHM is set as the default in IClinfMRI based on our experiences. Furthermore, users are able to adjust their preferred smoothness level in the software.
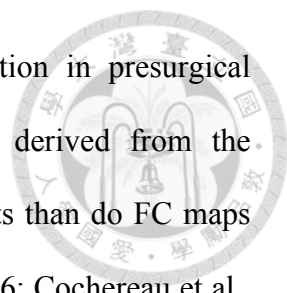
In addition to spatial smoothing, inclusion/exclusion of global signal remains a controversial issue for rs-fMRI preprocessing. Previous studies of presurgical fMRI mapping have applied global signal as a nuisance regressor to reduce the spurious variance from non-neural sources and to improve the spatial specificity of the resulting functional networks, such as motor (Rosazza et al., 2014) and language network (Lee et al., 2016; Mitchell et al., 2013). However, this nuisance regression has been criticized for introducing the artificial anti-correlations in seed-based correlation analysis (Fox et al., 2009; Murphy et al., 2009). In the *Resting-state fMRI* module of IClinfMRI, regressing out global signal was built in as an optional preprocessing step upon users' decision.

90

It is important to note the issue that accuracy of navigational systems is compromised by the opened cranium. Reinges and colleagues demonstrated that a mean displacement of the cortical landmarks ranged from 0.8 to 14.3 mm during surgery (Reinges et al., 2004), degrading the reliability of the alignment between the preoperative imaging and the intraoperative brain position. In this case, several approaches have been proposed to preserve the accurate alignment between the preoperative and intraoperative brain position. For example, using intraoperative ultrasound to detect the brain shift and to update the preoperative imaging data (Rasmussen et al., 2007). In addition, a significantly improvement in alignment accuracy has been reported in 1.82 mm with the use of non-rigid registration(Archip et al., 2007). Although our developed software has yet incorporated the feature of updating mapping result on navigation system due to the brain shift during surgery, our software provides the function of intraoperative fMRI mapping which does not suffer from the issue of inaccurate alignment

The design of the study in Chapter3 hinged around task-fMRI as a reference technique, with respect to which the Dice coefficient of rs-fMRI were measured. Although we observed a moderate overlay between rs-fMRI and task-fMRI, the functional localizations derived from fMRI do not directly indicate its essential role in language processing and represent a risk of future deficits in case of brain tissue removal due to the lack of gold-standard reference of activity localization. In the near future, we still need the intraoperative DCS data to support our findings.

A limitation of the resting-state module implemented in Chapter 4 is that it supports only seed-based analysis rather than data-driven approaches. Seed-based analysis is more intuitive for users who have clear targets in functional networks that they intent to

detect, such as motor and language, which is usually the situation in presurgical mapping. In addition, previous studies indicated the FC maps derived from the seed-based approach have higher consistency with task-fMRI results than do FC maps derived from an independent component analysis (Branco et al., 2016; Cochereau et al., 2016; Quigley et al., 2001; Sair et al., 2016). More recently, methods have been proposed to address the issue of component number optimization for the data-driven analysis (Lu et al., 2017). As the sensitivity and specificity of data-driven approaches improve, we will incorporate these approaches into the IClinfMRI workflow in the future.

5.3 Future Work

Rs-fMRI has been widely used to map functional connectivity throughout the brain using fMRI scanning while subjects lie "at rest" in the MRI machine (Huettel et al., 2009; Lee et al., 2013). To achieve a successful connectivity mapping using the rs-fMRI signal, the key is to guarantee sufficient physiological fluctuations over the thermal/system noise, which we already stated this point of view in Chapter 2 (PICSO). To date, the technical developments of accelerated sampling methods, such as parallel imaging and multiband technique, are speculated to benefit on the enhancement of neurophysiological fluctuations in rs-fMRI time series by reducing the interferences of physiological noise such as heartbeat or respiration (Uğurbil et al., 2013). For example, the recently introduced multiband EPI technique effectively shortens the acquisition time by enabling simultaneous acquisitions of multiple slices (Feinberg and Setsompop, 2013). To test on this hypothesis, we acquired a preliminary dataset for evaluation. Assuming that the noise of accelerated images $\left(\sigma_{Accelerated\ factor > 1}\right)$ over time is

independent from the non-accelerated images $\left(\sigma_{Accelerated\ factor=0}\right)$, the variance of measured noise after temporal subtraction could be regarded as the sum of noise variance of non-accelerated images and that of accelerated images $\left(\sigma_{Measured}^{2} = \sigma_{Accelerated\ factor=0}^{2} + \sigma_{Accelerated\ factor>1}^{2}\right)$.
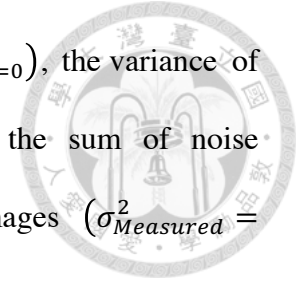
Supplementing the proposed PICSO index in Chapter 2 on the new acquisition technique, indices of $\sigma_{Non-accelerated\ images}$, $\sigma_{Accelerated\ images}$, and PICSO were first evaluated with increased multiband factor and parallel imaging factor (GRAPPA), where the PICSO of accelerated images was estimated based on the ratio of total fluctuation to the measured noise using temporal subtraction and correction factor (Hsu et al., 2016). On the basis of standard EPI protocol, we acquired rs-fMRI data with up to 4-fold GRAPPA acceleration (GRAPPA factor, G = 0, 2, 4) on two healthy subjects and 4-fold slice acceleration (multiband factor, M = 0, 2, 4) on four healthy subjects. The detailed acquisition parameter was presented in **Table 5-1**Table 5-1.

Table 5-1 Acquisition parameters for rs-fMRI non-accelerated and accelerated EPI time-series

Protocol	Matrix size	Voxel size	TR (ms)	TE (ms)	FA(°)	Measurement	BW
Regular EPI (G0)	64×64×33	3.44×3.44×3.0	2000	30	60	160	2367 Hz/px
EPI with G=2	64×64×33	3.44×3.44×3.4	2000	30	60	160	2367 Hz/px
EPI with G=4	64×64×33	3.44×3.44×3.4	2000	30	60	160	2367 Hz/px
EPI with M=0	64×64×12	3.44×3.44×3.4	785	30	60	420	2367 Hz/px
EPI with M=2	64×64×24	3.44×3.44×3.4	785	30	60	420	2367 Hz/px
EPI with M=4	64×64×48	3.44×3.44×3.4	785	30	60	420	2367 Hz/px

After the preprocessing steps (motion correction, normalization, despikeing and 3rd-order detrending), the measured noise and PICSO were estimated in a voxel-wise manner and averaged in a region of posterior cingulate cortex (PCC), as shown in **Table 5-2**. With increasing M-factor, the mean measured noise in PCC increased from 1.84 to 2.03 and the corresponding PICSO decreased from 1.43 to 1.16. As the GRAPPA factor increased, the mean measured noise in PCC increased from 2.58 to 4.16, and the
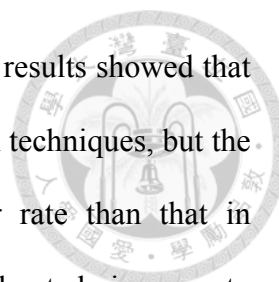
corresponding PICSO decreased from 1.01 to 0.64. Our preliminary results showed that an increase of measured noise was demonstrated in both acceleration techniques, but the measured noise in GRAPPA acceleration increased with a higher rate than that in multiband acceleration. In addition, the noise ratio of accelerated images to non-accelerated images $(\sigma_{M>1}/\sigma_{M=0})$ was increased from 0.14 to 0.35 for multiband factor of 2 to 4, respectively. Similar to the multiband technique, the noise ratio of rs-fMRI images with GRAPPA to that without GRAPPA technique $(\sigma_{G>1}/\sigma_{G=0})$ was increased from 0.58 to 1.27 as the GRAPPA factor from 2 to 4. Notably, caution should be exercised on these observations because the preliminary results were based on the presumption that the temporal fluctuations are independent of the spatial modulations by acceleration methods. Once the spatial modulation alters the temporal distributions of acquired rs-fMRI data, the $\sigma_{Accelerated\ images}$ should be re-evaluated in consideration of the spatio-temporal dependency. Although the evaluation was preliminarily presented, current observations suggested that M2 is a better choice to future fMRI studies for its highest sensitivity (PICSO) and lowest measured noise among tested acceleration sequences except M0.

Table 5-2 Average values of measured noise and PICSO for both non-accelerated and accelerated rs-fMRI data
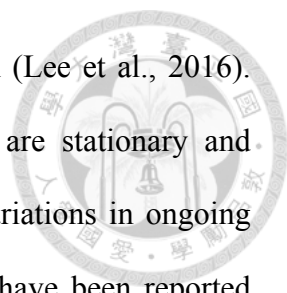
Case	$\sigma_{Measured}$						PICSO						σ_M		σ_G		$\sigma_{M>1}/\sigma_{M=0}$		$\sigma_{G>1}/\sigma_{G=0}$	
	M0	M2	M4	G0	G2	G4	M0	M2	M4	G0	G2	G4	M2	M4	G2	G4	M2	M4	G2	G4
1	2.05	2.03	2.17	—	—	—	1.12	1.08	0.99	—	—	—	—	0.71	—	—	—	0.34	—	—
2	1.61	1.63	—	—	—	—	1.34	1.31	—	—	—	—	0.22	—	—	—	0.14	—	—	—
3	1.81	1.77	1.88	—	—	—	2.01	1.50	1.42	—	—	—	—	0.52	—	—	—	0.29	—	—
4	1.88	1.87	2.04	2.64	3.23	4.16	1.25	1.27	1.08	0.93	0.90	0.68	—	0.80	1.87	3.22	—	0.43	0.71	1.22
5	—	—	—	2.52	2.76	4.17	—	—	—	1.08	0.94	0.61	—	—	1.13	3.32	—	—	0.45	1.32
Average	1.84	1.82	2.03	2.58	3.00	4.16	1.43	1.29	1.16	1.01	0.92	0.64	0.22	0.67	1.50	3.27	0.14	0.35	0.58	1.27

Abbreviations M, Multiband; G, GRAPPA; $\sigma_{Measured}$, Measured noise of acquired images; PICSO, Physiological Contribution in Spontaneous Oscillations

σ_M, Noise of the accelerated images with M>1; σ_G, Noise of the accelerated images with G>1

Note $\sigma_{Measured}^2 = (\sigma_{M=0}^2 + \sigma_{M>1}^2)$; $\sigma_{Measured}^2 = (\sigma_{G=0}^2 + \sigma_{G>1}^2)$

Accurate mapping of eloquent cortex in the brain expands surgical treatment options for patients and reduces the risk of postsurgical deficits (Gil-Robles and Duffau, 2010). Rs-fMRI mapping has played an important role in the presurgical assessment of

patients who are unable to cooperate with the task-based paradigm (Lee et al., 2016). Classical rs-fMRI methods assume the functional networks that are stationary and maintain the same structure over the data acquisition; however, variations in ongoing acquisition such as the dynamic changes in network connectivity have been reported compromised the detection of functional network in single subjects (Chang and Glover, 2010; Power et al., 2015). Additionally, the non-neural noise occurred transiently during the acquisition limits mapping sensitivity and affect its clinical use (Lin et al., 2016), obscuring networks as well as creating false-positive connections. Methodologies have been proposed to enhance the task-fMRI sensitivity, such as increasing the number of data points, or adopting complex designs, or using delicate processing procedures, yet previous two are not practical for clinical cases. Instead of prolonging fMRI experimental time, applying analytical strategies is favorable to enhance the sensitivity with the use of noise reduction. The independent component analysis has been used to address nonstationary decomposition for mapping intrinsic network and removing fMRI noise (Beall and Lowe, 2007; Kochiyama et al., 2005; Perlbarg et al., 2007; Thomas et al., 2002); however, the typical spatial ICA faces the challenges of determining the proper number of components and selecting components of interest (Hui et al., 2011). Recently, the ensemble empirical mode decomposition (EEMD) method (Huang et al., 1998) has been introduced as an adaptive filter on task-fMRI signals to increased sensitivity for mapping task activation (Lin et al., 2016). Without the constraints of stationarity and linearity on the fMRI signal, the EEMD adaptively decomposes the input signal into a set of intrinsic mode functions and then to filter task-irrelevant noise from raw data. However, the EEMD-based denoising approach has yet been adopted to denoise the rs-fMRI data in clinical application on individual patients. In the near future, we plan to use the EEMD-based denoising approach as a patient-specific rs-fMRI noise

removal routine and anticipate to augment the mapping sensitivity by using the Hilbert–Huang-based analysis for purifying the time-invariant features of the target networks without imposing assumption to the stationarity and linearity of the rs-fMRI signal. We hypothesized that EEMD is more effective than ICA methods at noise removal in localizing rs-fMRI functional network. We will validate the rs-fMRI results by using the task-fMRI and intraoperative DCS as standards.

96

Reference
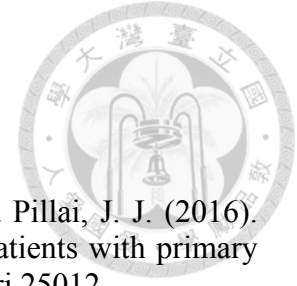
Agarwal, S., Sair, H. I., Yahyavi-Firouz-Abadi, N., Airan, R., and Pillai, J. J. (2016). Neurovascular uncoupling in resting state fMRI demonstrated in patients with primary brain gliomas. *J Magn Reson Imaging* 43, 620–626. doi:10.1002/jmri.25012.

Archip, N., Clatz, O., Whalen, S., Kacher, D., Fedorov, A., Kot, A., et al. (2007). Non-rigid alignment of pre-operative MRI, fMRI, and DT-MRI with intra-operative MRI for enhanced visualization and navigation in image-guided neurosurgery. *Neuroimage* 35, 609–624. doi:10.1016/j.neuroimage.2006.11.060.

Ashburner, J., and Friston, K. J. (2005). Unified segmentation. *Neuroimage* 26, 839–851. doi:10.1016/j.neuroimage.2005.02.018.

Bandettini, P. (2007). Functional MRI today. *Int J Psychophysiol* 63, 138–145. doi:10.1016/j.ijpsycho.2006.03.016.

Bandettini, P. A. (2012). Twenty years of functional MRI: the science and the stories. *Neuroimage* 62, 575–588. doi:10.1016/j.neuroimage.2012.04.026.

Barch, D. M., Sheline, Y. I., Csernansky, J. G., and Snyder, A. Z. (2003). Working memory and prefrontal cortex dysfunction: specificity to schizophrenia compared with major depression. *Biol. Psychiatry* 53, 376–384.

Bates, E., Wilson, S. M., Saygin, A. P., Dick, F., Sereno, M. I., Knight, R. T., et al. (2003). Voxel-based lesion-symptom mapping. *Nat. Neurosci.* 6, 448–450. doi:10.1038/nn1050.

Beall, E. B., and Lowe, M. J. (2007). Isolating physiologic noise sources with independently determined spatial measures. *Neuroimage* 37, 1286–1300. doi:10.1016/j.neuroimage.2007.07.004.

Becker, T. M., Kerns, J. G., Macdonald, A. W., and Carter, C. S. (2008). Prefrontal dysfunction in first-degree relatives of schizophrenia patients during a Stroop task. *Neuropsychopharmacology* 33, 2619–2625. doi:10.1038/sj.npp.1301673.

Benjamin, C. F., Walshaw, P. D., Hale, K., Gaillard, W. D., Baxter, L. C., Berl, M. M., et al. (2017). Presurgical language fMRI: Mapping of six critical regions. *Hum Brain Mapp* 38, 4239–4255. doi:10.1002/hbm.23661.

Bianciardi, M., Fukunaga, M., van Gelderen, P., Horovitz, S. G., de Zwart, J. A., Shmueli, K., et al. (2009). Sources of functional magnetic resonance imaging signal fluctuations in the human brain at rest: a 7 T study. *Magn Reson Imaging* 27, 1019–1029. doi:10.1016/j.mri.2009.02.004.

Birn, R. M., Smith, M. A., Jones, T. B., and Bandettini, P. A. (2008). The respiration response function: the temporal dynamics of fMRI signal fluctuations related to changes in respiration. *Neuroimage* 40, 644–654. doi:10.1016/j.neuroimage.2007.11.059.

Biswal, B., Yetkin, F. Z., Haughton, V. M., and Hyde, J. S. (1995). Functional connectivity in the motor cortex of resting human brain using echo-planar MRI. *Magn Reson Med* 34, 537–541.

Bizzi, A., Blasi, V., Falini, A., Ferroli, P., Cadioli, M., Danesi, U., et al. (2008). Presurgical functional MR imaging of language and motor functions: validation with intraoperative electrocortical mapping. *Radiology* 248, 579–589. doi:10.1148/radiol.2482071214.

Black, D. F., Vachha, B., Mian, A., Faro, S. H., Maheshwari, M., Sair, H. I., et al. (2017). American Society of Functional Neuroradiology–Recommended fMRI Paradigm Algorithms for Presurgical Language Assessment. *AJNR Am J Neuroradiol* 38, E65–E73. doi:10.5306/wjco.v2.i7.289.

Blatow, M., Reinhardt, J., Riffel, K., Nennig, E., Wengenroth, M., and Stippich, C. (2011). Clinical functional MRI of sensorimotor cortex using passive motor and sensory stimulation at 3 Tesla. *J Magn Reson Imaging* 34, 429–437. doi:10.1002/jmri.22629.

Bodurka, J., Ye, F., Petridou, N., Murphy, K., and Bandettini, P. A. (2007). Mapping the MRI voxel volume in which thermal noise matches physiological noise--implications for fMRI. *Neuroimage* 34, 542–549. doi:10.1016/j.neuroimage.2006.09.039.

Bookheimer, S. (2007). Pre-surgical language mapping with functional magnetic resonance imaging. *Neuropsychol Rev* 17, 145–155. doi:10.1007/s11065-007-9026-x.

Boveroux, P., Vanhaudenhuyse, A., Bruno, M.-A., Noirhomme, Q., Lauwick, S., Luxen, A., et al. (2010). Breakdown of within- and between-network resting state functional magnetic resonance imaging connectivity during propofol-induced loss of consciousness. *Anesthesiology* 113, 1038–1053. doi:10.1097/ALN.0b013e3181f697f5.

Böttger, J., Margulies, D. S., Horn, P., Thomale, U. W., Podlipsky, I., Shapira-Lichter, I., et al. (2011). A software tool for interactive exploration of intrinsic functional connectivity opens new perspectives for brain surgery. *Acta Neurochir* 153, 1561–1572. doi:10.1007/s00701-011-0985-6.

Branco, P., Seixas, D., Deprez, S., Kovacs, S., Peeters, R., Castro, S. L., et al. (2016). Resting-State Functional Magnetic Resonance Imaging for Language Preoperative Planning. *Front Hum Neurosci* 10, 11. doi:10.3389/fnhum.2016.00011.

Chang, C., and Glover, G. H. (2010). Time-frequency dynamics of resting-state brain connectivity measured with fMRI. *Neuroimage* 50, 81–98. doi:10.1016/j.neuroimage.2009.12.011.

Chang, C., Cunningham, J. P., and Glover, G. H. (2009a). Influence of heart rate on the BOLD signal: the cardiac response function. *Neuroimage* 44, 857–869. doi:10.1016/j.neuroimage.2008.09.029.

Chang, T.-Y., Kuan, W.-C., Huang, K.-L., Chang, C.-H., Chang, Y.-J., Wong, H.-F., et al. (2013). Heterogeneous cerebral vasoreactivity dynamics in patients with carotid stenosis. *PLoS ONE* 8, e76072. doi:10.1371/journal.pone.0076072.

Chang, T.-Y., Liu, H.-L., Lee, T.-H., Kuan, W.-C., Chang, C.-H., Wu, H.-C., et al. (2009b). Change in cerebral perfusion after carotid angioplasty with stenting is related to cerebral vasoreactivity: a study using dynamic susceptibility-weighted contrast-enhanced MR imaging and functional MR imaging with a breath-holding paradigm. *AJNR Am J Neuroradiol* 30, 1330–1336. doi:10.3174/ajnr.A1589.

Chen, L. M., Yang, P.-F., Wang, F., Mishra, A., Shi, Z., Wu, R., et al. (2017). Biophysical and neural basis of resting state functional connectivity: Evidence from non-human primates. *Magn Reson Imaging* 39, 71–81. doi:10.1016/j.mri.2017.01.020.

Chu, C., Hsu, A.-L., Chou, K.-H., Bandettini, P., Lin, C., Alzheimer's Disease Neuroimaging Initiative (2012). Does feature selection improve classification accuracy? Impact of sample size and feature selection on classification using anatomical magnetic resonance images. *Neuroimage* 60, 59–70. doi:10.1016/j.neuroimage.2011.11.066.

Cochereau, J., Deverdun, J., Herbet, G., Charroud, C., Boyer, A., Moritz-Gasser, S., et al. (2016). Comparison between resting state fMRI networks and responsive cortical stimulations in glioma patients. *Hum Brain Mapp* 37, 3721–3732. doi:10.1002/hbm.23270.

Cox, R. W. (1996). AFNI: software for analysis and visualization of functional magnetic resonance neuroimages. *Comput. Biomed. Res.* 29, 162–173.

Devonshire, I. M., Papadakis, N. G., Port, M., Berwick, J., Kennerley, A. J., Mayhew, J. E. W., et al. (2012). Neurovascular coupling is brain region-dependent. *Neuroimage* 59, 1997–2006. doi:10.1016/j.neuroimage.2011.09.050.

Dietrich, O., Raya, J. G., Reeder, S. B., Reiser, M. F., and Schoenberg, S. O. (2007). Measurement of signal-to-noise ratios in MR images: influence of multichannel coils, parallel imaging, and reconstruction filters. *J Magn Reson Imaging* 26, 375–385. doi:10.1002/jmri.20969.

Dimou, S., Battisti, R. A., Hermens, D. F., and Lagopoulos, J. (2013). A systematic review of functional magnetic resonance imaging and diffusion tensor imaging modalities used in presurgical planning of brain tumour resection. *Neurosurg Rev* 36, 205–14– discussion 214. doi:10.1007/s10143-012-0436-8.

Dong, Y., Winstein, C. J., Albistegui-DuBois, R., and Dobkin, B. H. (2007). Evolution of FMRI activation in the perilesional primary motor cortex and cerebellum with rehabilitation training-related motor gains after stroke: a pilot study. *Neurorehabil Neural Repair* 21, 412–428. doi:10.1177/1545968306298598.

Engel, S. (1997). Retinotopic organization in human visual cortex and the spatial precision of functional MRI. *Cerebral Cortex* 7, 181–192. doi:10.1093/cercor/7.2.181.

Fedorenko, E., Hsieh, P.-J., Nieto-Castañón, A., Whitfield-Gabrieli, S., and Kanwisher, N. (2010). New Method for fMRI Investigations of Language: Defining ROIs Functionally in Individual Subjects. *J. Neurophysiol.* 104, 1177–1194. doi:10.1002/(SICI)1097-0193(1997)5:4<218::AID-HBM2>3.0.CO;2-6.

Feinberg, D. A., and Setsompop, K. (2013). Ultra-fast MRI of the human brain with simultaneous multi-slice imaging. *J. Magn. Reson.* 229, 90–100. doi:10.1016/j.jmr.2013.02.002.

Fox, M. D., Zhang, D., Snyder, A. Z., and Raichle, M. E. (2009). The global signal and observed anticorrelated resting state brain networks. *J. Neurophysiol.* 101, 3270–3283. doi:10.1152/jn.90777.2008.

Fukunaga, M., Horovitz, S. G., van Gelderen, P., de Zwart, J. A., Jansma, J. M., Ikonomidou, V. N., et al. (2006). Large-amplitude, spatially correlated fluctuations in BOLD fMRI signals during extended rest and early sleep stages. *Magn Reson Imaging* 24, 979–992. doi:10.1016/j.mri.2006.04.018.

Genetti, M., Grouiller, F., Vulliemoz, S., Spinelli, L., Seeck, M., Michel, C. M., et al. (2013). Noninvasive language mapping in patients with epilepsy or brain tumors. *Neurosurgery* 72, 555–65– discussion 565. doi:10.1227/NEU.0b013e318282cdad.

Gil-Robles, S., and Duffau, H. (2010). Surgical management of World Health Organization Grade II gliomas in eloquent areas: the necessity of preserving a margin around functional structures. *Neurosurg Focus* 28, E8. doi:10.3171/2009.12.FOCUS09236.

Giussani, C., Roux, F.-E., Ojemann, J., Sganzerla, E. P., Pirillo, D., and Papagno, C. (2010). Is Preoperative Functional Magnetic Resonance Imaging Reliable for Language Areas Mapping in Brain Tumor Surgery? Review of Language Functional Magnetic Resonance Imaging and Direct Cortical Stimulation Correlation Studies. *Neurosurgery* 66, 113–120. doi:10.1227/01.NEU.0000360392.15450.C9.

Glodzik, L., Randall, C., Rusinek, H., and de Leon, M. J. (2013). Cerebrovascular reactivity to carbon dioxide in Alzheimer's disease. *J. Alzheimers Dis.* 35, 427–440. doi:10.3233/JAD-122011.

Glover, G. H., Li, T. Q., and Ress, D. (2000). Image-based method for retrospective correction of physiological motion effects in fMRI: RETROICOR. *Magn Reson Med* 44, 162–167.

Gonzalez-Castillo, J., Roopchansingh, V., Bandettini, P. A., and Bodurka, J. (2011). Physiological noise effects on the flip angle selection in BOLD fMRI. *Neuroimage* 54, 2764–2778. doi:10.1016/j.neuroimage.2010.11.020.

Greicius, M. D., Kiviniemi, V., Tervonen, O., Vainionpää, V., Alahuhta, S., Reiss, A. L., et al. (2008). Persistent default-mode network connectivity during light sedation. *Hum Brain Mapp* 29, 839–847. doi:10.1002/hbm.20537.

Greicius, M. D., Krasnow, B., Reiss, A. L., and Menon, V. (2003). Functional connectivity in the resting brain: a network analysis of the default mode hypothesis. *Proc. Natl. Acad. Sci. U.S.A.* 100, 253–258. doi:10.1073/pnas.0135058100.

Guldenmund, P., Demertzi, A., Boveroux, P., Boly, M., Vanhaudenhuyse, A., Bruno, M.-A., et al. (2013). Thalamus, brainstem and salience network connectivity changes during propofol-induced sedation and unconsciousness. *Brain Connect* 3, 273–285. doi:10.1089/brain.2012.0117.

Harris, J. J., Reynell, C., and Attwell, D. (2011). The physiology of developmental changes in BOLD functional imaging signals. *Dev Cogn Neurosci* 1, 199–216. doi:10.1016/j.dcn.2011.04.001.

Harrison, R. V., Harel, N., Panesar, J., and Mount, R. J. (2002). Blood capillary distribution correlates with hemodynamic-based functional imaging in cerebral cortex. *Cereb. Cortex* 12, 225–233.

Hart, M. G., Price, S. J., and Suckling, J. (2016). Functional connectivity networks for preoperative brain mapping in neurosurgery. *J. Neurosurg.* 126, 1941–1950. doi:10.3171/2016.6.JNS1662.

Heine, L., Soddu, A., Gómez, F., Vanhaudenhuyse, A., Tshibanda, L., Thonnard, M., et al. (2012). Resting state networks and consciousness: alterations of multiple resting state network connectivity in physiological, pharmacological, and pathological consciousness States. *Front. Psychol.* 3, 295. doi:10.3389/fpsyg.2012.00295.

Horovitz, S. G., Braun, A. R., Carr, W. S., Picchioni, D., Balkin, T. J., Fukunaga, M., et al. (2009). Decoupling of the brain's default mode network during deep sleep. *Proc. Natl. Acad. Sci. U.S.A.* 106, 11376–11381. doi:10.1073/pnas.0901435106.

Hou, B. L., Bradbury, M., Peck, K. K., Petrovich, N. M., Gutin, P. H., and Holodny, A. I. (2006). Effect of brain tumor neovasculature defined by rCBV on BOLD fMRI activation volume in the primary motor cortex. *Neuroimage* 32, 489–497. doi:10.1016/j.neuroimage.2006.04.188.

Hsu, A.-L., Chou, K.-H., Chao, Y.-P., Fan, H.-Y., Wu, C. W., and Chen, J.-H. (2016). Physiological Contribution in Spontaneous Oscillations: An Approximate Quality-Assurance Index for Resting-State fMRI Signals. *PLoS ONE* 11, e0148393. doi:10.1371/journal.pone.0148393.

Hsu, A.-L., Johnson, J. M., Noll, K. R., Prabhu, S. S., Chen, J.-H., and Liu, H.-L. (2018). Combining regional homogeneity and meta-analysis to improve preoperative language mapping with resting-state functional MRI. in (Paris, France).

Hsu, Y.-Y., Chang, C.-N., Jung, S.-M., Lim, K.-E., Huang, J.-C., Fang, S.-Y., et al. (2004). Blood oxygenation level-dependent MRI of cerebral gliomas during breath holding. *J Magn Reson Imaging* 19, 160–167. doi:10.1002/jmri.10447.

Huang, H., Ding, Z., Mao, D., Yuan, J., Zhu, F., Chen, S., et al. (2016). PreSurgMapp: a MATLAB Toolbox for Presurgical Mapping of Eloquent Functional Areas Based on Task-Related and Resting-State Functional MRI. *Neuroinformatics* 14, 421–438. doi:10.1007/s12021-016-9304-y.

Huang, N. E., Shen, Z., and Long, S. R. (1998). The empirical mode decomposition and the Hilbert spectrum for nonlinear and non-stationary time series analysis. *Proc. R. Soc. Lond. A* 454, 903–995.

Huber, L., Goense, J., Kennerley, A. J., Ivanov, D., Krieger, S. N., Lepsien, J., et al. (2014). Investigation of the neurovascular coupling in positive and negative BOLD responses in human brain at 7 T. *Neuroimage* 97, 349–362. doi:10.1016/j.neuroimage.2014.04.022.

Huettel, S. A., Song, A. W., and McCarthy, G. (2009). Functional Magnetic Resonance Imaging. 542.

Hui, M., Li, J., Wen, X., Yao, L., and Long, Z. (2011). An empirical comparison of information-theoretic criteria in estimating the number of independent components of fMRI data. *PLoS ONE* 6, e29274. doi:10.1371/journal.pone.0029274.

Iadecola, C. (2004). Neurovascular regulation in the normal brain and in Alzheimer's disease. *Nat. Rev. Neurosci.* 5, 347–360. doi:10.1038/nrn1387.

IClinfMRI Software for Integrating Functional MRI Techniques in Presurgical Mapping and Clinical Studies IClinfMRI Software for Integrating Functional MRI Techniques in Presurgical Mapping and Clinical Studies.

Jahanian, H., Christen, T., Moseley, M. E., Pajewski, N. M., Wright, C. B., Tamura, M. K., et al. (2016). Measuring vascular reactivity with resting-state blood oxygenation level-dependent (BOLD) signal fluctuations: A potential alternative to the breath-holding challenge? *J. Cereb. Blood Flow Metab.* 37, 2526–2538. doi:10.1177/0271678X16670921.

Jaillard, A., Martin, C. D., Garambois, K., Lebas, J. F., and Hommel, M. (2005). Vicarious function within the human primary motor cortex? A longitudinal fMRI stroke study. *Brain* 128, 1122–1138. doi:10.1093/brain/awh456.

Janecek, J. K., Swanson, S. J., Sabsevitz, D. S., Hammeke, T. A., Raghavan, M., E Rozman, M., et al. (2013). Language lateralization by fMRI and Wada testing in 229 patients with epilepsy: rates and predictors of discordance. *Epilepsia* 54, 314–322. doi:10.1111/epi.12068.

Jenkinson, M., Beckmann, C. F., Behrens, T. E. J., Woolrich, M. W., and Smith, S. M. (2012). FSL. *Neuroimage* 62, 782–790. doi:10.1016/j.neuroimage.2011.09.015.

Jiang, L., and Zuo, X. N. (2016). Regional Homogeneity: A Multimodal, Multiscale Neuroimaging Marker of the Human Connectome. *The Neuroscientist* 22, 486–505. doi:10.1177/1073858415595004.

Jo, H. J., Saad, Z. S., Simmons, W. K., Milbury, L. A., and Cox, R. W. (2010). Mapping sources of correlation in resting state FMRI, with artifact detection and removal. *Neuroimage* 52, 571–582. doi:10.1016/j.neuroimage.2010.04.246.

Kastrup, A., Krüger, G., Neumann-Haefelin, T., and Moseley, M. E. (2001). Assessment of cerebrovascular reactivity with functional magnetic resonance imaging: comparison of CO(2) and breath holding. *Magn Reson Imaging* 19, 13–20.

Kellman, P., and McVeigh, E. R. (2005). Image reconstruction in SNR units: a general method for SNR measurement. *Magn Reson Med* 54, 1439–1447. doi:10.1002/mrm.20713.

Kochiyama, T., Morita, T., Okada, T., Yonekura, Y., Matsumura, M., and Sadato, N. (2005). Removing the effects of task-related motion using independent-component analysis. *Neuroimage* 25, 802–814. doi:10.1016/j.neuroimage.2004.12.027.

Kokkonen, S.-M., Nikkinen, J., Remes, J., Kantola, J., Starck, T., Haapea, M., et al. (2009). Preoperative localization of the sensorimotor area using independent component analysis of resting-state fMRI. *Magn Reson Imaging* 27, 733–740. doi:10.1016/j.mri.2008.11.002.

Kristo, G., Rutten, G.-J., Raemaekers, M., de Gelder, B., Rombouts, S. A. R. B., and Ramsey, N. F. (2014). Task and task-free FMRI reproducibility comparison for motor network identification. *Hum Brain Mapp* 35, 340–352. doi:10.1002/hbm.22180.

Krüger, G., Kastrup, A., and Glover, G. H. (2001). Neuroimaging at 1.5 T and 3.0 T: comparison of oxygenation-sensitive magnetic resonance imaging. *Magn Reson Med* 45, 595–604.

Kwong, K. K., Belliveau, J. W., Chesler, D. A., Goldberg, I. E., Weisskoff, R. M., Poncelet, B. P., et al. (1992). Dynamic magnetic resonance imaging of human brain activity during primary sensory stimulation. *Proc. Natl. Acad. Sci. U.S.A.* 89, 5675–5679.

Lang, S., Duncan, N., and Northoff, G. (2014). Resting-state functional magnetic resonance imaging: review of neurosurgical applications. *Neurosurgery* 74, 453–64–discussion 464–5. doi:10.1227/NEU.0000000000000307.

Lee, M. H., Miller-Thomas, M. M., Benzinger, T. L., Marcus, D. S., Hacker, C. D., Leuthardt, E. C., et al. (2016). Clinical Resting-state fMRI in the Preoperative Setting: Are We Ready for Prime Time? *Top Magn Reson Imaging* 25, 11–18. doi:10.1097/RMR.0000000000000075.

Lee, M. H., Smyser, C. D., and Shimony, J. S. (2013). Resting-state fMRI: a review of methods and clinical applications. *AJNR Am J Neuroradiol* 34, 1866–1872. doi:10.3174/ajnr.A3263.

Leopold, D. A., Murayama, Y., and Logothetis, N. K. (2003). Very slow activity fluctuations in monkey visual cortex: implications for functional brain imaging. *Cereb. Cortex* 13, 422–433.

Li, Y.-O., Adali, T., and Calhoun, V. D. (2007). Estimating the number of independent components for functional magnetic resonance imaging data. *Hum Brain Mapp* 28, 1251–1266. doi:10.1002/hbm.20359.

Liang, P., Zhang, H., Xu, Y., Jia, W., Zang, Y., and Li, K. (2015). Disruption of cortical integration during midazolam-induced light sedation. *Hum Brain Mapp* 36, 4247–4261. doi:10.1002/hbm.22914.

Lin, S.-H. N., Lin, G.-H., Tsai, P.-J., Hsu, A.-L., Lo, M.-T., Yang, A. C., et al. (2016). Sensitivity enhancement of task-evoked fMRI using ensemble empirical mode decomposition. *J. Neurosci. Methods* 258, 56–66. doi:10.1016/j.jneumeth.2015.10.009.

Lindquist, M. A. (2008). The Statistical Analysis of fMRI Data. *Statist. Sci.* 23, 439–464. doi:10.1214/09-STS282.

Liu, H., Buckner, R. L., Talukdar, T., Tanaka, N., Madsen, J. R., and Stufflebeam, S. M. (2009). Task-free presurgical mapping using functional magnetic resonance imaging intrinsic activity. *J. Neurosurg.* 111, 746–754. doi:10.3171/2008.10.JNS08846.

Liu, H.-L., Huang, J. U.-C., Wu, C.-T., and Hsu, Y.-Y. (2002). Detectability of blood oxygenation level-dependent signal changes during short breath hold duration. *Magn Reson Imaging* 20, 643–648.

Logothetis, N. K. (2007). The ins and outs of fMRI signals. *Nat. Neurosci.* 10, 1230–1232. doi:10.1038/nn1007-1230.

Logothetis, N. K., Pauls, J., Augath, M., Trinath, T., and Oeltermann, A. (2001). Neurophysiological investigation of the basis of the fMRI signal. *Nature* 412, 150–157. doi:10.1038/35084005.

Lu, J., Zhang, H., Hameed, N. U. F., Zhang, J., Yuan, S., Qiu, T., et al. (2017). An automated method for identifying an independent component analysis-based language-related resting-state network in brain tumor subjects for surgical planning. *Sci Rep* 7, 13769. doi:10.1038/s41598-017-14248-5.

Lu, J.-F., Zhang, H., Wu, J.-S., Yao, C.-J., Zhuang, D.-X., Qiu, T.-M., et al. (2012). "Awake" intraoperative functional MRI (ai-fMRI) for mapping the eloquent cortex: Is it possible in awake craniotomy? *Neuroimage Clin* 2, 132–142. doi:10.1016/j.nicl.2012.12.002.

Macdonald, A. W., Carter, C. S., Kerns, J. G., Ursu, S., Barch, D. M., Holmes, A. J., et al. (2005). Specificity of prefrontal dysfunction and context processing deficits to schizophrenia in never-medicated patients with first-episode psychosis. *Am J Psychiatry* 162, 475–484. doi:10.1176/appi.ajp.162.3.475.

Mahowald, K., and Fedorenko, E. (2016). Reliable individual-level neural markers of high-level language processing: A necessary precursor for relating neural variability to behavioral and genetic variability. *Neuroimage* 139, 74–93. doi:10.1016/j.neuroimage.2016.05.073.

Matthews, P. M., and Hampshire, A. (2016). Clinical Concepts Emerging from fMRI Functional Connectomics. *Neuron* 91, 511–528. doi:10.1016/j.neuron.2016.07.031.

Matthews, P. M., Honey, G. D., and Bullmore, E. T. (2006). Applications of fMRI in translational medicine and clinical practice. *Nat. Rev. Neurosci.* 7, 732–744. doi:10.1038/nrn1929.

Mikulis, D. J. (2013). Chronic neurovascular uncoupling syndrome. *Stroke* 44, S55–7. doi:10.1161/STROKEAHA.113.001081.

Mikulis, D. J., Krolczyk, G., Desal, H., Logan, W., Deveber, G., Dirks, P., et al. (2005). Preoperative and postoperative mapping of cerebrovascular reactivity in moyamoya disease by using blood oxygen level-dependent magnetic resonance imaging. *J. Neurosurg.* 103, 347–355. doi:10.3171/jns.2005.103.2.0347.

Minzenberg, M. J., Laird, A. R., Thelen, S., Carter, C. S., and Glahn, D. C. (2009). Meta-analysis of 41 functional neuroimaging studies of executive function in schizophrenia. *Arch. Gen. Psychiatry* 66, 811–822. doi:10.1001/archgenpsychiatry.2009.91.

Mitchell, T. J., Hacker, C. D., Breshears, J. D., Szrama, N. P., Sharma, M., Bundy, D. T., et al. (2013). A novel data-driven approach to preoperative mapping of functional cortex using resting-state functional magnetic resonance imaging. *Neurosurgery* 73, 969–82– discussion 982–3. doi:10.1227/NEU.0000000000000141.

Molloy, E. K., Meyerand, M. E., and Birn, R. M. (2014). The influence of spatial resolution and smoothing on the detectability of resting-state and task fMRI. *Neuroimage* 86, 221–230. doi:10.1016/j.neuroimage.2013.09.001.

Mueller, S., Wang, D., Fox, M. D., Yeo, B. T. T., Sepulcre, J., Sabuncu, M. R., et al. (2013). Individual variability in functional connectivity architecture of the human brain. *Neuron* 77, 586–595. doi:10.1016/j.neuron.2012.12.028.

Mukamel, R., Gelbard, H., Arieli, A., Hasson, U., Fried, I., and Malach, R. (2005). Coupling between neuronal firing, field potentials, and FMRI in human auditory cortex. *Science* 309, 951–954. doi:10.1126/science.1110913.

Murphy, K., Birn, R. M., Handwerker, D. A., Jones, T. B., and Bandettini, P. A. (2009). The impact of global signal regression on resting state correlations: are anti-correlated networks introduced? *Neuroimage* 44, 893–905. doi:10.1016/j.neuroimage.2008.09.036.

Murphy, K., Bodurka, J., and Bandettini, P. A. (2007). How long to scan? The relationship between fMRI temporal signal to noise ratio and necessary scan duration. *Neuroimage* 34, 565–574. doi:10.1016/j.neuroimage.2006.09.032.

Mwansisya, T. E., Hu, A., Li, Y., Chen, X., Wu, G., Huang, X., et al. (2017). Task and resting-state fMRI studies in first-episode schizophrenia: A systematic review. *Schizophr. Res.* 189, 9–18. doi:10.1016/j.schres.2017.02.026.

Nadkarni, T. N., Andreoli, M. J., Nair, V. A., Yin, P., Young, B. M., Kundu, B., et al. (2015). Usage of fMRI for pre-surgical planning in brain tumor and vascular lesion patients: task and statistical threshold effects on language lateralization. *Neuroimage Clin* 7, 415–423. doi:10.1016/j.nicl.2014.12.014.

Ogawa, S., Lee, T. M., Kay, A. R., and Tank, D. W. (1990). Brain magnetic resonance imaging with contrast dependent on blood oxygenation. *Proc. Natl. Acad. Sci. U.S.A.* 87, 9868–9872.

Ojemann, G., Ojemann, J., Lettich, E., and Berger, M. (1989). Cortical language localization in left, dominant hemisphere. An electrical stimulation mapping investigation in 117 patients. *J. Neurosurg.* 71, 316–326. doi:10.3171/jns.1989.71.3.0316.

Pak, R. W., Hadjiabadi, D. H., Senarathna, J., Agarwal, S., Thakor, N. V., Pillai, J. J., et al. (2017). Implications of neurovascular uncoupling in functional magnetic resonance imaging (fMRI) of brain tumors. *J. Cereb. Blood Flow Metab.* 37, 3475–3487. doi:10.1177/0271678X17707398.

Pan, W.-J., Thompson, G., Magnuson, M., Majeed, W., Jaeger, D., and Keilholz, S. (2011). Broadband local field potentials correlate with spontaneous fluctuations in functional magnetic resonance imaging signals in the rat somatosensory cortex under isoflurane anesthesia. *Brain Connect* 1, 119–131. doi:10.1089/brain.2011.0014.

Perlbarg, V., Bellec, P., Anton, J.-L., Pélégrini-Issac, M., Doyon, J., and Benali, H. (2007). CORSICA: correction of structured noise in fMRI by automatic identification of ICA components. *Magn Reson Imaging* 25, 35–46. doi:10.1016/j.mri.2006.09.042.

Pillai, J. J. (2010). The evolution of clinical functional imaging during the past 2 decades and its current impact on neurosurgical planning. *AJNR Am J Neuroradiol* 31, 219–225. doi:10.3174/ajnr.A1845.

Pillai, J. J., and Mikulis, D. J. (2015). Cerebrovascular reactivity mapping: an evolving standard for clinical functional imaging. *AJNR Am J Neuroradiol* 36, 7–13. doi:10.3174/ajnr.A3941.

Pillai, J. J., and Zacà, D. (2011). Clinical utility of cerebrovascular reactivity mapping in patients with low grade gliomas. *World J Clin Oncol* 2, 397–403. doi:10.5306/wjco.v2.i12.397.

Pillai, J. J., and Zacà, D. (2012). Comparison of BOLD cerebrovascular reactivity mapping and DSC MR perfusion imaging for prediction of neurovascular uncoupling potential in brain tumors. *Technol. Cancer Res. Treat.* 11, 361–374. doi:10.7785/tcrt.2012.500284.

Power, J. D., Barnes, K. A., Snyder, A. Z., Schlaggar, B. L., and Petersen, S. E. (2012). Spurious but systematic correlations in functional connectivity MRI networks arise from subject motion. *Neuroimage* 59, 2142–2154. doi:10.1016/j.neuroimage.2011.10.018.

Power, J. D., Mitra, A., Laumann, T. O., Snyder, A. Z., Schlaggar, B. L., and Petersen, S. E. (2014). Methods to detect, characterize, and remove motion artifact in resting state fMRI. *Neuroimage* 84, 320–341. doi:10.1016/j.neuroimage.2013.08.048.

Power, J. D., Schlaggar, B. L., and Petersen, S. E. (2015). Recent progress and outstanding issues in motion correction in resting state fMRI. *Neuroimage* 105, 536–551. doi:10.1016/j.neuroimage.2014.10.044.

Pujol, J., Conesa, G., Deus, J., López-Obarrio, L., Isamat, F., and Capdevila, A. (1998). Clinical application of functional magnetic resonance imaging in presurgical identification of the central sulcus. *J. Neurosurg.* 88, 863–869. doi:10.3171/jns.1998.88.5.0863.

Quigley, M., Cordes, D., Wendt, G., Turski, P., Moritz, C., Haughton, V., et al. (2001). Effect of focal and nonfocal cerebral lesions on functional connectivity studied with MR imaging. *AJNR Am J Neuroradiol* 22, 294–300.

Rasetti, R., Mattay, V. S., Stankevich, B., Skjei, K., Blasi, G., Sambataro, F., et al. (2010). Modulatory effects of modafinil on neural circuits regulating emotion and cognition. *Neuropsychopharmacology* 35, 2101–2109. doi:10.1038/npp.2010.83.

Rasmussen, I. A., Jr, Lindseth, F., Rygh, O. M., Berntsen, E. M., Selbekk, T., Xu, J., et al. (2007). Functional neuronavigation combined with intra-operative 3D ultrasound: Initial experiences during surgical resections close to eloquent brain areas and future directions in automatic brain shift compensation of preoperative data. *Acta Neurochir* 149, 365–378. doi:10.1080/01616412.2000.11740684.

Reeder, S. B., Wintersperger, B. J., Dietrich, O., Lanz, T., Greiser, A., Reiser, M. F., et al. (2005). Practical approaches to the evaluation of signal-to-noise ratio performance with parallel imaging: application with cardiac imaging and a 32-channel cardiac coil. *Magn Reson Med* 54, 748–754. doi:10.1002/mrm.20636.

Reinges, M. H. T., Nguyen, H.-H., Krings, T., Hütter, B.-O., Rohde, V., and Gilsbach, J. M. (2004). Course of brain shift during microsurgical resection of supratentorial cerebral lesions: limits of conventional neuronavigation. *Acta Neurochir* 146, 369–77–discussion 377. doi:10.1007/s00701-003-0204-1.

Rombouts, S. A., Barkhof, F., Hoogenraad, F. G., Sprenger, M., Valk, J., and Scheltens, P. (1997). Test-retest analysis with functional MR of the activated area in the human visual cortex. *AJNR Am J Neuroradiol* 18, 1317–1322.

Rosazza, C., Aquino, D., D'Incerti, L., Cordella, R., Andronache, A., Zacà, D., et al. (2014). Preoperative mapping of the sensorimotor cortex: comparative assessment of task-based and resting-state FMRI. *PLoS ONE* 9, e98860. doi:10.1371/journal.pone.0098860.

Roy, C. S., and Sherrington, C. S. (1890). On the Regulation of the Blood-supply of the Brain. *J. Physiol. (Lond.)* 11, 85–158.17.

Saad, Z. S., Glen, D. R., Chen, G., Beauchamp, M. S., Desai, R., and Cox, R. W. (2009). A new method for improving functional-to-structural MRI alignment using local Pearson correlation. *Neuroimage* 44, 839–848. doi:10.1016/j.neuroimage.2008.09.037.

Sabsevitz, D. S., Swanson, S. J., Hammeke, T. A., Spanaki, M. V., Possing, E. T., Morris, G. L., et al. (2003). Use of preoperative functional neuroimaging to predict language deficits from epilepsy surgery. *Neurology* 60, 1788–1792.

Sair, H. I., Yahyavi-Firouz-Abadi, N., Calhoun, V. D., Airan, R. D., Agarwal, S., Intrapiromkul, J., et al. (2016). Presurgical brain mapping of the language network in patients with brain tumors using resting-state fMRI: Comparison with task fMRI. *Hum Brain Mapp* 37, 913–923. doi:10.1002/hbm.23075.

Sanai, N., Mirzadeh, Z., and Berger, M. S. (2008). Functional Outcome after Language Mapping for Glioma Resection. *N Engl J Med* 358, 18–27. doi:10.1056/NEJMoa067819.

Scheinost, D., Papademetris, X., and Constable, R. T. (2014). The impact of image smoothness on intrinsic functional connectivity and head motion confounds. *Neuroimage* 95, 13–21. doi:10.1016/j.neuroimage.2014.03.035.

Scoriels, L., Jones, P. B., and Sahakian, B. J. (2013). Modafinil effects on cognition and emotion in schizophrenia and its neurochemical modulation in the brain. *Neuropharmacology* 64, 168–184. doi:10.1016/j.neuropharm.2012.07.011.

Shattuck, D. W., Mirza, M., Adisetiyo, V., Hojatkashani, C., Salamon, G., Narr, K. L., et al. (2008). Construction of a 3D probabilistic atlas of human cortical structures. *Neuroimage* 39, 1064–1080. doi:10.1016/j.neuroimage.2007.09.031.

Shimony, J. S., Zhang, D., Johnston, J. M., Fox, M. D., Roy, A., and Leuthardt, E. C. (2009). Resting-state spontaneous fluctuations in brain activity: a new paradigm for presurgical planning using fMRI. *Acad Radiol* 16, 578–583. doi:10.1016/j.acra.2009.02.001.

Shmuel, A., Yacoub, E., Chaimow, D., Logothetis, N. K., and Uğurbil, K. (2007). Spatio-temporal point-spread function of fMRI signal in human gray matter at 7 Tesla. *Neuroimage* 35, 539–552. doi:10.1016/j.neuroimage.2006.12.030.

Silva, M. A., See, A. P., Essayed, W. I., Golby, A. J., and Tie, Y. (2018). Challenges and techniques for presurgical brain mapping with functional MRI. *Neuroimage Clin* 17, 794–803. doi:10.1016/j.nicl.2017.12.008.

Smith, S. M., Beckmann, C. F., Andersson, J., Auerbach, E. J., Bijsterbosch, J., Douaud, G., et al. (2013). Resting-state fMRI in the Human Connectome Project. *Neuroimage* 80, 144–168. doi:10.1016/j.neuroimage.2013.05.039.

Smith, S. M., Fox, P. T., Miller, K. L., Glahn, D. C., Fox, P. M., Mackay, C. E., et al. (2009). Correspondence of the brain's functional architecture during activation and rest. *Proc. Natl. Acad. Sci. U.S.A.* 106, 13040–13045. doi:10.1073/pnas.0905267106.

Smith, S. M., Jenkinson, M., Woolrich, M. W., Beckmann, C. F., Behrens, T. E. J., Johansen-Berg, H., et al. (2004). Advances in functional and structural MR image analysis and implementation as FSL. *Neuroimage* 23 Suppl 1, S208–19. doi:10.1016/j.neuroimage.2004.07.051.

Sohn, W. S., Yoo, K., Lee, Y.-B., Seo, S. W., Na, D. L., and Jeong, Y. (2015). Influence of ROI selection on resting state functional connectivity: an individualized approach for resting state fMRI analysis. *Front. Neurosci.* 9, 280. doi:10.3389/fnins.2015.00280.

Taylor, P. A., and Saad, Z. S. (2013). FATCAT: (an efficient) Functional and Tractographic Connectivity Analysis Toolbox. *Brain Connect* 3, 523–535. doi:10.1089/brain.2013.0154.

Thomas, C. G., Harshman, R. A., and Menon, R. S. (2002). Noise reduction in BOLD-based fMRI using component analysis. *Neuroimage* 17, 1521–1537.

Tie, Y., Rigolo, L., Norton, I. H., Huang, R. Y., Wu, W., Orringer, D., et al. (2014). Defining language networks from resting-state fMRI for surgical planning--a feasibility study. *Hum Brain Mapp* 35, 1018–1030. doi:10.1002/hbm.22231.

Tomasi, D., and Volkow, N. D. (2012). Resting functional connectivity of language networks: characterization and reproducibility. *Mol. Psychiatry* 17, 841–854. doi:10.1038/mp.2011.177.

Tomasi, D., Wang, G.-J., and Volkow, N. D. (2013). Energetic cost of brain functional connectivity. *Proceedings of the National Academy of Sciences* 110, 13642–13647. doi:10.1073/pnas.1303346110.

Triantafyllou, C., Hoge, R. D., and Wald, L. L. (2006). Effect of spatial smoothing on physiological noise in high-resolution fMRI. *Neuroimage* 32, 551–557. doi:10.1016/j.neuroimage.2006.04.182.

Triantafyllou, C., Hoge, R. D., Krueger, G., Wiggins, C. J., Potthast, A., Wiggins, G. C., et al. (2005). Comparison of physiological noise at 1.5 T, 3 T and 7 T and optimization of fMRI acquisition parameters. *Neuroimage* 26, 243–250. doi:10.1016/j.neuroimage.2005.01.007.

Triantafyllou, C., Polimeni, J. R., and Wald, L. L. (2011). Physiological noise and signal-to-noise ratio in fMRI with multi-channel array coils. *Neuroimage* 55, 597–606. doi:10.1016/j.neuroimage.2010.11.084.

Uğurbil, K., Xu, J., Auerbach, E. J., Moeller, S., Vu, A. T., Duarte-Carvajalino, J. M., et al. (2013). Pushing spatial and temporal resolution for functional and diffusion MRI in the Human Connectome Project. *Neuroimage* 80, 80–104. doi:10.1016/j.neuroimage.2013.05.012.

Ulmer, J. L., Hacein-Bey, L., Mathews, V. P., Mueller, W. M., DeYoe, E. A., Prost, R. W., et al. (2004). Lesion-induced pseudo-dominance at functional magnetic resonance imaging: implications for preoperative assessments. *Neurosurgery* 55, 569–79–discussion 580–1.

Ulmer, J. L., Krouwer, H. G., Mueller, W. M., Ugurel, M. S., Kocak, M., and Mark, L. P. (2003). Pseudo-reorganization of language cortical function at fMR imaging: a consequence of tumor-induced neurovascular uncoupling. *AJNR Am J Neuroradiol* 24, 213–217.

Vlieger, E.-J., Majoie, C. B., Leenstra, S., and Heeten, Den, G. J. (2004). Functional magnetic resonance imaging for neurosurgical planning in neurooncology. *Eur Radiol* 14, 1143–1153. doi:10.1007/s00330-004-2328-y.

Voyvodic, J. T. (2006). Activation mapping as a percentage of local excitation: fMRI stability within scans, between scans and across field strengths. *Magn Reson Imaging* 24, 1249–1261. doi:10.1016/j.mri.2006.04.020.

Weisskoff, R. M. (1996). Simple measurement of scanner stability for functional NMR imaging of activation in the brain. *Magn Reson Med* 36, 643–645.

Weng, H.-H., Noll, K. R., Johnson, J. M., Prabhu, S. S., Tsai, Y.-H., Chang, S.-W., et al. (2017). Accuracy of Presurgical Functional MR Imaging for Language Mapping of Brain Tumors: A Systematic Review and Meta-Analysis. *Radiology* 286, 512–523. doi:10.1148/radiol.2017162971.

Wilson, G. H., Yang, P.-F., Gore, J. C., and Chen, L. M. (2016). Correlated inter-regional variations in low frequency local field potentials and resting state BOLD signals within S1 cortex of monkeys. *Hum Brain Mapp* 37, 2755–2766. doi:10.1002/hbm.23207.

Wink, A. M., and Roerdink, J. B. T. M. (2006). BOLD Noise Assumptions in fMRI. *Int J Biomed Imaging* 2006, 12014. doi:10.1155/IJBI/2006/12014.

Wong, C. W., Olafsson, V., Tal, O., and Liu, T. T. (2013). The amplitude of the resting-state fMRI global signal is related to EEG vigilance measures. *Neuroimage* 83, 983–990. doi:10.1016/j.neuroimage.2013.07.057.

Wu, C. W., Chen, C.-L., Liu, P.-Y., Chao, Y.-P., Biswal, B. B., and Lin, C.-P. (2011). Empirical evaluations of slice-timing, smoothing, and normalization effects in seed-based, resting-state functional magnetic resonance imaging analyses. *Brain Connect* 1, 401–410. doi:10.1089/brain.2011.0018.

Wu, R., Yang, P.-F., and Chen, L. M. (2017). Correlated Disruption of Resting-State fMRI, LFP, and Spike Connectivity between Area 3b and S2 following Spinal Cord Injury in Monkeys. *J. Neurosci.* 37, 11192–11203. doi:10.1523/JNEUROSCI.2318-17.2017.

Yan, F.-X., Wu, C. W., Cheng, S.-Y., Lim, K.-E., Hsu, Y.-Y., and Liu, H.-L. (2013). Resting-state functional magnetic resonance imaging analysis with seed definition constrained by regional homogeneity. *Brain Connect* 3, 438–449. doi:10.1089/brain.2013.0164.

Yarkoni, T., Poldrack, R. A., Nichols, T. E., Van Essen, D. C., and Wager, T. D. (2011). Large-scale automated synthesis of human functional neuroimaging data. *Nat. Methods* 8, 665–670. doi:10.1038/nmeth.1635.

Zacà, D., Jovicich, J., Nadar, S. R., Voyvodic, J. T., and Pillai, J. J. (2014). Cerebrovascular reactivity mapping in patients with low grade gliomas undergoing presurgical sensorimotor mapping with BOLD fMRI. *J Magn Reson Imaging* 40, 383–390. doi:10.1002/jmri.24406.

Zang, Y., Jiang, T., Lu, Y., He, Y., and Tian, L. (2004). Regional homogeneity approach to fMRI data analysis. *Neuroimage* 22, 394–400. doi:10.1016/j.neuroimage.2003.12.030.

Zhang, D., and Raichle, M. E. (2010). Disease and the brain's dark energy. *Nat Rev Neurol* 6, 15–28. doi:10.1038/nrneurol.2009.198.

Zhang, D., Johnston, J. M., Fox, M. D., Leuthardt, E. C., Grubb, R. L., Chicoine, M. R., et al. (2009). Preoperative sensorimotor mapping in brain tumor patients using spontaneous fluctuations in neuronal activity imaged with functional magnetic resonance imaging: initial experience. *Neurosurgery* 65, 226–236. doi:10.1227/01.NEU.0000350868.95634.CA.

Zhao, L., Alsop, D. C., Detre, J. A., and Dai, W. (2017). Global fluctuations of cerebral blood flow indicate a global brain network independent of systemic factors. *J. Cereb. Blood Flow Metab.*, 271678X17726625. doi:10.1177/0271678X17726625.

Zhu, L., Fan, Y., Zou, Q., Wang, J., Gao, J.-H., and Niu, Z. (2014). Temporal reliability and lateralization of the resting-state language network. *PLoS ONE* 9, e85880. doi:10.1371/journal.pone.0085880.

Zuo, X.-N., Xu, T., Jiang, L., Yang, Z., Cao, X.-Y., He, Y., et al. (2013). Toward reliable characterization of functional homogeneity in the human brain: Preprocessing, scan duration, imaging resolution and computational space. *Neuroimage* 65, 374–386. doi:10.1016/j.neuroimage.2012.10.017.